DEVELOPMENT AND APPLICATIONS OF A HETERO-BASED STATISTICAL ASSOCIATING FLUID THEORY

by

Yun Peng

Dissertation

Submitted to the Faculty of the

Graduate School of Vanderbilt University

in partial fulfillment of the requirements

for the degree of

DOCTOR OF PHILOSOPHY

in

Chemical Engineering

December, 2007

Nashville, Tennessee

Approved:

Professor Clare McCabe

Professor Peter T. Cummings

Professor G. Kane Jennings

Professor Scott A. Guelcher

Professor Eva M. Harth

Dedicated

To

My Family

ACKNOWLEDGEMENT

The five years I have spent on my PhD work is the most important part of my life, when my view of life has been developed and my future career path paved. Recalling these past years, though going through difficulties and facing challenges, I have learnt a lot, gained experiences, and enjoyed the happiness of success. This thesis is a result of my research in the field of thermodynamic modeling and molecular simulation conducted at the Colorado School of Mines and at Vanderbilt University, where I have been accompanied and supported by so many great people. I wish to express my sincere gratitude to them.

The first person I would like to thank is my advisor, Dr. Clare McCabe. I feel honored to be one of her first PhD students. I have been receiving her constructive guidance and her important support and encouragement throughout my work. She is my first mentor leading me into the door of advanced chemical engineering in thermodyamics.

I would also thank people with whom I collaborated in my research projects and all members in Dr. McCabe's group. Particularly, I would like to thank Dr. Honggang Zhao for his endless patience and help and for being an excellent example to me. I also thank Dr. Oleg A. Mazyar and Kevin Hadley for their useful discussions on my project.

I would also like to thank other members of my committee, Dr. Peter T. Cummings, Dr. G. Kane Jennings, Dr. Scott A. Guelcher, Dr. Eva M. Harth, and Departments of Chemical Engineering at the Colorado School of Mines and Vanderbilt University for their valuable support.

Finally and mostly, I would like to express my deepest gratitude to my parents who raised me, give me their endless love and support, and always encourage me to make progress and pursue my goals. All of these have got me to where I am today. I am so proud to be their daughter.

TABLE OF CONTENTS

Page

LIST OF TABLES

Page

LIST OF FIGURES

Page

CHAPTER I

INTRODUCTION AND BACKGROUND

1.1 Introduction

Although the study of fluid phase behavior and the development of accurate theoretical approaches to predict physical properties and phase diagrams is a very traditional area of chemical engineering research, it is still a very important and active one. Reliable methods for the theoretical prediction of thermophysical properties (such as volumetric, thermal and transport properties) and phase equilibria are essential to the chemical industry. This is because physical property data is needed in all aspects of plant operation, and in particular for the design of separation processes. The need for efficient separations is self-evident: separation processes account for 43% of the energy consumed and up to 70% of capital investment in chemical plants [1]. Therefore central to continued improvements in process and product design, product safety and the development of new application areas such as biotechnology, is the need to develop accurate tools for physical property prediction.

An equation of state (EOS) is a very useful and efficient tool with which to investigate the thermodynamic properties of fluids. While numerous equations of state have been reported in the literature, traditional equations of state, such as cubic EOS, are typically only suitable for describing simple, nearly spherical molecules such as small alkanes, nitrogen, etc. When applied to the study of the phase behavior of complex fluids such as polymers, and associating fluids like water and alcohols, they generally fail to

accurately reproduce the phase behavior without extensive fitting to experimental data. Parameters for each system studied are determined by fitting to experimental data leading to effective parameters for the molecular size and interactions, which have little or no predictive value outside of the region of the phase diagram to which they are fitted. This also often leads to the use of unphysical mixing rules and/or temperature-dependent and/or concentration-dependent binary parameters.

Molecular-based equations of state such as the statistical associating fluid theory (SAFT) [2] and the perturbed hard-chain theory (PHCT) [3] have parameters that relate to physical interactions and therefore are generally more successful in predicting the phase behavior of fluids, rather than merely correlating experimental data. The SAFT EOS explicitly takes into account the non-sphericity and association interactions and hence can not only be applied to treat the simple spherical molecules, but also chain fluids and associating and non-associating fluids. There have been many extensions and variations of the original SAFT expressions (more details are give in section 1.2). In this work we focus on SAFT-VR, which describes chain molecules formed from hard-core monomers with attractive potentials of variable range (SAFT-VR) [4, 5], typically a square well potential. SAFT-VR has been successfully used to describe the phase equilibria of a wide range of industrially important systems including polymers [6, 7]. However, all of the real fluids modeled to-date with SAFT-VR have been treated as homonuclear chains and hence it is not possible to explicitly capture the effects of molecular structure and composition on thermodynamic properties and phase behavior. Therefore, we have developed a hetero-SAFT-VR model which allows the modeling of molecules composed of segments of different size and/or energy parameters and hence

explicitly describes heteronuclear chains. In order to validate the hetero-SAFT-VR approach, we have performed molecular simulations for the same model as used in the theoretical approach. The hetero-SAFT-VR equation has been applied to the study of the thermodynamic properties of polyhedral olgiomeric silsesquioxanes and the phase behavior of small molecules using a group-contribution-based hetero-SAFT-VR equation. With the GC-SAFT-VR method we are able to determine the model parameters needed to describe molecules of low molecular weight through to polymers, and accurately capture the effects of molecule composition and structure.

In the remainder of Chapter I, we give a brief description of the SAFT EOSs and in particular heteronuclear versions of SAFT. We will also provide some background on the molecular simulation techniques used in this work to validate the theory. In Chapter II, we provide a detailed description of the hetero-SAFT-VR equation and also a description of the GC-SAFT-VR equation, which is based on the hetero-SAFT-VR equation. In Chapter III, our work on validation of the hetero-SAFT-VR EOS through comparison with *isothermal-isobaric (NPT)* Monte Carlo (MC) and Gibbs ensemble Monte Carlo (GEMC) simulations are presented [8]. In Chapter IV, the hetero-SAFT-VR approach is applied to study the effect of tether groups on the thermodynamic properties and phase behavior of polyhedral oligomeric silsesquioxane (POSS) fluids [9]. In Chapter V, the development of a GC-SAFT-VR model to study the phase behavior of pure fluids and binary mixture systems is presented [10]. In Chapter VI, the GC-SAFT-VR is extended to study the phase properties (VLE and LLE) for polymer solutions using the parameters obtained in Chapter V [11]. Finally, conclusions and future work are discussed in Chapter VII.

1.2 Background

1.2.1 SAFT Equation of State

An important feature of the SAFT equation of state is that it explicitly takes into account the non-sphericity and association interactions of real molecules. In the SAFT formalism, following the seminal work of Wertheim [12-15], the free energy is written as the sum of four separate contributions:

$$\frac{A}{NkT} = \frac{A^{ideal}}{NkT} + \frac{A^{mono}}{NkT} + \frac{A^{chain}}{NkT} + \frac{A^{assoc}}{NkT} \tag{1.1}$$

where N is the number of molecules, k Boltzmann's constant, and T the temperature. A^{ideal} is the ideal free energy, A^{mono} the contribution to the free energy due to the monomer segments, A^{chain} the contribution due to the formation of bonds between monomer segments, and A^{assoc} is the contribution due to association. Hence, a SAFT fluid is a collection of monomers that can form covalent bonds; the monomers interact via repulsive and attractive (dispersion) forces, and, in some cases, association interactions. Since the SAFT EOS has a firm basis in statistical mechanical perturbation theory for well-defined molecular models, systematic improvement (e.g., by improved expressions for the monomer free energy and structure) and extension of the theory (e.g., by considering new monomer fluids, bonding schemes and association interactions) is possible by comparing the theoretical predictions with computer simulation results on the same molecular model. This also results in many versions and applications of SAFT-based approaches in the literature since the introduction of the original SAFT expressions in the late 80's. By far the most widely used version of the SAFT EOS is the engineering version of SAFT developed by Huang and Radosz (HR-SAFT) [16, 17]. HR-SAFT is

based on an argon equation of state (the so-called Back equation of state) for the dispersion term and a hard-sphere pair-correlation function for the chain term. Pure-component parameters have been determined for over 100 real fluids, e.g., simple inorganics, alkanes, cyclic molecules, aromatics, ethers, ketones, esters, alkenes, chlorinated hydrocarbons, water, ammonia, hydrogen sulfide, alkanols, acids, and primary and secondary amines, and polymeric substances [18]. Perhaps the simplest version of SAFT is SAFT-HS [19], in which chains are modeled as hard-sphere (HS) segments with dispersion interactions approximated at the mean-field level of van der Waals. SAFT-HS has been successfully used to study the phase behavior and critical lines of strongly associating systems, such as the alkanes + water [20], refrigerants + hydrogen fluoride [21], and water + alkylpolyoxyeythylenes [22, 23]. SAFT-HS is seen to work best in systems with strong association, where the weak dispersion forces described by the mean-field approximation are masked by the strong association interactions [4]. However, it is not adequate to study systems where the dispersive interactions are dominant. Several other versions of SAFT have been proposed that provide a better description of the reference fluid and monomer free energy (e.g., dispersion interactions). For example, instead of using hard spheres as the reference fluid as used in the original SAFT, HR-SAFT and SAFT-HS equations, Blas and Vega proposed the soft-SAFT approach [24] in which the reference fluid is modeled as a Lennard Jones fluid. Soft-SAFT has been used to study pure fluids such as *n*-alkanes, 1-alkenes, 1-alcohols and binary/ternary mixtures of *n*-alkanes [24, 25] and carbon dioxide and perfluoroalkanes [26]. However, the Lennard Jones reference term used fitted to simulation data for the pure Lennard Jones fluids and so an analytical expression is not

used. Later, Gross and Sadowski developed the perturbed-chain SAFT (PC-SAFT) equation [27] which explicitly accounts for the nonsphericity of chain molecules by using a hard-chain reference fluid, rather than monomer segments as is used in all other of versions of SAFT. Again, this results in a non-analytical expression for the monomer free energy as the model is fitted to the pure-component properties of *n*-alkanes. The chain term and association term in PC-SAFT are the same as those in the original SAFT approach. PC-SAFT has been applied to study many systems such as polar fluids [28], polymer [29], and copolymer systems [30, 31].

In this work we focus on SAFT-VR, which describes chain molecules formed from hard-core monomers with attractive potentials of variable range (SAFT-VR) [4, 5], typically a square well. In this version of the theory the dispersive interactions are treated via a second-order high-temperature perturbation expansion, providing a more rigorous description of the thermodynamics than found in simpler versions of the SAFT approach [32]. SAFT-VR EOS provides better description of the dispersion interactions than the SAFT-HS EOS and also has the advantage over other SAFT equations in that it uses analytical expressions to describe the monomer fluids. In this way the theory can be readily extended by using different approximations for the reference fluid. SAFT-VR has been successfully used to describe the fluid phase equilibria of a wide range of industrially important systems; for example, short alkanes through to simple polymers of high molecular weight [6, 32-36], and their binary mixtures [33, 37-42], perfluoroalkanes [43, 44] and other fluorinated molecules of industrial importance [45-48], water [49], electrolyte solutions [50-52], and carbon dioxide [42, 53-56], have all been studied. It

also has recently been extended to accurately model the critical region [36, 41, 42] and rigorously incorporate dipolar interactions into the model chain [57].

1.2.2 Heteronuclear Versions of the SAFT EOS

In recent years, heteronuclear versions of SAFT which allow the model chain to be composed of segments of different size and/or energy have been proposed by several authors [30, 58-68]. The development of the heteronuclear versions of SAFT is mainly carried out by modifying the chain term in equation (1.1). One of the first applications of hetero-SAFT to chain fluids focused on hard systems and compared the theoretical predictions of PVT behavior with simulation data for block, alternate and random copolymers [61]. The SAFT predictions were shown to be more accurate than the available equations of state for heteronuclear chain fluids [3, 69-71], performing well over a range of densities. Of particular interest is the work of Radosz and co-workers on copolymer SAFT [59], which allows for the description of linear and branched copolymers based on the original SAFT. In this approach molecules composed of two distinct types of segments are considered and the sequence of segments is described through a segment fraction, which is the fraction of segments of one type in the chain, and bonding fraction, which define all pairs of segment-segment bonds. Copolymer SAFT was initially applied to the engineering version of SAFT proposed by Huang and Radosz [16] to model real copolymer systems [59, 72], and later to Lennard-Jones- [73] and square-well-based SAFT models [62, 74]. Heteronuclear Lennard Jones chains have also been studied by Tang [75] and Blas and Vega [60]; in both cases the thermodynamics of heteronuclear dimers were studied. More recently PC-SAFT has

been shown to be successful in modeling polymer systems [29, 65] and has been extended to heterosegmented molecules [30, 65] similarly using the bond and segment fraction approach suggested by Banasak *et al.* [59]. However, this yields a statistical (but not exact) description of molecular structure. In this work, we focus on developing a heteronuclear-based on SAFT-VR approach in order to explicitly describe the heterogeneity of molecular structure and composition and later a group-contribution-based hetero-SAFT-VR, which will be described in details in Chapter II.

1.2.3 Molecular Simulation

One of the advantages of the SAFT EOS over conventional cubic equations is that the approximations made in developing the SAFT equation can be rigorously tested against computer simulation results because the simulations are performed on the same model as used in the theory and provide exact properties for the model fluid. In addition, the simulations provide data at the molecular level-molecular on molecular distributions, orientations, coordination numbers, lifetimes of complexes, etc., that can be difficult or impossible to obtain in the laboratory [76].

Monte Carlo (MC) and molecular dynamics (MD) computer simulations allow the study of atomic or molecular systems and provide information on structural, conformational, and thermodynamic properties of a macroscopic sample. MD also provides information on the dynamics of the system. However, using the real time evolution for sampling the configuration space imposes a limitation on the sampling rate. If one is only interested in simulating the nondynamic properties (e.g., thermodynamic properties), MC can be the more efficient alternative.

1.2.3.1 Monte Carlo Simulation

In order to test the hetero-SAFT-VR EOS, we carried out two *NPT* and GEMC MC simulations on the same model (i.e., molecules are modeled as flexible chains in which beads are tangentially bonded interacting through a square well potential) as used in the theory.

In the *NPT* MC simulations, a fixed number of particles, N, which can be a pure fluid or a mixture, are placed in a simulation box. The microscopic state of the system is specified in terms of positions of the particles and interaction potentials. In order to simulate homogeneous bulk phases, periodic boundary condition (PBC), in which the simulation box is replicated throughout space to form an infinite lattice, are used to mimic the presence of an infinite bulk surrounding the *N*-particle system. The volume of the simulation box is allowed to fluctuate while conditions of temperature and pressure are kept constant. Under these conditions, the MC sampling is carried out to generate an ensemble of states. The random sampling of the configuration space is realized by performing a series of trial moves such as particle displacement and reorientation, and volume change. After every trial move, a new trial configuration will be generated. The usual procedure to accept/reject the trial configuration is as follows. The probability *P* of acceptance of the displacement move or reorientation move satisfies [77]:

$$P = \min\left\{1, \exp\left(-\beta \Delta U\right)\right\} \tag{1.2}$$

where ΔU represents energy difference between the trial configuration. The volume-change move is accepted with the probability [77]:

$$P = \min\left\{1, \exp\left(-\beta \Delta H\right)\right\} \tag{1.3}$$

where $\Delta H = \Delta U + P\Delta V - \frac{1}{\beta} N \ln\left(\left(V + \Delta V\right)/V\right)$ represents the enthalpy change. The macroscopic properties such as system density are calculated by averaging over the configuration states during Monte Carlo sampling of configuration space.

The Gibbs Ensemble Monte Carlo (GEMC) simulation technique [78] is used to study phase coexistence in moderately dense fluids in a single simulation. In GEMC, two simulation boxes that are in thermodynamic equilibrium but not in direct contact are used to simulate the two coexisting phases and so allow the simulation of phase equilibria without an interface. Properties such as the density of each phase and the composition of the coexisting phases in mixture systems can be obtained from the GEMC simulation. . The total system of pure fluids is under constant N, V, and T conditions. In order to sample phase space and achieve equilibrium conditions between the two boxes a combination of trial moves are preformed, i.e., particle displacement, rotation, volume change (i.e., one box changed by ΔV, the other box changed by -ΔV), and particle exchange between the two systems. The acceptance displacement, reorientation, and volume change moves follow the same rules as equations (1.2) and (1.3). Additionally, the acceptance of particle exchange satisfies the following rule [79]:

$$P = \min\left\{1, \exp\left(-\beta\Delta G\right)\right\} \tag{1.4}$$

where $\Delta G = \Delta U_i + \Delta U_j + \frac{1}{\beta}\ln\left(\frac{V_i\left(N_j + 1\right)}{N_i V_j}\right)$ represents the Gibbs energy change, i the box where particle is removed, and j the box where particle is inserted. In the particle exchange move a molecule is selected at random from each box to be deleted and created using the using the Widom particle insertion method [80]. The acceptance probability for

a random trial insertion decreases as the density of the liquid phase increases, and especially for chain molecules [81], as it becomes more difficult to successfully insert a molecule without creating overlaps with other molecules. This can be overcome by using the configurational bias Monte Carlo (CBMC) scheme [81-84]. In this approach, part of a chain molecule is rebuilt segment by segment. The trial direction of placing a new segment is decided based on the distribution of Boltzmann factors as function of angular position of the new segment. By biasing the selection of trial directions to a high value of Boltzmann factor, the success of inserting of chain molecules without overlapping is greatly increased. The bias introduced by the grow procedure can be removed exactly by using an adjusted acceptance rule suggested by Frenkel *et al.* [85]. Through generation of chain configurations by successive insertion of the bonded segments of the chain, the efficiency of insertion of the chain molecule is increased.

1.2.3.2 Molecular Dynamics Simulation

In contrast to MC simulation, the beauty of MD simulation lies in the fact that it is governed by Newton's laws of motion. Hence, the path of the trajectory in the configuration space is continuous. The algorithm for performing a MD simulation is as follows: a) the initial positions and velocities of every atom are specified; b) then, using potentials (i.e., a force field describing the molecular intra- and inter interactions), forces acting on each atom are calculated; c) the motion of every atom (trajectory) is calculated by numerically integrating Newton's equations of motion over the time step (Δt). Steps b) and c) are repeated until the time of evolution of the system reaches the desired length of time and the averages of measured properties are computed after the system reaches equilibrium.

MD simulations can be performed under different types of ensembles such as the microcanonical (*NVE*), canonical (*NVT*), isothermal-isobaric (*NPT*), etc. Constant temperature and pressure can be achieved through the use of a different thermostats and barostats, such as those proposed by Berenderson [86, 87] and Nosé and Hoover [88].

CHAPTER II

THE HETERO-SAFT-VR EQUATION

2.1 Hetero-SAFT-VR EOS for Pure Fluids

In the original SAFT-VR approach, applicable to homonuclear chains, chain molecules are formed from tangentially bonded monomer segments. For a pure fluid, all of the segments have the same σ, λ and ε and interact through an attractive potential of variable range. Specifically, a segment of type *i* interacts with a segment of type *j* through a square well (SW) potential,

$$U_{ij}(r) = \begin{cases} +\infty & \text{if} \quad r < \sigma_{ij} \\ -\varepsilon_{ij} & \text{if} \quad \sigma_{ij} \le r < \lambda_{ij}\sigma_{ij} \\ 0 & \text{if} \quad r \ge \lambda_{ij}\sigma_{ij} \end{cases} \tag{2.1}$$

where σ_{ij} is the diameter of the interaction, λ_{ij} the range and ε_{ij} the well depth of the SW potential. Hence, in the original SAFT-VR, $\sigma_{ij} = \sigma$, $\varepsilon_{ij} = \varepsilon$, and $\lambda_{ij} = \lambda$ for all *i*, *j*. By contrast, in this work we have developed the hetero-SAFT-VR approach to treat chains composed of segments of different size and/or energy. The inter- and intra-molecular cross interactions between segments are obtained from the Lorentz-Berthelot combining rules [89],

$$\sigma_{ij} = \frac{\sigma_{ii} + \sigma_{jj}}{2} \tag{2.2}$$

$$\varepsilon_{ij} = \sqrt{\varepsilon_{ii}\varepsilon_{jj}} \tag{2.3}$$

$$\lambda_{ij} = \frac{\lambda_{ii}\sigma_{ii} + \lambda_{jj}\sigma_{jj}}{\sigma_{ii} + \sigma_{jj}} \tag{2.4}$$

The general form of the Helmholtz free energy A within the SAFT framework is given by equation (1.1). We will present each contribution in turn for the treatment of pure fluids composed of polyatomic heteronuclear molecules. We do not give details of the association term since the chain fluids considered in this work are non-associating.

The ideal contribution to the free energy is expressed as:

$$\frac{A^{ideal}}{NkT} = \ln(\rho\Lambda^3) - 1 \tag{2.5}$$

where N is the total number of molecules, k Boltzmann's constant, ρ the number density of chain molecules and Λ the thermal de Broglie wavelength.

The monomer free energy is given by,

$$\frac{A^{mono}}{NkT} = m\frac{A^M}{N_s kT} = ma^M \tag{2.6}$$

where N_s is the total number of segments, determined from the product of the total number of molecules N and the number of segments per molecule m. a^M is free energy per monomer segment and in the SAFT-VR equation is approximated by a second order high temperature expansion using Barker and Henderson perturbation theory for mixtures [90], *viz*

$$a^M = a^{HS} + \beta a_1 + \beta^2 a_2 \tag{2.7}$$

where $\beta = 1/kT$, a^{HS} is the free energy of the hard sphere reference fluid and a_1 and a_2 are the first and second perturbation terms respectively.

The hard sphere reference term a^{HS} is determined from the expression of Boublik [91] and Mansoori and co-workers [92] for multicomponent hard sphere systems, viz

$$a^{HS} = \frac{6}{\pi\rho_s}\left[\left(\frac{\zeta_2^3}{\zeta_3^2} - \zeta_0\right)\ln(1-\zeta_3) + \frac{3\zeta_1\zeta_2}{1-\zeta_3} + \frac{\zeta_2^3}{\zeta_3(1-\zeta_3)^2}\right] \tag{2.8}$$

where ρ_s is the number density of segments, which is defined as N_s/V, the total number of segments divided by the total volume, and ζ_l is the reduced density given by a sum over all segment types i,

$$\zeta_l = \frac{\pi}{6}\rho_s\left[\sum_{i=1}^{n} x_{s,i}(\sigma_i)^l\right] \tag{2.9}$$

where σ_i is diameter of segments of type i and $x_{s,i}$ is the mole fraction of segments of type i. Note that ζ_3 is the volume fraction occupied by the molecules and is generally denoted η.

The first perturbation term a_1 describing the mean-attractive energy is obtained from the sum of all pair interactions,

$$a_1 = \sum_{i=1}^{n}\sum_{j=1}^{n} x_{s,i}x_{s,j}\left(a_1\right)_{ij} \tag{2.10}$$

where $\left(a_1\right)_{ij}$ is obtained from the mean-value theorem as proposed by Gil-Villegas *et al.* [4],

$$\begin{aligned}\left(a_1\right)_{ij} &= -2\pi\rho_s\varepsilon_{ij}\int_{\sigma_{ij}}^{\infty} r_{ij}^2 g_{ij}^{HS}(r_{ij})dr_{ij} \\ &= -\rho_s\alpha_{ij}^{VDW} g_{ij}^{HS}(\sigma_{ij};\zeta_3^{eff})\end{aligned} \tag{2.11}$$

where

$$\alpha_{ij}^{VDW} = \frac{2\pi}{3}\sigma_{ij}^3\varepsilon_{ij}\left(\lambda_{ij}^3 - 1\right) \tag{2.12}$$

Within the van der Waals one-fluid theory the radial distribution function $g_{ij}^{HS}(\sigma_{ij};\zeta_3^{eff})$ is approximated by that for a hypothetical pure fluid, hence equation (2.11) becomes:

$$\left(a_1\right)_{ij} = -\rho_s\alpha_{ij}^{VDW} g_0^{HS}\left[\sigma_x;\zeta_x^{eff}\left(\lambda_{ij}\right)\right] \tag{2.13}$$

where $g_0^{HS}(\sigma_x;\zeta_x^{eff})$ is obtained from the Carnahan and Starling equation of state [93],

$$g_0^{HS}\left[\sigma_x;\zeta_x^{eff}\left(\lambda_{ij}\right)\right] = \frac{1-\zeta_x^{eff}/2}{\left(1-\zeta_x^{eff}\right)^3} \tag{2.14}$$

The effective packing fraction $\zeta_x^{eff}\left(\lambda_{ij}\right)$ of the hypothetical pure fluid is obtained within the van der Waals one fluid theory from the corresponding packing fraction of the mixture ζ_x given by,

$$\zeta_x^{eff}\left(\zeta_x,\lambda_{ij}\right) = c_1\left(\lambda_{ij}\right)\zeta_x + c_2\left(\lambda_{ij}\right)\zeta_x^2 + c_3\left(\lambda_{ij}\right)\zeta_x^3 \tag{2.15}$$

where

$$\begin{pmatrix} c_1 \\ c_2 \\ c_3 \end{pmatrix} = \begin{pmatrix} 2.25855 & -1.50349 & 0.249434 \\ -0.669270 & 1.40049 & -0.827739 \\ 10.1576 & -15.0427 & 5.30827 \end{pmatrix}\begin{pmatrix} 1 \\ \lambda_{ij} \\ \lambda_{ij}^{\,2} \end{pmatrix} \tag{2.16}$$

and

$$\zeta_x = \frac{\pi}{6}\rho_s\sigma_x^3 \tag{2.17}$$

with

$$\sigma_x^3 = \sum_{i=1}^{n}\sum_{j=1}^{n} x_{s,i}x_{s,j}\sigma_{ij}^3 \tag{2.18}$$

This corresponds to mixing rule MX1b in the original SAFT-VR approach for mixtures [5]. We have compared the results obtained from this formulation with the MX3b mixing rule [5], in which the actual packing fraction of the system is used to obtain ζ_3^{eff}, and found that the difference between the two was negligible in most cases. Therefore despite the more rigorous nature of the MX3b approach, we chose MX1b in order to avoid convergence problems in the critical region of the phase diagram [5, 33].

The second order perturbation term for the monomer excess free energy a_2 is expressed as:

$$\begin{aligned} a_2 &= \sum_{i=1}^{n}\sum_{j=1}^{n} x_{s,i}x_{s,j}\left(a_2\right)_{ij} \\ &= x_{s,1}^2\left(a_2\right)_{11} + 2x_{s,1}x_{s,2}\left(a_2\right)_{12} + x_{s,2}^2\left(a_2\right)_{22} \end{aligned} \tag{2.19}$$

where $\left(a_2\right)_{ij}$ is obtained through the local compressibility approximation:

$$\left(a_2\right)_{ij} = \frac{1}{2}K^{HS}\varepsilon_{ij}\rho_s\frac{\partial\left(a_1\right)_{ij}}{\partial\rho_s} \tag{2.20}$$

and K^{HS} is the Percus-Yevick expression for the hard-sphere isothermal compressibility,

$$K^{HS} = \frac{\zeta_0(1-\zeta_3)^4}{\zeta_0(1-\zeta_3)^2 + 6\zeta_1\zeta_2(1-\zeta_3) + 9\zeta_2^3} \tag{2.21}$$

Finally the contribution due to chain formation from the monomer segments is given in terms of the background correlation function y_{ij}^{SW},

$$\frac{A^{chain}}{NkT} = -\sum_{ij\ \text{bonds}} \ln y_{ij}^{SW}\left(\sigma_{ij}\right) \tag{2.22}$$

where the sum is over all bonds in the chain molecule,

$$y_{ij}^{SW}\left(\sigma_{ij}\right)=\exp\left(-\beta\varepsilon_{ij}\right)g_{ij}^{SW}\left(\sigma_{ij}\right) \tag{2.23}$$

The radial distribution function for the square well monomers $g_{ij}^{SW}\left(\sigma_{ij}\right)$ in equation (2.23) is approximated by a first-order high-temperature perturbation expansion:

$$g_{ij}^{SW}\left(\sigma_{ij};\zeta_3\right)=g_{ij}^{HS}\left(\sigma_{ij};\zeta_3\right)+\beta\varepsilon_{ij}g_1^{SW}\left(\sigma_{ij}\right) \tag{2.24}$$

where the contact value of the radial distribution function $g_{ij}^{HS}\left(\sigma_{ij};\zeta_3\right)$ at the actual packing fraction ζ_3 is obtained from the expression of Boublik [91],

$$g_{ij}^{HS}(\sigma_{ij};\zeta_3)=\frac{1}{1-\zeta_3}+3\frac{D_{ij}\zeta_3}{\left(1-\zeta_3\right)^2}+2\frac{\left(D_{ij}\zeta_3\right)^2}{\left(1-\zeta_3\right)^3} \tag{2.25}$$

where

$$\begin{aligned} D_{ij}&=\frac{\sigma_{ii}\sigma_{jj}\sum_{i=1}^{n}x_{s,i}\sigma_{ii}^2}{\left(\sigma_{ii}+\sigma_{jj}\right)\sum_{i=1}^{n}x_{s,i}\sigma_{ii}^3} \\ &=\frac{\sigma_{ii}\sigma_{jj}\left(x_{s,1}\sigma_{11}^2+x_{s,2}\sigma_{22}^2\right)}{\left(\sigma_{ii}+\sigma_{jj}\right)\left(x_{s,1}\sigma_{11}^3+x_{s,2}\sigma_{22}^3\right)} \end{aligned} \tag{2.26}$$

and $g_1^{SW}\left(\sigma_{ij}\right)$ is determined using the Clausius virial theorem and the first derivative of the free energy with respect to the density [4] giving:

$$g_1^{SW}\left(\sigma_{ij}\right)=\frac{1}{2\pi\varepsilon_{ij}\sigma_{ij}^3}\left[3\left(\frac{\partial\left(a_1\right)_{ij}}{\partial\rho_s}\right)-\frac{\lambda_{ij}}{\rho_s}\frac{\partial\left(a_1\right)_{ij}}{\partial\lambda_{ij}}\right] \tag{2.27}$$

2.2 GC-SAFT-VR EOS for Mixtures

The GC-SAFT-VR approach, which is developed based on the hetero-SAFT-VR approach, also models fluids as chains composed of segments of different size and/or energy. Within the GC-SAFT-VR, *n*-alkanes are modeled as chains of CH_2 groups capped by a CH_3 group at each end. Once parameters for the CH_2 and CH_3 groups have been determined several other key functional groups can be defined and parameterized, allowing us to model a wide range of organic molecules using the GC-SAFT-VR approach. For example to study branched alkanes and ketones only a single additional group is needed in each case; the CH group and the carbonyl (C=O) group respectively. As in the hetero-SAFT-VR approach, the segments representing different types of chemical groups, interact via a square well potential that is characterized by three parameters; the segment diameter σ, well depth ε, and potential range λ. The inter- and intra-molecular cross interactions between segment *i* in chain *k* and segment *j* in chain *l* are obtained from the Lorentz-Berthelot combining rules [89],

$$\sigma_{ki,lj} = \frac{\sigma_{ki,ki} + \sigma_{lj,lj}}{2} \tag{2.28}$$

$$\varepsilon_{ki,lj} = \sqrt{\varepsilon_{ki,ki}\varepsilon_{lj,lj}} \tag{2.29}$$

$$\lambda_{ki,lj} = \frac{\lambda_{ki,ki}\sigma_{ki,ki} + \lambda_{lj,lj}\sigma_{lj,lj}}{\sigma_{ki,ki} + \sigma_{lj,lj}} \tag{2.30}$$

Within the GC-SAFT-VR approach, the free energy is written as the sum of four separate contributions as in equation (1.1). The expressions for a^{assoc} are not included in this work since the systems studied are not associating fluids. The general expressions for each of the remaining terms (i.e., A^{ideal}, A^{mono}, and A^{chain}) for a mixture system

composed of heteronuclear chain molecules are presented below. These expressions can also be simplified to the equations for pure heteronuclear fluids, similarly to those equations given in the previous section 2.1.

The ideal helmholtz free energy is given by

$$\frac{A^{ideal}}{NkT} = \sum_{k=1}^{n} x_k \ln \rho_k \Lambda_k^3 - 1 \tag{2.31}$$

where n represents the number of pure components, $\rho_k = \frac{N_k}{V}$ the number density of chains of component k, x_k the mole fractions of chain k in the mixture, and Λ_k the thermal de Broglie wavelength.

The monomer free energy is given by a second order high temperature expansion using Barker and Henderson perturbation theory for mixtures [90], *viz*,

$$\begin{aligned} \frac{A^{mono}}{NkT} &= \sum_{k=1}^{n}\sum_{i=1}^{n'_k} x_k m_{ki} \frac{A^M}{N_s kT} \\ &= \sum_{k=1}^{n}\sum_{i=1}^{n'_k} x_k m_{ki} a^M = \sum_{k=1}^{n}\sum_{i=1}^{n'_k} x_k m_{ki} \left(a^{HS} + \beta a_1 + \beta^2 a_2 \right) \end{aligned} \tag{2.32}$$

where n'_k is the number of types of segment i in a chain of component k and m_{ki} the number of segments of type i in chains of component k.

The hard sphere reference term a^{HS} uses the same expression as equation (2.8), where ρ_s is the number density of segments, which is defined as N_s/V, the total number of segments divided by the total volume, and ζ_l is the reduced density given by a sum over all segments,

$$\zeta_l = \frac{\pi}{6} \rho_s \left[\sum_{k=1}^{n}\sum_{i=1}^{n'_k} x_{s,ki} (\sigma_{ki})^l \right] \tag{2.33}$$

where σ_{ki} is diameter of segments of type *ki* (i.e., segment i in chain k) and $x_{s,ki}$ the mole fraction of segments of type ki, is expressed as

$$x_{s,ki} = \frac{x_k m_{ki}}{\sum_{k=1}^{n}\sum_{i=1}^{n'_k} x_k m_{ki}} \tag{2.34}$$

The first perturbation term a_1 describing the mean-attractive energy is obtained from the sum of all pair interactions,

$$a_1 = \sum_{l=1}^{n}\sum_{j=1}^{n'_l}\sum_{k=1}^{n}\sum_{i=1}^{n'_k} x_{s,ki} x_{s,lj} \left(a_1\right)_{ki,lj} \tag{2.35}$$

where $\left(a_1\right)_{ki,lj}$ is obtained from the mean-value theorem as proposed by Gil-Villegas *et al.* [4] and expressed through the radial distribution function $g_0^{HS}\left[\sigma_x;\zeta_x^{eff}\left(\lambda_{ki,lj}\right)\right]$ by using the van der Waals one fluid theory,

$$\begin{aligned}\left(a_1\right)_{ki,lj} &= -2\pi\rho_s\varepsilon_{ki,lj}\int_{\sigma_{ki,lj}}^{\infty} r_{ki,lj}^2 g_{ki,lj}^{HS}(r_{ki,lj})dr_{ki,lj} \\ &= -\rho_s\frac{2\pi}{3}\sigma_{ki,lj}^3\varepsilon_{ki,lj}\left(\lambda_{ki,lj}^3-1\right)g_{ki,lj}^{HS}(\sigma_{ki,lj};\zeta_3^{eff}) \\ &= -\rho_s\frac{2\pi}{3}\sigma_{ki,lj}^3\varepsilon_{ki,lj}\left(\lambda_{ki,lj}^3-1\right)g_0^{HS}\left[\sigma_x;\zeta_x^{eff}\left(\lambda_{ki,lj}\right)\right]\end{aligned} \tag{2.36}$$

where $g_0^{HS}(\sigma_x;\zeta_x^{eff})$ has been obtained previously from equation (2.14). The expression for the effective packing fraction ζ_x^{eff} is obtained from the Padé expression proposed by Patel *et al*. [94].

$$\zeta_x^{eff} = \frac{C_1\zeta_x + C_2\zeta_x^{\,2}}{\left(1+C_3\zeta_x\right)^3} \tag{2.37}$$

$$\begin{pmatrix} c_1 \\ c_2 \\ c_3 \end{pmatrix} = \begin{pmatrix} -3.16492 & 13.35007 & -14.80567 & 5.70286 \\ 43.00422 & -191.66232 & 273.89683 & -128.93337 \\ 65.04194 & -266.46273 & 361.04309 & -162.69963 \end{pmatrix} \begin{pmatrix} 1/\lambda_{ki,lj} \\ 1/\lambda_{ki,lj}^{\,2} \\ 1/\lambda_{ki,lj}^{\,3} \\ 1/\lambda_{ki,lj}^{\,4} \end{pmatrix} \quad (2.38)$$

where

$$\begin{aligned} \zeta_x &= \frac{\pi}{6}\rho_s \sigma_x^3 \\ &= \frac{\pi}{6}\rho_s \sum_{l=1}^{n}\sum_{j=1}^{n'_l}\sum_{k=1}^{n}\sum_{i=1}^{n'_k} x_{s,ki} x_{s,lj} \sigma_{ki,lj}^3 \end{aligned} \quad (2.39)$$

The second order perturbation term for the monomer excess free energy a_2 is expressed as:

$$a_2 = \sum_{l=1}^{n}\sum_{j=1}^{n'_l}\sum_{k=1}^{n}\sum_{i=1}^{n'_k} x_{s,ki} x_{s,lj} \left(a_2\right)_{ki,lj} \quad (2.40)$$

where $\left(a_2\right)_{ki,lj}$ is obtained through the local compressibility approximation:

$$\left(a_2\right)_{ki,lj} = \frac{1}{2} K^{HS} \varepsilon_{ki,lj} \rho_s \frac{\partial \left(a_1\right)_{ki,lj}}{\partial \rho_s} \quad (2.41)$$

and K^{HS} is given in equation (2.21).

Here we give the general expression for the chain term a^{chain} for a mixture of heteronuclear molecules,

$$\frac{A^{chain}}{NkT} = -\sum_{k=1}^{n} x_k \sum_{ij \text{ bonds}} \ln y_{ki,kj}^{SW}\left(\sigma_{ki,kj}\right) \quad (2.42)$$

where the sum is over all bonds in the chain molecule. The background correlation function is given by,

$$y_{ki,kj}^{SW}\left(\sigma_{ki,kj}\right) = \exp\left(-\beta\varepsilon_{ki,kj}\right) g_{ki,kj}^{SW}\left(\sigma_{ki,kj}\right) \quad (2.43)$$

where $g_{ki,kj}^{SW}\left(\sigma_{ki,kj}\right)$ is the radial distribution function for the square well monomers and is approximated by a first-order high-temperature perturbation expansion. The exact form of equation (2.22) depends on the number of different types of segments and bonds between segments in the molecules being studied. For example, if we consider a binary mixture of *n*-alkanes: *n*-alkane molecules are composed of CH_3 segments (type1) and CH_2 segments (type2). In this case equation (2.22) becomes:

$$\begin{aligned}\frac{A^{chain}}{NkT} = &-x_1\left[2\ln y_{11,12}^{SW}\left(\sigma_{11,12}\right)+\left(m_{11}-2\right)\ln y_{11,11}^{SW}\left(\sigma_{11,11}\right)+\left(m_{12}-1\right)\ln y_{12,12}^{SW}\left(\sigma_{12,12}\right)\right] \\ &-x_2\left[2\ln y_{21,22}^{SW}\left(\sigma_{21,22}\right)+\left(m_{21}-2\right)\ln y_{21,21}^{SW}\left(\sigma_{21,21}\right)+\left(m_{22}-1\right)\ln y_{22,22}^{SW}\left(\sigma_{22,22}\right)\right]\end{aligned} \quad (2.44)$$

In the case of a single-branched alkane such as 3-ethylpentane, an additional segment (type 3) to represent the CH group is introduced and equation (2.22) becomes:

$$\frac{A^{chain}}{NkT} = -\begin{bmatrix}3\ln y_{1,3}^{SW}\left(\sigma_{1,3}\right)+3\ln y_{2,3}^{SW}\left(\sigma_{2,3}\right)+\left(m_1-3\right)\ln y_{1,1}^{SW}\left(\sigma_{1,1}\right) \\ +\left(m_2-3\right)\ln y_{2,2}^{SW}\left(\sigma_{2,2}\right)+\left(m_3-1\right)\ln y_{3,3}^{SW}\left(\sigma_{3,3}\right)\end{bmatrix} \quad (2.45)$$

Chapter III

VALIDATION OF THE HETERO-SAFT-VR EQUATION

3.1 Introduction

A heteronuclear version of the SAFT-VR equation of state was applied in earlier work to dimer fluids and excellent agreement was obtained between simulation data and theoretical predictions for the PVT behavior of the systems studied [64]. Here we extend the hetero-SAFT-VR approach to chain fluids as a move towards more realistic models of polymers and small molecules composed of different functional groups and rigorously test the predictions against both PVT and phase equilibrium simulation data. The theoretical predictions are compared to isothermal-isobaric (*NPT*) and Gibbs ensemble Monte Carlo (GEMC) simulations of symmetric and asymmetric diblock chain molecules. The remainder of this chapter is organized as follows. In section 3.2 the molecular model systems studied are presented. In section 3.3 details of the simulations performed are given, the results of which are compared to the theoretical predictions in section 3.4. Finally conclusions are drawn in section 3.5.

3.2 Theory and Model Systems Studied

A total of 18 diblock fluids have been studied over a range of state conditions with chain lengths of m = 4, 6, and 8. For each system the diblock chains are composed of segments with different size and/or different energy of interaction. The details of each system studied are given in Table 1.

Table 1: Potential model parameters for the symmetric and asymmetric diblock chain fluids studied. m_1 and m_2 are the number of segments of type 1 and type 2 respectively. σ_2 / σ_1 is the ratio of the hard core diameters of segments of type 2 to type 1, $\varepsilon_2 / \varepsilon_1$ the ratio of the depth of the attractive interaction between segments of type 2 and type 1 and λ the range of the potential.

System	m_2	m_1	σ_2/σ_1	$\varepsilon_2/\varepsilon_1$	λ
1	2	2	1	1.5	1.5
2	2	2	1	0.5	1.5
3	2	2	2	1.5	1.5
4	2	2	2	1.0	1.5
5	2	2	2	0.5	1.5
6	2	2	2	1.0	1.4
7	2	2	2	1.0	1.6
8	4	4	1	1.5	1.5
9	4	4	1	0.5	1.5
10	4	4	2	1.5	1.5
11	4	4	2	1.0	1.5
12	4	4	2	0.5	1.5
13	2	4	2	1.5	1.5
14	2	4	2	1.0	1.5
15	2	4	2	0.5	1.5
16	2	6	2	1.5	1.5
17	2	6	2	1.0	1.5
18	2	6	2	0.5	1.5

We use the hetero-SAFT-VR for pure fluids given in section 2.1 to study the diblock systems in this work. For the specific case of diblock chains equation (2.22) becomes

$$\frac{A^{chain}}{NkT} = -(m_1 - 1)\ln y_{11}^{SW}(\sigma_{11}) - \ln y_{12}^{SW}(\sigma_{12}) - (m_2 - 1)\ln y_{22}^{SW}(\sigma_{22}) \qquad (3.1)$$

3.3 Simulation Details

We have performed Monte Carlo (MC) simulations to determine the *PVT* and phase behavior of 18 model diblock chain fluids (listed in Table 1) to compare with the theoretical predictions and test the accuracy of the hetero-SAFT-VR approach for diblock chains.

Isothermal-isobaric (*NPT*) MC simulations have been performed for each fluid studied at several state conditions to ensure a wide range of temperatures and pressures are examined. Initial configurations were generated by placing molecules on a face centred cubic lattice; simulations at higher pressure, and hence density, were started from this equilibrated configuration and allowed to re-equilibrate to the corresponding density. The simulations were performed with $N = 128$ molecules for all fluids. The usual periodic boundary conditions and minimum image convention were applied. In order to test the *NPT* MC code developed for heteronuclear chain fluids comparisons were made, and agreement achieved, between the results obtained in this work and the work of Gulati and Hall [95], who studied symmetric square-well diblock 4-mer, 8-mer, and 16-mer chains at a single reduced temperature using continuous canonical molecular dynamics.

GEMC simulations have also been performed for selected fluids to determine the fluid phase diagram. The initial configurations for each simulation were taken from equilibrated *NPT* runs at either densities approximately mid way between those for the liquid and vapor phase at each state condition or close to the corresponding theoretical solutions. Simulations were performed with $N = 256$ molecules. As for the *NPT* simulations the usual periodic boundary conditions and minimum image convention were applied.

In both the *NPT* and GEMC simulations one cycle consisted of *N* attempted MC moves (chosen randomly from displacement and reorientation), one volume change and a specified number of attempted re-growths (*NPT*) or insertions (GEMC) of randomly selected molecules using continuum configurational bias sampling [96]. The maximum displacement and volume changes were adjusted to give an acceptance ratio of between 30 and 40 %. The number of attempted re-growths/insertions were controlled so that between 1 and 3% of the molecules are re-grown or inserted each cycle. The thermodynamic properties of the system were obtained as ensemble averages and the errors estimated by determining the standard deviation. An initial simulation of 50,000 - 250,000 cycles was performed to equilibrate the system, depending upon pressure and chain length, before averaging for between 250,000 and 1,000,000 cycles.

3.4 Results

Twelve symmetric and 6 asymmetric diblock chain fluids have been studied; Systems 1 - 7 are symmetric diblock 4-mer fluids, systems 8 - 12 symmetric diblock 8-mer fluids, systems 13 - 15 asymmetric diblock 6-mer fluids, and systems 16 - 18 asymmetric diblock 8-mer fluids. For each chain length we consider molecules in which; the segments are of the same size but have different well depths (systems 1, 2, 8, and 9); the segments are of different sizes but have the same well depth (systems 4, 6, 7, 11, 14 and 17); the segments have different sizes and different values of the well depth (systems 3, 5, 10, 12, 13, 15, 16 and 18). The details of each system are given in Table 1. For each system we have studied isotherms at reduced temperatures of T^*= 2, 3, 4, and 5, where $T^* = kT / \varepsilon_1$. The hetero-SAFT-VR EOS predictions are compared against *NPT* MC

simulation data (reported in Table 2 - Table 5) and GEMC simulation data (given in Table 6 - Table 7).

Table 2: *NPT* MC simulation results for the symmetric diblock 4-mer fluids studied (systems 1 - 7). The reduced temperature is given by $T^* = kT / \varepsilon_1$, the pressure as $P^* = P\sigma_1^3 / \varepsilon_1$, and the energy is defined per segment as $E^* = E / N_s\varepsilon_1$.

System	T^*	P^*	η	E^*	System	T^*	P^*	η	E^*
1	2	2.2134	0.402 ± 0.005	-5.97 ± 0.09	4	4	0.5633	0.304 ± 0.007	-2.99 ± 0.09
	3	0.2327	0.172 ± 0.012	-2.40 ± 0.16			1.8327	0.401 ± 0.005	-4.23 ± 0.08
		1.0840	0.298 ± 0.007	-4.04 ± 0.13		5	0.2691	0.204 ± 0.008	-1.84 ± 0.09
		5.8699	0.402 ± 0.005	-5.81 ± 0.10			0.8170	0.304 ± 0.006	-2.93 ± 0.09
	4	0.6761	0.194 ± 0.008	-2.43 ± 0.12			2.5078	0.401 ± 0.005	-4.19 ± 0.08
		2.4281	0.299 ± 0.006	-3.95 ± 0.12	5	2	0.0767	0.211 ± 0.010	-1.33 ± 0.07
		9.5555	0.402 ± 0.005	-5.72 ± 0.09			0.2340	0.308 ± 0.007	-1.97 ± 0.06
	5	1.1220	0.199 ± 0.008	-2.39 ± 0.12			0.8091	0.402 ± 0.005	-2.71 ± 0.05
		3.7827	0.301 ± 0.006	-3.91 ± 0.11		3	0.1633	0.206 ± 0.008	-1.18 ± 0.06
		13.2528	0.402 ± 0.005	-5.68 ± 0.09			0.4866	0.304 ± 0.007	-1.85 ± 0.06
2	2	0.2417	0.188 ± 0.009	-1.47 ± 0.08			1.4836	0.402 ± 0.005	-2.64 ± 0.05
		0.9536	0.298 ± 0.007	-2.36 ± 0.07		4	0.2499	0.205 ± 0.007	-1.13 ± 0.05
		4.3166	0.402 ± 0.005	-3.40 ± 0.06			0.7408	0.304 ± 0.006	-1.80 ± 0.05
	3	0.6868	0.200 ± 0.008	-1.42 ± 0.07			2.1597	0.402 ± 0.005	-2.59 ± 0.05
		2.3051	0.300 ± 0.006	-2.29 ± 0.06		5	0.3367	0.205 ± 0.007	-1.10 ± 0.05
		8.0106	0.401 ± 0.005	-3.34 ± 0.05			0.9957	0.303 ± 0.006	-1.77 ± 0.05
	4	1.1342	0.201 ± 0.007	-1.37 ± 0.06			2.8364	0.401 ± 0.004	-2.57 ± 0.05
		3.6660	0.302 ± 0.006	-2.27 ± 0.07	6	2	0.0472	0.211 ± 0.013	-1.77 ± 0.11
		11.7152	0.401 ± 0.004	-3.30 ± 0.05			0.1466	0.312 ± 0.009	-2.59 ± 0.10
	5	1.5824	0.202 ± 0.006	-1.34 ± 0.06			0.5894	0.406 ± 0.006	-3.60 ± 0.08
		5.0308	0.302 ± 0.006	-2.25 ± 0.06		3	0.1346	0.207 ± 0.009	-1.51 ± 0.08
		15.4240	0.401 ± 0.004	-3.29 ± 0.05			0.3971	0.307 ± 0.007	-2.37 ± 0.08
3	2	0.2050	0.404 ± 0.006	-6.17 ± 0.11			1.2584	0.404 ± 0.005	-3.44 ± 0.07
	3	0.0343	0.192 ± 0.017	-2.89 ± 0.21		4	0.2218	0.205 ± 0.008	-1.41 ± 0.07
		0.1528	0.308 ± 0.009	-4.35 ± 0.16			0.6503	0.305 ± 0.007	-2.28 ± 0.08
		0.8660	0.402 ± 0.005	-5.93 ± 0.10			1.9318	0.402 ± 0.005	-3.37 ± 0.07
	4	0.1204	0.203 ± 0.010	-2.71 ± 0.14		5	0.3088	0.204 ± 0.007	-1.35 ± 0.07
		0.4022	0.306 ± 0.008	-4.15 ± 0.14			0.9045	0.305 ± 0.006	-2.23 ± 0.07
		1.5353	0.401 ± 0.005	-5.78 ± 0.10			2.6070	0.402 ± 0.005	-3.34 ± 0.07
	5	0.2068	0.205 ± 0.009	-2.59 ± 0.13	7	2	0.3987	0.402 ± 0.005	-5.46 ± 0.08
		0.6542	0.305 ± 0.007	-4.04 ± 0.13		3	0.0546	0.206 ± 0.013	-2.72 ± 0.16
		2.2080	0.401 ± 0.005	-5.72 ± 0.10			0.2266	0.307 ± 0.008	-3.95 ± 0.12
4	2	0.0099	0.119 ± 0.039	-1.75 ± 0.33			1.0668	0.401 ± 0.005	-5.28 ± 0.08
		0.0625	0.307 ± 0.011	-3.31 ± 0.13		4	0.1404	0.206 ± 0.010	-2.53 ± 0.13
		0.4905	0.403 ± 0.005	-4.46 ± 0.08			0.4783	0.305 ± 0.007	-3.80 ± 0.11
	3	0.0960	0.206 ± 0.010	-2.05 ± 0.11			1.7398	0.401 ± 0.005	-5.20 ± 0.08
		0.3111	0.306 ± 0.007	-3.09 ± 0.10		5	0.2266	0.205 ± 0.008	-2.42 ± 0.11
		1.1594	0.402 ± 0.005	-4.31 ± 0.08			0.7316	0.304 ± 0.006	-3.74 ± 0.10
	4	0.1825	0.206 ± 0.008	-1.92 ± 0.10			2.4147	0.401 ± 0.005	-5.16 ± 0.08

Table 3: *NPT* MC simulation results for the symmetric diblock 8-mer fluids studied (systems 8 - 12). The properties are defined as for Table 2.

System	T^*	P^*	η	E^*	System	T^*	P^*	η	E^*
8	2	1.6202	0.395 ± 0.004	-5.60 ± 0.10	11	2	0.0028	0.296 ± 0.012	-3.18 ± 0.11
	3	0.0360	0.088 ± 0.031	-1.73 ± 0.29			0.3728	0.399 ± 0.004	-4.26 ± 0.06
		0.6444	0.295 ± 0.005	-3.86 ± 0.09		3	0.0514	0.202 ± 0.009	-2.02 ± 0.09
		5.0170	0.400 ± 0.005	-5.57 ± 0.11			0.2186	0.309 ± 0.006	-3.01 ± 0.08
	4	0.4009	0.266 ± 0.009	-3.48 ± 0.12			0.9855	0.401 ± 0.004	-4.14 ± 0.06
		1.8370	0.300 ± 0.005	-3.81 ± 0.08		4	0.1208	0.206 ± 0.007	-1.88 ± 0.07
		8.4412	0.399 ± 0.004	-5.46 ± 0.10			0.4381	0.307 ± 0.005	-2.88 ± 0.07
	5	0.7684	0.199 ± 0.006	-2.33 ± 0.09			1.6025	0.402 ± 0.003	-4.09 ± 0.05
		3.0404	0.302 ± 0.004	-3.76 ± 0.08		5	0.1904	0.208 ± 0.007	-1.82 ± 0.07
		11.8767	0.399 ± 0.004	-5.42 ± 0.07			0.6591	0.306 ± 0.005	-2.82 ± 0.07
9	2	0.1089	0.176 ± 0.010	-1.42 ± 0.07			2.2213	0.401 ± 0.003	-4.05 ± 0.05
		0.6600	0.297 ± 0.005	-2.28 ± 0.05	12	2	0.0480	0.215 ± 0.009	-1.42 ± 0.06
		3.7508	0.397 ± 0.004	-3.24 ± 0.05			0.1739	0.309 ± 0.005	-1.98 ± 0.05
	3	0.4755	0.200 ± 0.006	-1.39 ± 0.05			0.6924	0.401 ± 0.003	-2.65 ± 0.03
		1.8601	0.302 ± 0.004	-2.22 ± 0.04		3	0.1176	0.211 ± 0.006	-1.23 ± 0.04
		7.1833	0.399 ± 0.003	-3.20 ± 0.04			0.3937	0.308 ± 0.005	-1.85 ± 0.04
	4	0.8446	0.203 ± 0.005	-1.34 ± 0.05			1.3106	0.401 ± 0.003	-2.58 ± 0.03
		3.0698	0.303 ± 0.004	-2.19 ± 0.05		4	0.1872	0.210 ± 0.006	-1.16 ± 0.04
		10.6258	0.398 ± 0.003	-3.17 ± 0.04			0.6152	0.307 ± 0.004	-1.79 ± 0.04
	5	1.2145	0.204 ± 0.005	-1.31 ± 0.04			1.9304	0.401 ± 0.003	-2.54 ± 0.03
		4.2834	0.303 ± 0.004	-2.17 ± 0.04		5	0.2570	0.208 ± 0.005	-1.11 ± 0.04
		14.0724	0.398 ± 0.003	-3.15 ± 0.04			0.8373	0.305 ± 0.005	-1.74 ± 0.04
10	2	0.0858	0.396 ± 0.003	-5.73 ± 0.07			2.5509	0.400 ± 0.003	-2.52 ± 0.03
	3	0.0613	0.303 ± 0.008	-4.11 ± 0.12					
		0.6906	0.401 ± 0.003	-5.63 ± 0.07					
	4	0.0603	0.195 ± 0.010	-2.57 ± 0.12					
		0.2779	0.306 ± 0.006	-3.95 ± 0.10					
		1.3037	0.399 ± 0.003	-5.49 ± 0.06					
	5	0.1296	0.203 ± 0.007	-2.48 ± 0.10					
		0.4972	0.307 ± 0.005	-3.86 ± 0.09					
		1.9201	0.400 ± 0.003	-5.44 ± 0.06					

Table 4: *NPT* MC simulation results for the asymmetric diblock 6-mer (systems 13-15) and 8-mer (systems 16-18) fluids studied. The properties are defined as for Table 2.

System	T^*	P^*	η	E^*	System	T^*	P^*	η	E^*
13	2	0.2135	0.405 ± 0.004	-5.65 ± 0.08	16	2	0.2443	0.398 ± 0.004	-5.24 ± 0.07
	3	0.0249	0.181 ± 0.018	-2.62 ± 0.18		3	0.0183	0.196 ± 0.012	-2.63 ± 0.12
		0.1611	0.311 ± 0.008	-4.00 ± 0.12			0.1745	0.307 ± 0.007	-3.73 ± 0.10
		1.0170	0.405 ± 0.005	-5.44 ± 0.08			1.1804	0.401 ± 0.004	-5.11 ± 0.06
	4	0.1231	0.205 ± 0.009	-2.52 ± 0.12		4	0.1275	0.206 ± 0.008	-2.41 ± 0.10
		0.4569	0.307 ± 0.007	-3.79 ± 0.11			0.5132	0.310 ± 0.006	-3.62 ± 0.09
		1.8309	0.404 ± 0.005	-5.31 ± 0.08			2.1280	0.400 ± 0.004	-5.00 ± 0.06
	5	0.2215	0.206 ± 0.008	-2.40 ± 0.11		5	0.2370	0.208 ± 0.008	-2.30 ± 0.09
		0.7557	0.307 ± 0.006	-3.69 ± 0.10			0.8554	0.307 ± 0.005	-3.49 ± 0.08
		2.6488	0.404 ± 0.004	-5.24 ± 0.08			3.0803	0.401 ± 0.003	-4.97 ± 0.06
14	2	0.0315	0.311 ± 0.009	-3.33 ± 0.10	17	2	0.0048	0.312 ± 0.009	-3.32 ± 0.08
		0.5088	0.405 ± 0.005	-4.36 ± 0.07			0.5408	0.402 ± 0.004	-4.28 ± 0.06
	3	0.0898	0.209 ± 0.009	-2.09 ± 0.09		3	0.0844	0.211 ± 0.009	-2.11 ± 0.09
		0.3252	0.309 ± 0.007	-3.05 ± 0.09			0.3403	0.308 ± 0.006	-2.99 ± 0.08
		1.3208	0.404 ± 0.004	-4.20 ± 0.07			1.4853	0.403 ± 0.004	-4.16 ± 0.05
	4	0.1883	0.208 ± 0.007	-1.93 ± 0.08		4	0.1939	0.209 ± 0.008	-1.92 ± 0.08
		0.6238	0.306 ± 0.006	-2.92 ± 0.08			0.6818	0.306 ± 0.005	-2.87 ± 0.07
		2.1388	0.403 ± 0.004	-4.11 ± 0.06			2.4372	0.400 ± 0.005	-4.06 ± 0.05
	5	0.2869	0.208 ± 0.007	-1.85 ± 0.07		5	0.3035	0.208 ± 0.005	-1.83 ± 0.06
		0.9243	0.306 ± 0.005	-2.85 ± 0.07			1.0256	0.307 ± 0.005	-2.81 ± 0.07
		2.9593	0.403 ± 0.004	-4.06 ± 0.06			3.3920	0.401 ± 0.003	-4.01 ± 0.05
15	2	0.0653	0.219 ± 0.009	-1.64 ± 0.07	18	2	0.0523	0.220 ± 0.009	-1.83 ± 0.07
		0.2171	0.311 ± 0.006	-2.24 ± 0.06			0.1973	0.312 ± 0.007	-2.41 ± 0.06
		0.8519	0.404 ± 0.004	-2.98 ± 0.05			0.8940	0.403 ± 0.004	-3.17 ± 0.05
	3	0.1639	0.212 ± 0.007	-1.40 ± 0.06		3	0.1620	0.211 ± 0.006	-1.51 ± 0.05
		0.5151	0.307 ± 0.006	-2.06 ± 0.05			0.5372	0.309 ± 0.005	-2.20 ± 0.05
		1.6703	0.404 ± 0.004	-2.87 ± 0.04			1.8454	0.403 ± 0.003	-3.04 ± 0.03
	4	0.2626	0.209 ± 0.006	-1.30 ± 0.05		4	0.2717	0.211 ± 0.007	-1.41 ± 0.05
		0.8158	0.306 ± 0.005	-1.99 ± 0.05			0.8809	0.307 ± 0.005	-2.10 ± 0.05
		2.4916	0.404 ± 0.004	-2.83 ± 0.05			2.8006	0.402 ± 0.004	-2.98 ± 0.04
	5	0.3613	0.208 ± 0.006	-1.26 ± 0.05		5	0.3815	0.209 ± 0.005	-1.34 ± 0.05
		1.1176	0.306 ± 0.005	-1.95 ± 0.05			1.2260	0.306 ± 0.005	-2.05 ± 0.05
		3.3140	0.403 ± 0.004	-2.79 ± 0.05			3.7575	0.403 ± 0.003	-2.96 ± 0.04

Table 5: *NPT* MC simulation results along the coexistence curve for selected symmetric diblock 4-mer and 8-mer fluids. The properties are defined as for Table 2.

System	T^*	η	E^*
3	1.2	0.452 ± 0.004	-7.31 ± 0.07
	1.3	0.442 ± 0.005	-7.10 ± 0.08
	1.4	0.433 ± 0.005	-6.90 ± 0.08
	1.5	0.423 ± 0.006	-6.72 ± 0.10
	1.6	0.413 ± 0.005	-6.50 ± 0.10
	1.7	0.403 ± 0.006	-6.30 ± 0.11
4	0.9	0.451 ± 0.004	-5.46 ± 0.05
	1.0	0.438 ± 0.005	-5.23 ± 0.06
	1.1	0.424 ± 0.005	-5.03 ± 0.07
	1.2	0.410 ± 0.006	-4.81 ± 0.08
	1.3	0.397 ± 0.007	-4.62 ± 0.09
5	0.76	0.402 ± 0.008	-3.13 ± 0.06
	0.80	0.394 ± 0.007	-3.04 ± 0.06
10	1.8	0.401 ± 0.003	-5.86 ± 0.07
	1.9	0.395 ± 0.004	-5.82 ± 0.08
	2.0	0.388 ± 0.004	-5.70 ± 0.07
	2.1	0.380 ± 0.006	-5.54 ± 0.09
	2.2	0.373 ± 0.005	-5.40 ± 0.09
	2.3	0.358 ± 0.006	-5.13 ± 0.10
11	1.3	0.403 ± 0.004	-4.48 ± 0.07
	1.4	0.393 ± 0.003	-4.35 ± 0.07
	1.5	0.389 ± 0.004	-4.28 ± 0.07
	1.6	0.374 ± 0.005	-4.11 ± 0.06
	1.7	0.358 ± 0.006	-3.91 ± 0.07
12	0.86	0.392 ± 0.003	-2.89 ± 0.03
	0.90	0.382 ± 0.004	-2.85 ± 0.05
	0.95	0.370 ± 0.005	-2.79 ± 0.04
	1.00	0.356 ± 0.009	-2.73 ± 0.06
	1.05	0.344 ± 0.010	-2.66 ± 0.05

Table 6: GEMC simulation results for selected symmetric diblock 4-mer and 8-mer fluids. The fixed variables during the simulation are defined as for Table 2. The densities η, number of molecules *N* and reduced energies per segment $E*$ in the coexisting vapor and liquid phases are labeled *v* and *l*, respectively.

System	T^*	η_L	η_v	N_L	N_v	E_L^*	E_v^*
3	1.7	0.403 ± 0.006	0.0005 ± 0.0000	138	118	-6.28 ± 0.11	-0.49 ± 0.03
	1.8	0.391 ± 0.004	0.0011 ± 0.0004	240	16	-6.05 ± 0.08	-0.54 ± 0.11
	1.9	0.382 ± 0.005	0.0023 ± 0.0010	228	28	-5.86 ± 0.10	-0.60 ± 0.11
	2.0	0.371 ± 0.007	0.0034 ± 0.0003	193	63	-5.64 ± 0.11	-0.62 ± 0.07
	2.1	0.356 ± 0.008	0.0054 ± 0.0008	182	74	-5.36 ± 0.14	-0.66 ± 0.07
	2.2	0.343 ± 0.009	0.0097 ± 0.0007	177	79	-5.14 ± 0.14	-0.78 ± 0.09
	2.3	0.324 ± 0.013	0.0159 ± 0.0016	69	187	-4.82 ± 0.20	-0.92 ± 0.11
	2.4	0.304 ± 0.012	0.0292 ± 0.0082	224	32	-4.49 ± 0.16	-1.16 ± 0.28
4	1.3	0.396 ± 0.004	0.0006 ± 0.0002	251	5	-4.60 ± 0.05	-0.44 ± 0.14
	1.4	0.379 ± 0.006	0.0015 ± 0.0004	245	11	-4.37 ± 0.07	-0.46 ± 0.10
	1.5	0.362 ± 0.006	0.0034 ± 0.0005	228	28	-4.13 ± 0.08	-0.50 ± 0.08
	1.6	0.343 ± 0.009	0.0080 ± 0.0011	166	90	-3.87 ± 0.10	-0.60 ± 0.08
	1.7	0.319 ± 0.012	0.0159 ± 0.0028	190	66	-3.58 ± 0.12	-0.74 ± 0.10
	1.8	0.277 ± 0.018	0.0284 ± 0.0076	223	33	-3.17 ± 0.14	-0.89 ± 0.20
5	0.80	0.394 ± 0.005	0.0007 ± 0.0003	251	5	-3.04 ± 0.04	-0.37 ± 0.12
	0.85	0.381 ± 0.006	0.0023 ± 0.0007	243	13	-2.94 ± 0.05	-0.46 ± 0.17
	0.90	0.366 ± 0.006	0.0024 ± 0.0006	238	18	-2.79 ± 0.04	-0.40 ± 0.09
	0.95	0.352 ± 0.008	0.0051 ± 0.0008	202	54	-2.66 ± 0.06	-0.45 ± 0.08
	1.00	0.330 ± 0.010	0.0101 ± 0.0009	165	91	-2.49 ± 0.07	-0.56 ± 0.08
	1.05	0.307 ± 0.015	0.0201 ± 0.0049	184	72	-2.33 ± 0.08	-0.71 ± 0.14
	1.10	0.268 ± 0.019	0.0285 ± 0.0092	229	27	-2.11 ± 0.09	-0.72 ± 0.20
10	2.3	0.361 ± 0.006	0.0069 ± 0.0002	141	115	-5.18 ± 0.09	-2.48 ± 0.34
	2.4	0.352 ± 0.007	0.0030 ± 0.0001	98	158	-5.00 ± 0.11	-1.07 ± 0.05
	2.5	0.327 ± 0.011	0.0031 ± 0.0002	93	163	-4.62 ± 0.15	-1.02 ± 0.08
	2.68	0.294 ± 0.019	0.0101 ± 0.0008	64	192	-4.15 ± 0.22	-1.14 ± 0.07
11	1.70	0.358 ± 0.005	0.0025 ± 0.0001	142	114	-3.90 ± 0.06	-0.86 ± 0.04
	1.78	0.343 ± 0.008	0.0026 ± 0.0001	133	123	-3.72 ± 0.09	-0.82 ± 0.12
	1.85	0.335 ± 0.008	0.0061 ± 0.0002	146	110	-3.61 ± 0.09	-0.93 ± 0.06
	1.90	0.315 ± 0.010	0.0069 ± 0.0004	142	114	-3.38 ± 0.10	-0.91 ± 0.09
	1.95	0.299 ± 0.014	0.0077 ± 0.0004	116	140	-3.24 ± 0.12	-0.92 ± 0.06
	2.05	0.238 ± 0.074	0.0190 ± 0.0039	101	155	-2.71 ± 0.55	-1.07 ± 0.09
12	0.95	0.374 ± 0.005	0.0026 ± 0.0000	130	126	-2.85 ± 0.04	-2.19 ± 0.08
	1.00	0.358 ± 0.007	0.0027 ± 0.0001	123	133	-2.79 ± 0.05	-2.14 ± 0.07
	1.05	0.341 ± 0.008	0.0070 ± 0.0002	136	120	-2.62 ± 0.04	-2.09 ± 0.06
	1.10	0.337 ± 0.008	0.0057 ± 0.0004	172	84	-2.57 ± 0.05	-1.39 ± 0.12
	1.15	0.315 ± 0.011	0.0067 ± 0.0004	147	109	-2.42 ± 0.08	-1.07 ± 0.08
	1.20	0.288 ± 0.015	0.0084 ± 0.0004	97	159	-2.26 ± 0.09	-0.84 ± 0.06
	1.25	0.269 ± 0.015	0.0378 ± 0.0041	156	100	-2.15 ± 0.07	-1.34 ± 0.09

Table 7: GEMC simulation results for asymmetric diblock 6-mer and 8-mer fluids. See Table 6 for details.

System	T^*	η_L	η_v	N_L	N_v	E_L^*	E_v^*
13	2.10	0.363 ± 0.006	0.0021 ± 0.0001	131	125	-5.00 ± 0.10	-0.84 ± 0.08
	2.20	0.351 ± 0.009	0.0039 ± 0.0001	131	125	-4.82 ± 0.13	-0.80 ± 0.11
	2.30	0.335 ± 0.012	0.0070 ± 0.0006	92	164	-4.55 ± 0.17	-0.93 ± 0.07
	2.40	0.315 ± 0.011	0.0106 ± 0.0007	141	115	-4.26 ± 0.13	-1.00 ± 0.07
	2.45	0.307 ± 0.016	0.0151 ± 0.0016	83	173	-4.14 ± 0.19	-1.08 ± 0.07
14	1.50	0.386 ± 0.007	0.0007 ± 0.0000	135	121	-4.31 ± 0.09	-0.72 ± 0.13
	1.60	0.371 ± 0.006	0.0020 ± 0.0000	138	118	-4.12 ± 0.08	-0.76 ± 0.08
	1.65	0.364 ± 0.006	0.0036 ± 0.0001	144	112	-4.02 ± 0.08	-0.64 ± 0.10
	1.70	0.354 ± 0.007	0.0039 ± 0.0001	128	128	-3.88 ± 0.08	-0.69 ± 0.12
	1.80	0.333 ± 0.009	0.0095 ± 0.0010	181	75	-3.63 ± 0.10	-0.91 ± 0.07
	1.85	0.317 ± 0.012	0.0105 ± 0.0007	133	123	-3.46 ± 0.12	-0.90 ± 0.06
	1.90	0.297 ± 0.017	0.0133 ± 0.0013	68	168	-3.27 ± 0.15	-0.92 ± 0.06
15	1.00	0.384 ± 0.007	0.0007 ± 0.0000	151	105	-3.25 ± 0.07	-0.79 ± 0.12
	1.05	0.371 ± 0.007	0.0018 ± 0.0001	151	105	-3.14 ± 0.06	-1.12 ± 0.13
	1.10	0.350 ± 0.010	0.0037 ± 0.0002	148	108	-3.00 ± 0.08	-1.57 ± 0.24
	1.15	0.342 ± 0.010	0.0072 ± 0.0007	157	99	-2.91 ± 0.08	-1.38 ± 0.16
	1.17	0.331 ± 0.010	0.0082 ± 0.0007	156	100	-2.82 ± 0.08	-1.38 ± 0.14
	1.20	0.328 ± 0.009	0.0082 ± 0.0009	177	79	-2.79 ± 0.07	-0.95 ± 0.10
	1.23	0.308 ± 0.013	0.0084 ± 0.0015	177	79	-2.67 ± 0.07	-0.87 ± 0.09
	1.25	0.300 ± 0.017	0.0119 ± 0.0008	129	127	-2.62 ± 0.08	-1.03 ± 0.11
16	2.10	0.360 ± 0.007	0.0007 ± 0.0000	109	147	-4.71 ± 0.11	-0.91 ± 0.13
	2.20	0.354 ± 0.007	0.0021 ± 0.0001	136	120	-4.57 ± 0.11	-0.94 ± 0.09
	2.30	0.338 ± 0.009	0.0033 ± 0.0001	124	132	-4.36 ± 0.12	-0.97 ± 0.06
	2.40	0.312 ± 0.014	0.0053 ± 0.0003	104	152	-4.00 ± 0.16	-0.99 ± 0.07
	2.50	0.303 ± 0.013	0.0131 ± 0.0007	110	146	-3.87 ± 0.16	-1.15 ± 0.06
17	1.55	0.386 ± 0.005	0.0002 ± 0.0000	132	124	-4.24 ± 0.07	-0.81 ± 0.19
	1.60	0.376 ± 0.005	0.0004 ± 0.0000	138	118	-4.12 ± 0.06	-0.88 ± 0.14
	1.65	0.369 ± 0.007	0.0006 ± 0.0000	106	150	-4.01 ± 0.08	-0.83 ± 0.15
	1.70	0.363 ± 0.007	0.0011 ± 0.0000	113	143	-3.96 ± 0.08	-0.86 ± 0.14
	1.75	0.355 ± 0.008	0.0022 ± 0.0001	109	147	-3.83 ± 0.08	-0.93 ± 0.08
	1.80	0.340 ± 0.008	0.0020 ± 0.0001	137	119	-3.67 ± 0.08	-0.90 ± 0.07
	1.85	0.333 ± 0.011	0.0038 ± 0.0002	89	167	-3.58 ± 0.12	-0.94 ± 0.06
	1.90	0.319 ± 0.005	0.0108 ± 0.0003	110	146	-3.44 ± 0.09	-0.92 ± 0.08
18	1.20	0.361 ± 0.007	0.0010 ± 0.0000	126	130	-3.22 ± 0.08	-0.91 ± 0.08
	1.25	0.348 ± 0.008	0.0014 ± 0.0001	148	108	-3.12 ± 0.07	-0.96 ± 0.08
	1.30	0.331 ± 0.009	0.0031 ± 0.0001	151	105	-3.01 ± 0.06	-1.01 ± 0.07
	1.35	0.313 ± 0.011	0.0050 ± 0.0006	162	94	-2.87 ± 0.07	-1.06 ± 0.13
	1.40	0.303 ± 0.011	0.0109 ± 0.0005	135	121	-2.74 ± 0.06	-1.16 ± 0.08

In Figure 1 we present the isotherms studied for the diblock 4-mer fluids (systems 1 and 2) composed of segments with equal diameters ($\sigma_2 = \sigma_1$), a potential range of $\lambda_1 = \lambda_2 = 1.5$, and different well depths $\varepsilon_2 \neq \varepsilon_1$. From the figure we see that system 1 (Figure 1a) which has a higher ratio of $\varepsilon_2 / \varepsilon_1 = 1.5$ than system 2 (Figure 1b), displays higher densities at a given pressure. We observe good agreement between the simulation results and theoretical predictions over a wide range of temperatures and pressures.

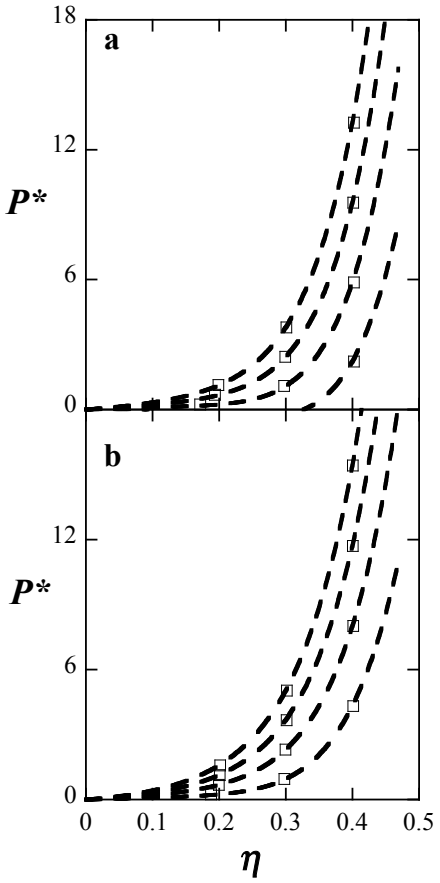

Figure 1: Isotherms for symmetric diblock 4-mer fluids with a) diameter $\sigma_2 = \sigma_1$, well depth $\varepsilon_2 = 1.5\varepsilon_1$ and range $\lambda_1 = \lambda_2 = 1.5$ (system 1) and b) diameter $\sigma_2 = \sigma_1$, well depth $\varepsilon_2 = 0.5\varepsilon_1$ and range $\lambda_1 = \lambda_2 = 1.5$ (system 2). SAFT-VR EOS results at T*= 2.0, 3.0, 4.0, 5.0 (from bottom to top) are represented as continuous curves and the squares represent the *NPT* MC simulation data.

In contrast, Figure 2 presents isotherms for diblock 4-mer fluids (systems 3 - 5) composed of segments with a size ratio of $\sigma_2 / \sigma_1 = 2$, a potential range of $\lambda_1 = \lambda_2 = 1.5$ and differing well depths. System 3 in Figure 2a has the highest ratio of interaction energies, $\varepsilon_2 / \varepsilon_1 = 1.5$, and system 5 (Figure 2c) the lowest, $\varepsilon_2 / \varepsilon_1 = 0.5$. We again observe that the system with the higher ratio of well depths is denser at a given pressure; however, in contrast to system 1, system 3 has much larger densities under the same pressures due to size effects. Similar behavior is expected and observed for system 5 compared to system 2. Again, in all cases excellent agreement is observed between the theoretical predictions and the simulation data.

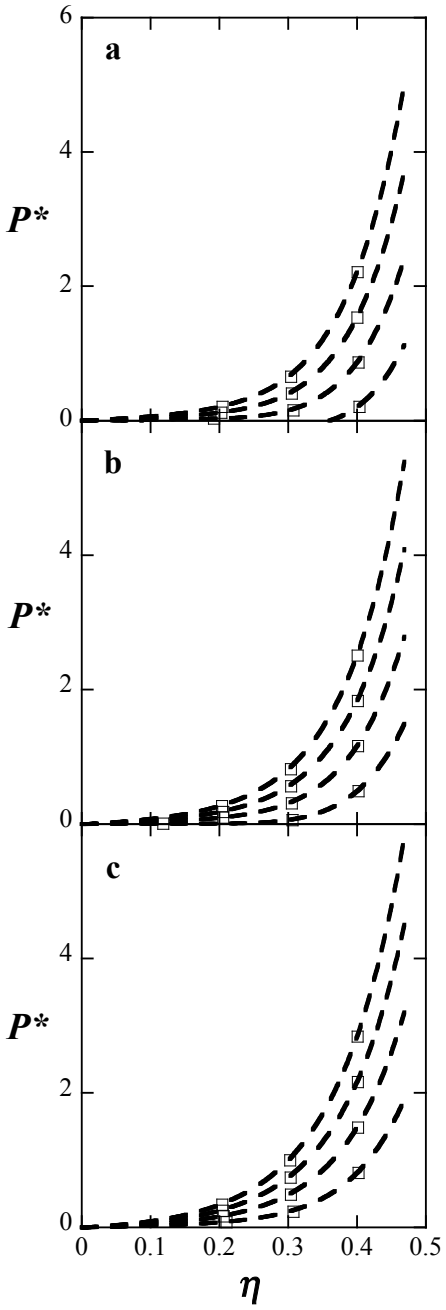

Figure 2: Isotherms for symmetric diblock 4-mer fluids with a) diameter $\sigma_2 = 2\sigma_1$, well depth $\varepsilon_2 = 1.5\varepsilon_1$ and range $\lambda_1 = \lambda_2 = 1.5$ (system 3), b) diameter $\sigma_2 = 2\sigma_1$, well depth $\varepsilon_2 = \varepsilon_1$ and range $\lambda_1 = \lambda_2 = 1.5$ (system 4) and c) diameter $\sigma_2 = 2\sigma_1$, well depth $\varepsilon_2 = 0.5\varepsilon_1$ and range $\lambda_1 = \lambda_2 = 1.5$ (system 5). Hetero-SAFT-VR EOS results at T*= 2.0, 3.0, 4.0, 5.0 (from bottom to top) are represented as continuous curves and the symbols represent the *NPT* MC simulation data.

To test the effect of the range of the potential on the *PVT* and phase behavior, in Figure 3 we also present results for 4-mer fluids that have the same size ratio ($\sigma_2 / \sigma_1 = 2$) and equal well depth ($\varepsilon_2 = \varepsilon_1$), but different potential range ($\lambda_1 = \lambda_2 = 1.6$ and $\lambda_1 = \lambda_2 = 1.4$). From the figure we can see that system 7, which has the greatest potential range ($\lambda = 1.6$), exhibits a higher density at a given pressure compared to system 6 which has a shorter potential range ($\lambda = 1.4$).

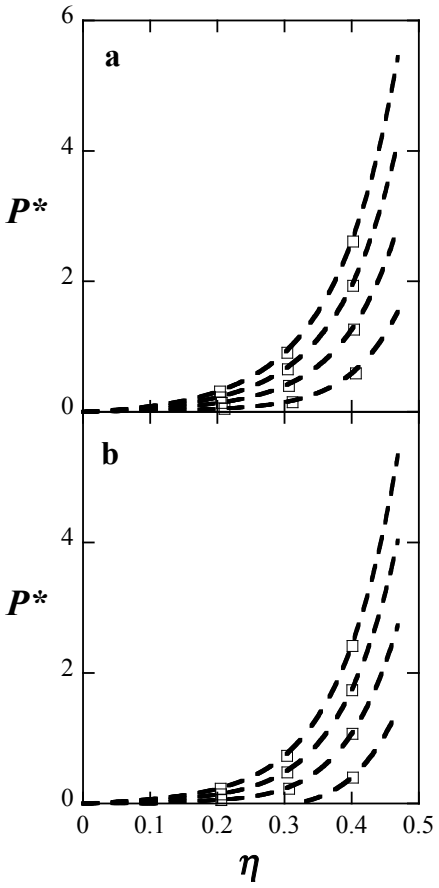

Figure 3: Isotherms for symmetric diblock 4-mer fluids with a) diameter $\sigma_2 = 2\sigma_1$, well depth $\varepsilon_2 = \varepsilon_1$ and range $\lambda_1 = \lambda_2 = 1.4$ (system 6), b) diameter $\sigma_2 = 2\sigma_1$, well depth $\varepsilon_2 = \varepsilon_1$ and range $\lambda_1 = \lambda_2 = 1.6$ (system 7). Hetero-SAFT-VR EOS results at T*= 2.0, 3.0, 4.0, 5.0 (from bottom to top) are represented as continuous curves and the symbols represent the *NPT* MC simulation data.

If we consider longer chain lengths, the isotherms for 8-mer fluids are presented in Figure 4 and Figure 5. Similar trends are seen in the isotherms as a function of the size ratio and interaction energy for the 8-mer systems as for the 4-mer fluids. Again excellent agreement is in general observed between the theoretical predictions and the simulation data, though slight deviations are seen at low densities for the systems studied in Figure 4. We can also note from the figures that at a given pressure the densities for the 8-mer fluids are slightly higher than those observed for the corresponding 4-mer systems, due to chain length effects.

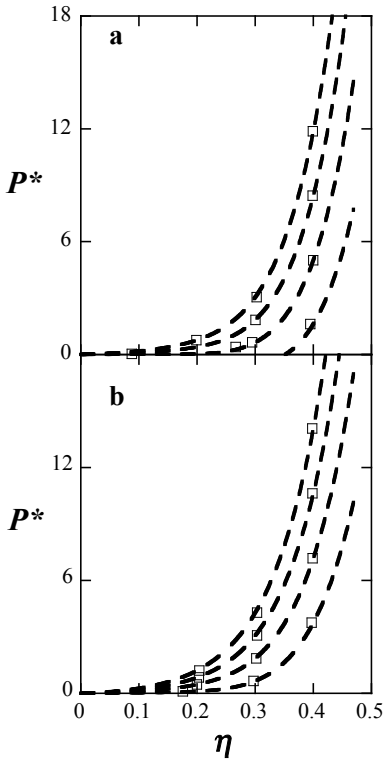

Figure 4: Isotherms for symmetric diblock 8-mer fluids with a) diameter $\sigma_2 = \sigma_1$, well depth $\varepsilon_2 = 1.5\varepsilon_1$ and range $\lambda_1 = \lambda_2 = 1.5$ (system 8) and b) diameter $\sigma_2 = \sigma_1$, well depth $\varepsilon_2 = 0.5\varepsilon_1$ and range $\lambda_1 = \lambda_2 = 1.5$ (system 9). Hetero-SAFT-VR EOS results at T*= 2.0, 3.0, 4.0, 5.0 (from bottom to top) are represented as continuous curves and the symbols represent the *NPT* MC simulation data.

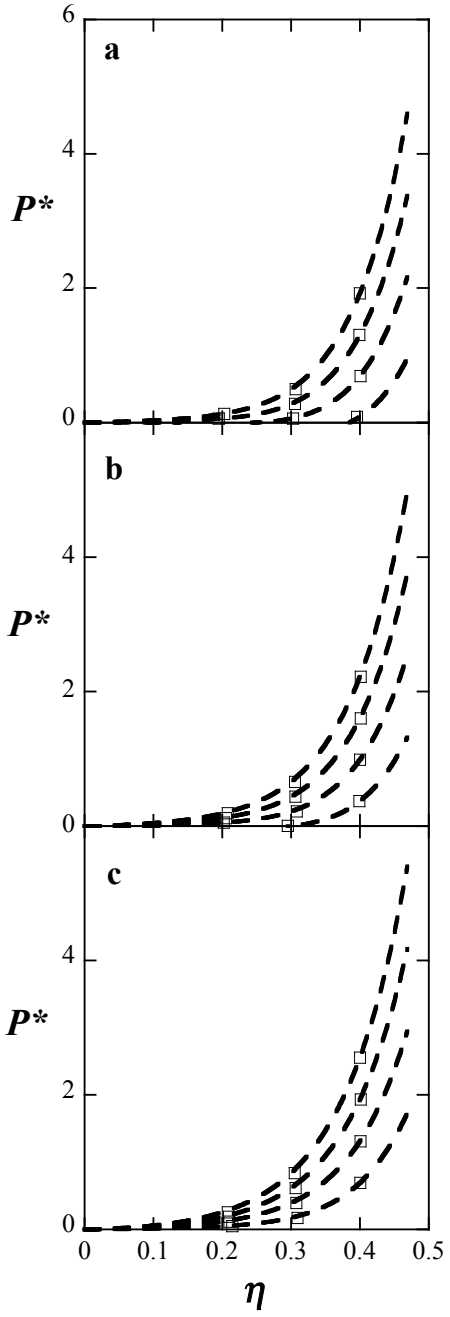

Figure 5: Isotherms for symmetric diblock 8-mer fluids with a) diameter $\sigma_2 = 2\sigma_1$, well depth $\varepsilon_2 = 1.5\varepsilon_1$ and range $\lambda_1 = \lambda_2 = 1.5$ (system 10), b) diameter $\sigma_2 = 2\sigma_1$, well depth $\varepsilon_2 = \varepsilon_1$ and range $\lambda_1 = \lambda_2 = 1.5$ (system 11) and c) diameter $\sigma_2 = 2\sigma_1$, well depth $\varepsilon_2 = 0.5\varepsilon_1$ and range $\lambda_1 = \lambda_2 = 1.5$ (system 12). Hetero-SAFT-VR EOS results at T*= 2.0, 3.0, 4.0, 5.0 (from bottom to top) are represented as continuous curves and the symbols represent the *NPT* MC simulation data.

To examine the effect of symmetry on the isotherms we have studied a number of asymmetric 6-mer (systems 13 - 15) and 8-mer fluids (systems 16 - 18), the results of which are presented in Figure 6 and Figure 7 respectively. For each chain length, each system studied has the same asymmetric molecular structure with $\sigma_2 / \sigma_1 = 2$, a potential range of $\lambda_1 = \lambda_2 = 1.5$ but different ratios of the well depths ($\varepsilon_2 / \varepsilon_1$). Good agreement is observed between the theory and simulation for each system studied. We also note from the figures that increasing the fraction of the smaller segments (m_1) within a molecule results in lower densities at a given pressure. For example, the asymmetric 8-mer fluids (systems 16 - 18) have a higher fraction of small segments than the symmetric 8-mer fluids (systems 10 - 12), and therefore lower densities at a given pressure (comparing systems with the same ratio of $\varepsilon_2 / \varepsilon_1$). Similarly if we consider the asymmetric 6-mer fluids (systems 13 - 15), which have a lower fraction of small segments than the asymmetric 8-mer fluids (systems 16 - 18), for the same ratio of $\varepsilon_2 / \varepsilon_1$ the asymmetric 6-mer systems have higher densities at a given pressure than the corresponding asymmetric 8-mer systems, despite having less segments per molecule.

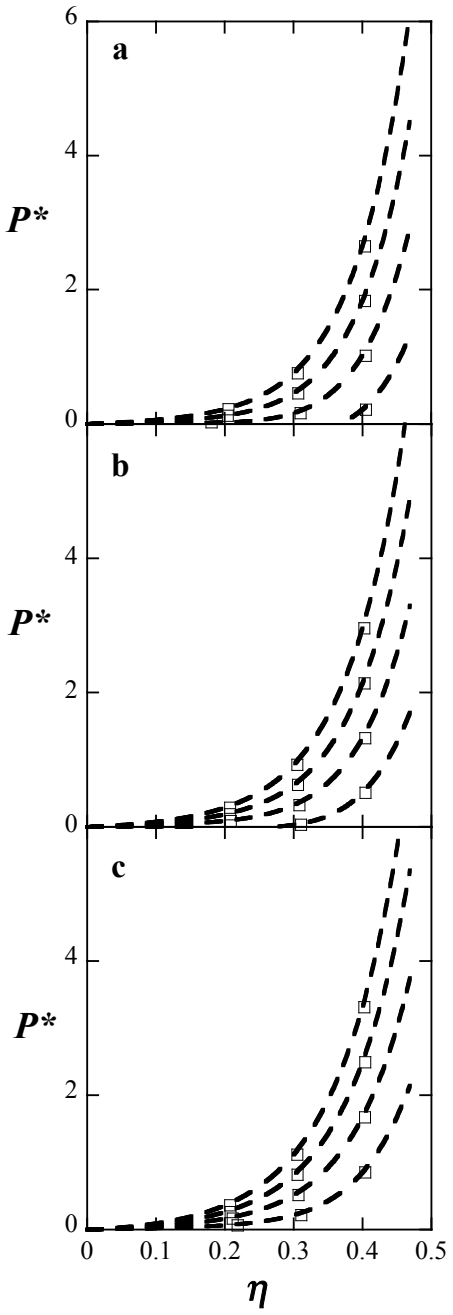

Figure 6: Isotherms for asymmetric diblock 6-mer fluids with $m_1 = 4$, $m_2 = 2$ and a) diameter $\sigma_2 = 2\sigma_1$, well depth $\varepsilon_2 = 1.5\varepsilon_1$ and range $\lambda_1 = \lambda_2 = 1.5$ (system 13), b) diameter $\sigma_2 = 2\sigma_1$, well depth $\varepsilon_2 = \varepsilon_1$ and range $\lambda_1 = \lambda_2 = 1.5$ (system 14) and c) diameter $\sigma_2 = 2\sigma_1$, well depth $\varepsilon_2 = 0.5\varepsilon_1$ and range $\lambda_1 = \lambda_2 = 1.5$ (system 15). Hetero-SAFT-VR EOS results at T*= 2.0, 3.0, 4.0, 5.0 (from bottom to top) are represented as continuous curves and the squares represent the *NPT* MC simulation data.

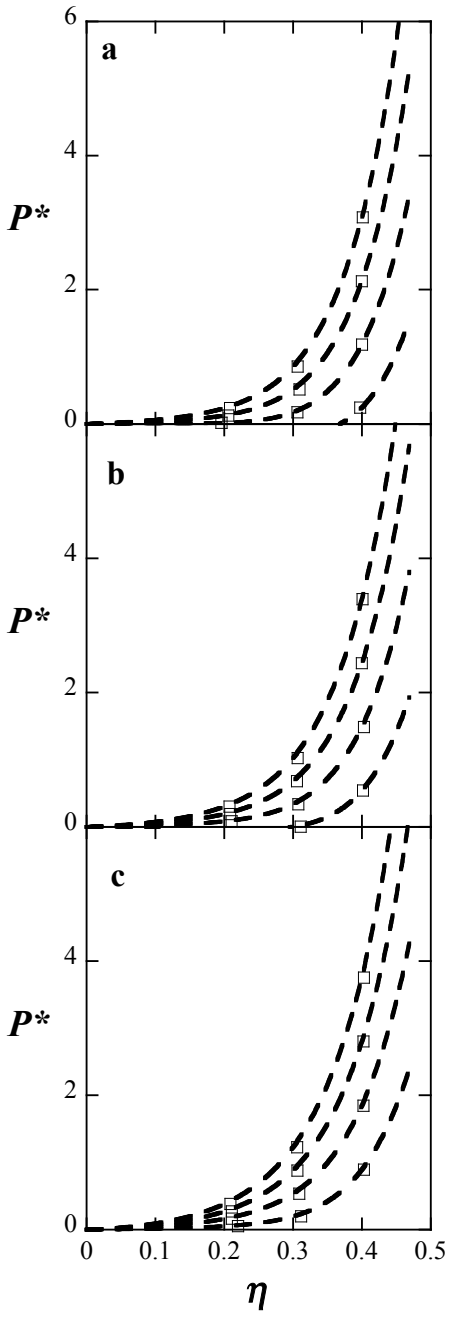

Figure 7: Isotherms for asymmetric diblock 8-mer fluids with $m_1 = 6$, $m_2 = 2$ and a) diameter $\sigma_2 = 2\sigma_1$, well depth $\varepsilon_2 = 1.5\varepsilon_1$ and range $\lambda_1 = \lambda_2 = 1.5$ (system 16), b) diameter $\sigma_2 = 2\sigma_1$, well depth $\varepsilon_2 = \varepsilon_1$ and range $\lambda_1 = \lambda_2 = 1.5$ (system 17) and c) diameter $\sigma_2 = 2\sigma_1$, well depth $\varepsilon_2 = 0.5\varepsilon_1$ and range $\lambda_1 = \lambda_2 = 1.5$ (system 18). Hetero-SAFT-VR EOS results at T*= 2.0, 3.0, 4.0, 5.0 (from bottom to top) are represented as continuous curves and the squares represent the *NPT* MC simulation data.

In order to obtain a comprehensive understanding of the thermodynamic properties of the systems studied and fully test the hetero-SAFT-VR approach, we have also determined phase diagrams for the symmetric 4-mer (systems 3 - 5, as shown in Figure 8) and 8-mer (systems 10 - 12, as shown in Figure 9) fluids with a segment diameter ratio of $\sigma_2 / \sigma_1 = 2$, a potential range of $\lambda_1 = \lambda_2 = 1.5$ and differing potential depth ratios of $\varepsilon_2 / \varepsilon_1 = 0.5$, 1.0, and 1.5. If we compare the phase diagrams for all of the symmetric 4-mer and 8-mer fluids studied, we can see that the critical temperature of the diblock chain fluids increases with an increase in the ratio of $\varepsilon_2 / \varepsilon_1$, which is to be anticipated as the attractive interactions between the molecules have increased. Additionally, as expected from the phase behavior of homonuclear fluids, as the chain length increases the critical point moves to higher temperatures and the phase envelope narrows. In all cases excellent agreement is achieved between the hetero-SAFT-VR predictions and the simulation data for both the gas and liquid coexisting densities, though we note the theory over-predicts the critical point. This shortcoming of the SAFT-VR approach has been addressed for homonuclear chains in recent work by the authors [36, 41, 42, 97], and will be extended to heteronuclear chains in future work.

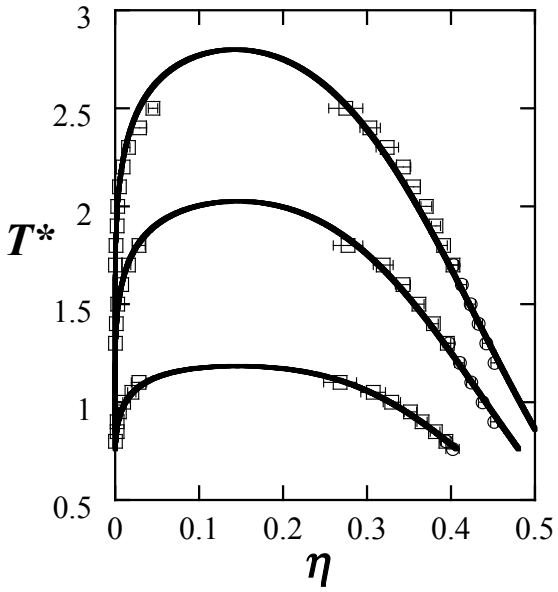

Figure 8: Phase equilibrium for symmetric diblock 4-mer fluids with (from top to bottom) diameter $\sigma_2 = 2\sigma_1$, well depth $\varepsilon_2 = 1.5\varepsilon_1$ and range $\lambda_1 = \lambda_2 = 1.5$ (system 3), diameter $\sigma_2 = 2\sigma_1$, well depth $\varepsilon_2 = \varepsilon_1$ and range $\lambda_1 = \lambda_2 = 1.5$ (system 4), and diameter $\sigma_2 = 2\sigma_1$, well depth $\varepsilon_2 = 0.5\varepsilon_1$ and range $\lambda_1 = \lambda_2 = 1.5$ (system 5). Hetero-SAFT-VR results are represented as continuous curves, and the squares and circles correspond to GEMC and *NPT* MC simulation data, respectively.

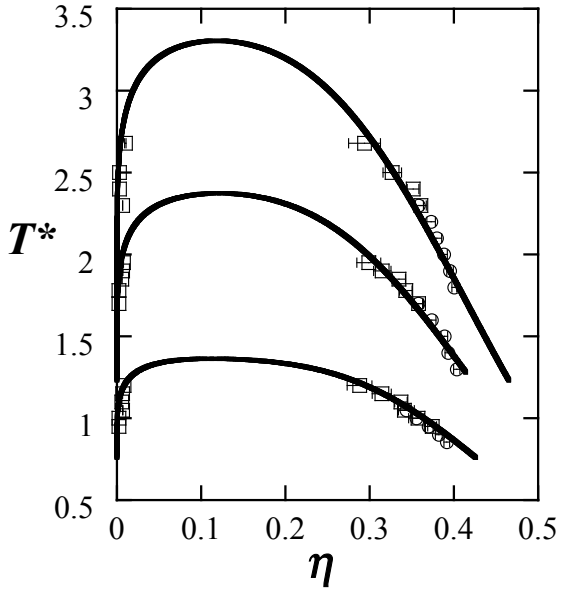

Figure 9: Phase equilibrium for symmetric diblock 8-mer fluids with (from top to bottom) diameter $\sigma_2 = 2\sigma_1$, well depth $\varepsilon_2 = 1.5\varepsilon_1$ and range $\lambda_1 = \lambda_2 = 1.5$ (system 10), diameter $\sigma_2 = 2\sigma_1$, well depth $\varepsilon_2 = \varepsilon_1$ and range $\lambda_1 = \lambda_2 = 1.5$ (system 11), and diameter $\sigma_2 = 2\sigma_1$, well depth $\varepsilon_2 = 0.5\varepsilon_1$ and range $\lambda_1 = \lambda_2 = 1.5$ (system 12). Hetero-SAFT-VR results are represented as continuous curves, and the squares and circles correspond to GEMC and *NPT* MC simulation data, respectively.

Finally, in order to gain a better understanding of the effect of molecular structure on coexistence properties we have considered the phase equilibrium of asymmetric 6-mer (systems 13 – 15, as shown in Figure 10) and asymmetric 8-mer fluids (systems 16 – 18, as shown in Figure 11) with three different potential depth ratios. In contrast to the symmetric diblock 8-mer fluid with $\varepsilon_2 / \varepsilon_1 = 1.5$ (system 10), the asymmetric 8-mer with $\varepsilon_2 / \varepsilon_1 = 1.5$ (system 16) has a lower critical temperature; however, the asymmetric diblock 8-mer fluid with $\varepsilon_2 / \varepsilon_1 = 0.5$ (system 18) has a higher critical temperature than the corresponding symmetric 8-mer fluid (system 12). It is also observed that the coexistence curve for the asymmetric 8-mer fluid with $\varepsilon_2 = \varepsilon_1$ (system 17) crosses that of

the asymmetric 8-mer fluid with $\varepsilon_2 = \varepsilon_1$ (system 11). For the systems with the same value of $\varepsilon_2 / \varepsilon_1$, the asymmetric 6-mer fluids have a higher critical point than the symmetric 4-mer fluids and a lower critical point than the asymmetric 8-mer fluids due to chain length effects. From the figures we see that the hetero-SAFT-VR prediction agrees well with the simulation results for the asymmetric fluids, indicating that the theory is able to capture the effect of having chains of different molecular structure, but equal chain length, on the phase behavior.

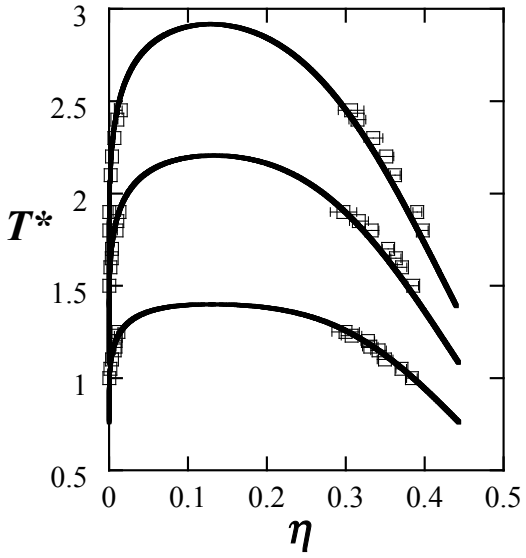

Figure 10: Phase equilibrium for asymmetric diblock 6-mer fluids with (from top to bottom) $m_1 = 4$, $m_2 = 2$ and diameter $\sigma_2 = 2\sigma_1$, well depth $\varepsilon_2 = 1.5\varepsilon_1$ and range $\lambda_1 = \lambda_2 = 1.5$ (system 13), diameter $\sigma_2 = 2\sigma_1$, well depth $\varepsilon_2 = \varepsilon_1$ and range $\lambda_1 = \lambda_2 = 1.5$ (system 14), and diameter $\sigma_2 = 2\sigma_1$, well depth $\varepsilon_2 = 0.5\varepsilon_1$ and range $\lambda_1 = \lambda_2 = 1.5$ (system 15). Hetero-SAFT-VR results are represented as continuous curves and the squares correspond to the GEMC simulation data.

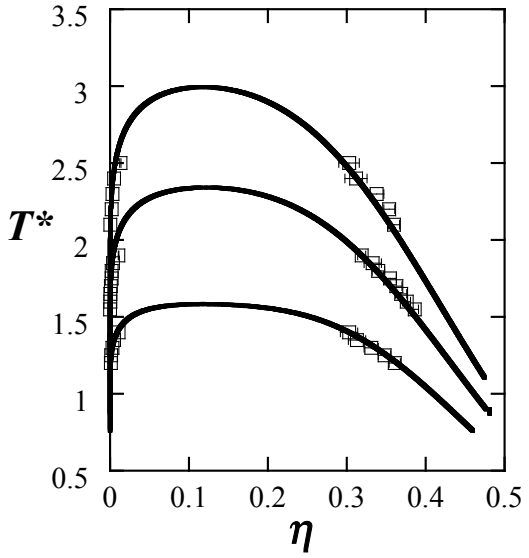

Figure 11: Phase equilibrium for asymmetric diblock 8-mer fluids with (from top to bottom) $m_1 = 6$, $m_2 = 2$ and diameter $\sigma_2 = 2\sigma_1$, well depth $\varepsilon_2 = 1.5\varepsilon_1$ and range $\lambda_1 = \lambda_2 = 1.5$ (system 16), diameter $\sigma_2 = 2\sigma_1$, well depth $\varepsilon_2 = \varepsilon_1$ and range $\lambda_1 = \lambda_2 = 1.5$ (system 17), and diameter $\sigma_2 = 2\sigma_1$, well depth $\varepsilon_2 = 0.5\varepsilon_1$ and range $\lambda_1 = \lambda_2 = 1.5$ (system 18). Hetero-SAFT-VR results are represented as continuous curves and the squares correspond to the GEMC simulation data.

3.5 Conclusions

In this work, the SAFT-VR approach has been developed to study hetero-segmented chain fluids, with particular focus on symmetric and asymmetric diblock chains. Eighteen systems differing in chain length, segment size, potential range, potential well depth, and molecular structure have been examined. In order to gain a comprehensive understanding of the thermodynamic properties of the systems studied and test the hetero-SAFT-VR approach, both *NPT* MC and GEMC simulation methods were utilized to validate the theoretical predictions. The phase behavior of the diblock fluids is found to be affected by the interaction energies, segment size and the distribution of segments in terms of symmetry, i.e. at a given pressure and temperature, the fluid density rises as the ratio of interaction energy and/or segment size increases, as the potential range increases,

as the chain length increases, and as the fraction of smaller segments decreases. The critical temperature of the diblock chain fluids rises as the ratio of $\varepsilon_2 / \varepsilon_1$ increases, and as the chain length increases. Excellent agreement between the theoretical predictions and simulation results has been achieved. The average absolute deviation (AAD) between the hetero-SAFT-VR predictions and the simulation data for all systems is 1 - 3%. Slightly larger deviations (4 - 10%) are seen at low pressures and for the lowest temperature (T* = 2) studied. In the following chapters, we will apply the hetero-SAFT-VR approach to study real fluids such as small molecules and polymers composed of different functional groups.

Chapter IV

APPLICATION OF THE HETERO-SAFT-VR EOS TO POLYHEDRAL OLIGOMERIC SILSESQUIOXANES

4.1 Introduction

Polyhedral oligomeric silsesquioxane (POSS) molecules are unique nanometer-size inorganic/organic hybrid structures based on a $(SiO_{1.5})_8$ core. POSS can be functionalized with the same organic or inorganic group on each corner of the cube ($R_8Si_8O_{12}$) or with one group on one corner and a different group on the others ($RR'_7Si_8O_{12}$), the simplest POSS monomer being hydrogen terminated POSS ($H_8Si_8O_{12}$). The ability to synthesize POSS cubes with different functional groups results in a large number of possible POSS-based molecules whose physical properties can be tailored through manipulation of the functional groups, opening up many possible application areas for POSS-based materials [98].

POSS molecules can either be physically blended with polymers to form nanocomposite materials or chemically grafted to polymeric chains, where they form a crosslinked polymer network or serve as pendant groups from the polymer backbone. The incorporation of POSS molecules into polymeric materials often results in dramatic improvements in the material properties such as oxidation resistance, surface hardening, improved mechanical and thermal properties and reductions in flammability and heat evolution [99]. The properties of POSS-polymer blends depend on the interactions between the POSS molecules and the polymer. For example, cyclohexyl- and isobutyl-

POSS fillers, when well dispersed into polymethyl methacrylate (PMMA), decrease the zero-shear viscosity. However, once the solubility limit of the POSS molecules is reached, the POSS aggregates into crystallites and leads to an increase in the viscosity [100]. In the same study, blends of POSS-PMMA copolymer with isobutyl-POSS were observed to show a dramatic increase in viscosity with the addition of even small amounts of POSS fillers due to the interactions between the free POSS and POSS pendants [100].

In recent years research on POSS-based systems, particularly synthesis and structural properties, has increased significantly. Information on the thermodynamic properties, however, is more scarce. The melting points of 8-fold alkyl substituted POSS have been studied and show a sharp decrease from octa-propyl-POSS to octa-pentyl-POSS, while molecules with longer alkyl chains (C_5 - C_{10}) show an odd-even effect [101] similar to that observed for other homologous series [102]. From a theoretical point of view it is interesting to study both octa- and mono-substituted POSS systems with simple tether groups like the alkanes, as this allows a systematic study of the effect of the tether on the thermodynamic properties. Although such systems might be considered model compounds for silsesquioxane-based materials, they do show potentially interesting properties, including their use as amphiphiles for novel core/shell type silicate nanoparticles [103].

In order to obtain a better understanding of POSS systems at a molecular level, several simulation studies have recently appeared [104-112]. For example, using a minimal model to mimic POSS systems, Lamm and co-workers [105] studied the structural properties of cross-linked POSS networks using lattice Monte Carlo

simulations. The effect of the length of the linkers between POSS cages on network structural properties was examined and the porosity was seen to decrease with increasing tether length in qualitative agreement with experimental data. In work closer to the current study, a number of atomistic molecular dynamics simulations have been performed on POSS-solvent and POSS-polymer systems [104, 107-110]. In particular, Striolo and co-workers [108, 109, 111, 113] have studied dilute solutions of hydrogen terminated and octa-substituted POSS monomers in poly(dimethylsiloxane), n-hexadecane and n-hexane to probe the POSS-solvent interactions. This work illustrated that it is possible to modulate the effective POSS-POSS interaction by increasing the temperature, solvent and/or functional groups on the POSS cage.

Although molecular simulation is a useful tool with which to study atomic and nano-scale processes, a theoretical approach can much more rapidly study a wide range of systems than is possible by simulation. There are many theoretical approaches available to describe the thermodynamics and physical properties of fluid systems. However, in contrast to traditional equations such as activity coefficient models and cubic equations of state (EOS), molecular-based approaches provide the opportunity to develop a molecular level basis for the observed behavior and a more predictive approach. In particular, the molecular-based SAFT approach [114, 115] provides a framework in which the effects of molecular shape and interactions on the thermodynamic properties can be separated and quantified. The explicit description of the molecular level interactions enables the parameters of the resulting equation of state to have physical meaning, leading to more predictive capabilities and a limited reliance on fitting to experimental data. While there are several versions of the SAFT equation

available [116, 117], we focus on the SAFT-VR [4, 5] equation in which monomers interact through a potential of variable attractive range (VR). In this work, we apply the hetero-SAFT-VR approach developed by McCabe and co-workers [8, 64] to study the effect of tether groups on the thermodynamic properties of both mono-tethered and homogeneously multi-tethered POSS molecules. The theoretical model for POSS is described in section 4.2 and details of the molecular dynamics simulations performed to parameterize and validate the theoretical model are given in section 4.3. The theoretical results are presented and compared with molecular simulations in section 4.4 and conclusions drawn in section 4.5.

4.2 Hetero-SAFT-VR Model for POSS

The hetero-SAFT-VR approach allows molecules to be described as chains of segments that can have different size and/or energy parameters. In the previous chapter, we have validated the hetero-SAFT-VR approach using isothermal-isobaric (*NPT*) and Gibbs ensemble Monte Carlo (GEMC) simulation data and demonstrated that the theory can accurately capture the effects of interaction energy, segment size and molecular structure on the *PVT* and phase behavior of heteronuclear diblock fluids [8]. In the same spirit, the hetero-SAFT-VR approach allows us to model alkyl-tethered POSS molecules as a single spherical POSS core connected to a number of smaller segments that describe the alkyl tethers as shown in Figure 12(b).

We use the equations of the hetero-SAFT-VR for pure fluids given in section 2.1 to study POSS molecules. The equation (2.22) of chain term for POSS fluids in hetero-SAFT-VR becomes

$$\frac{A^{chain}}{NkT} = -N_t\left[\ln y_{12}^{SW}\left(\sigma_{12}\right) + \left(m_2 - 1\right)\ln y_{22}^{SW}\left(\sigma_{22}\right)\right] \tag{4.1}$$

where N_t is the number of tethers per molecule and m_2 is the number of alkyl segments per tether.

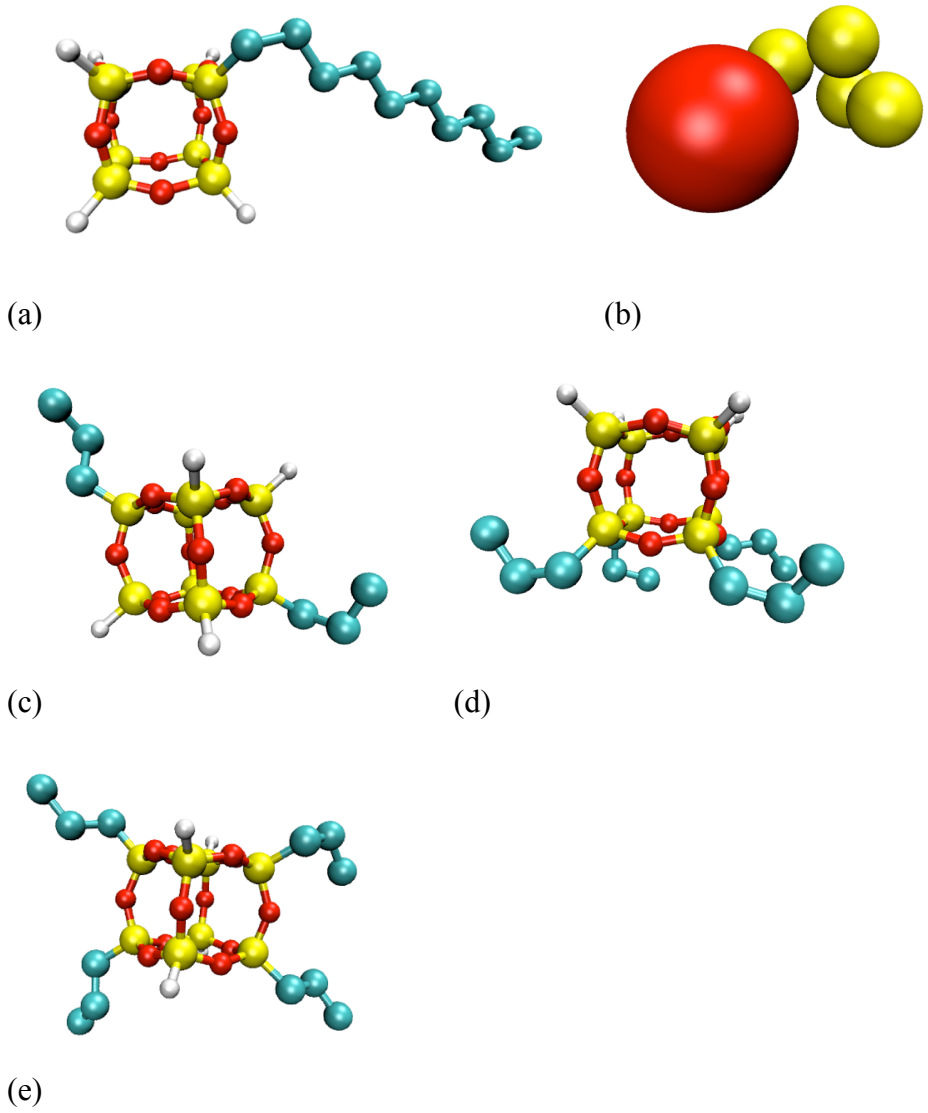

Figure 12: Schematic illustration of (a) mono-tethered decyl-POSS (b) the hetero-SAFT-VR model for mono-tethered decyl-POSS, (c) di-tethered propyl-POSS, and (d) and (e) the two different tetra-tethered propyl-POSS molecules studied.

4.3 Simulation Details

In order to study POSS molecules with the hetero-SAFT-VR approach the theoretical model parameters (i.e. m, σ, ε, λ) for the POSS cube must be determined. Typically the SAFT parameters are obtained by fitting to experimental thermodynamic property data. However, the dearth of experimental data on the thermodynamics of POSS-based molecules makes it very difficult to calibrate the hetero-SAFT-VR model by comparison to experiment. Hence, here we calibrate the theory using simulation data based on reliable force fields. This can be thought of as a coarse-graining of the atomistic simulation, albeit into a coarse-grained theoretical model, as opposed to the usual coarse-grained force field model. Molecular dynamics simulations were performed for 7 different mono- and multi-tethered POSS fluids: mono-tethered propyl-, hexyl- and, nonyl- POSS; di-tethered propyl-POSS, tetra-tethered propyl-POSS with two different arrangements of the tethers on the POSS cube, and octa-tethered propyl-POSS (as shown in Figure 12).

The molecular dynamics simulations were carried out using the DL_POLY 2 simulation software [118] with atomistic force fields for the POSS and tether molecules as described below. Simulations were performed in the canonical (*NVT*) ensemble using the Berendsen thermostat [86] to maintain the temperature. In each simulation 64 POSS molecules (ranging from 1920 atoms to 2816 atoms) were used and the usual periodic boundary conditions were applied to the simulation box. Initially simulations were also performed with 128 POSS molecules; however, no difference was observed in the calculated density and so 64 molecules were used for all production runs. A time step of 1 fs was employed and a cutoff of 10 Å used for non-bonded interactions. Each

simulation was started from a lattice configuration and then equilibrated for 100 ps, followed by production runs of 400 - 500 ps during which the properties of interest were calculated. For each system three isotherms were studied (700 K, 900 K and 1200 K) and the pressure profile obtained for a series of densities between η = 0.1 - 0.45. The temperatures were chosen to ensure the POSS systems were above the experimental and force field melting points [119]. While POSS monomers probably decompose at 1000 K [120], the high temperature results correspond to hypothetical results that would be obtained in the absence of decomposition. From the point of view of determining effective parameters for use in a hetero-SAFT-VR model, the absence of decomposition in either the simulation or the hetero-SAFT-VR models is not a drawback; our goal here is to calibrate the molecular model using simulation data. A similar problem existed in the calibration of alkane force fields against experimental phase equilibrium and critical point data [121], as such models also do not include decomposition.

The Hybrid-COMPASS (HC) force field [122, 123] was used to describe the POSS molecules. The HC force field was shown in earlier work to be successful in describing the structural properties of POSS systems [119]. The TraPPE united atom model [124], which was specifically developed to study the fluid phase behavior of alkanes, was used to describe the alkyl tethers. *Ab-initio* calculations of alkyl-tethered POSS systems [125] have shown that the POSS cage is not significantly influenced by the tether and vice versa, indicating that it is possible to combine force fields developed independently to study functionalized POSS systems and take advantage of specifically developed force fields for the tethered groups. Below we briefly describe the force fields used.

4.3.1 Force Field for the POSS Cube

As in earlier work [119] the simplified or hybrid COMPASS force field was used to model the POSS cube. In this model bond stretching U_b, bond angle-bending U_θ and torsional motion U_ϕ are respectively described by:

$$U_b = k_2\left(b - b_0\right)^2 + k_3\left(b - b_0\right)^3 + k_4\left(b - b_0\right)^4 \tag{4.2}$$

$$U_\theta = H_2\left(\theta - \theta_0\right)^2 + H_3\left(\theta - \theta_0\right)^3 + H_4\left(\theta - \theta_0\right)^4 \tag{4.3}$$

$$U_\Phi = V_1\left(1 - \cos\left(\Phi\right)\right) + V_2\left(1 - \cos\left(2\Phi\right)\right) + V_3\left(1 - \cos\left(3\Phi\right)\right) \tag{4.4}$$

where b, θ, and Φ are the bond length, bond angle, and dihedral angle respectively, b_0 the equilibrium bond length, θ_0 the equilibrium bond angle and k_2, k_3, k_4, H_2, H_3, H_4, and V_1, V_2, V_3 constants.

Nonbonded interactions are described by a Lennard-Jones 9-6 function.

$$U_{vdw} = \varepsilon_{ij}\left[2\left(\frac{\sigma_{ij}}{r}\right)^9 - 3\left(\frac{\sigma_{ij}}{r}\right)^6\right] \tag{4.5}$$

The cross interaction parameters σ_{ij} and ε_{ij} are calculated using a 6th order combining rule:

$$\sigma_{ij} = \left(\frac{\sigma_i^6 + \sigma_j^6}{2}\right)^{1/6} \tag{4.6}$$

$$\varepsilon_{ij} = \left(\frac{2\sigma_i^3\sigma_j^3\sqrt{\varepsilon_i\varepsilon_j}}{\sigma_i^6 + \sigma_j^6}\right) \tag{4.7}$$

where σ_i, σ_j, ε_i, ε_j are the interaction parameters for the like atoms. Details of the potential model parameters used for the hybrid-COMPASS force field [122, 123] are reported in Table 8.

Table 8: Parameters used in the hybrid-COMPASS force field for the POSS systems studied.

Bond	b_0 **(Å)**	k_2 **(kcal/mol Å^2)**	k_3 **(kcal/mol Å^3)**	k_4 **(kcal/mol Å^4)**
Si-O	1.640	350.1232	-517.3424	673.7067
Si-H	1.478	202.7800	-305.3600	280.2700
Si-C	1.899	189.6500	-279.4200	307.5100
Angle	θ_0 **(deg)**	H_2 **(kcal/mol rad^2)**	H_3 **(kcal/mol rad^3)**	H_4 **(kcal/mol rad^4)**
Si-O-Si	159.0	8.5000	-13.4188	-4.1785
O-Si-O	110.7	70.3069	-6.9375	0.0000
H-Si-O	107.4	57.6643	-10.6506	4.6274
C-Si-O	114.9	23.0218	-31.3993	24.9814
Dihedral		V_1 **(kcal/mol)**	V_2 **(kcal/mol)**	V_3 **(kcal/mol)**
Si-O-Si-O		-0.225	0.000	-0.010
Si-O-Si-H		0.000	0.000	-0.010
Si-O-Si-C		0.000	0.000	-0.010
Non-bonded interactions		σ_{ij} **(Å)**		ε_{ij} **(kcal/mol)**
Si-Si		4.4050		0.19800
Si-Si(C)		4.3494		0.16054
Si-O		4.0323		0.08993
Si-C		4.1744		0.09063
Si(C)-Si(C)		4.2900		0.13100
Si(C)-O		3.9437		0.07710
Si(C)-C		4.1007		0.08560
O-O		3.3000		0.08000
O-C		3.6290		0.06342

4.3.2 Force Field for Alkyl Tethers

The alkyl tethers are described using the TraPPE united-atom force field [124] for alkanes in which each carbon atom and its bonded hydrogen atoms are treated as a single

spherical interaction site. Bond-stretching U_b and bond-angle-bending U_θ terms are described by simple harmonic functions:

$$U_b = \frac{1}{2} k_{ij} \left(r - r_{ij} \right)^2 \tag{4.8}$$

$$U_\theta = \frac{1}{2} k_\theta \left(\theta - \theta_0 \right)^2 \tag{4.9}$$

where k_{ij} and k_θ are the force constants, r_{ij} is the equilibrium bond length between atoms i and j and θ_0 is the equilibrium angle. The torsion potential is expressed as a cosine function,

$$U_\Phi = c_1 \left[1 + \cos\left(\Phi \right) \right] + c_2 \left[1 - \cos\left(2\Phi \right) \right] + c_3 \left[1 + \cos\left(3\Phi \right) \right] \tag{4.10}$$

where c_1, c_2, c_3 are constants and Φ is the torsional angle. In the TraPPE potential the non-bonded van der Waals interactions are described via a Lennard-Jones 12-6 potential and the cross alkyl-alkyl interactions (i.e. ε_{ij} and σ_{ij}) are calculated using the Lorenz-Berthelot combining rules. The parameters used to study the alkyl tether groups in this work are reported in Table 9. In studying alkyl-POSS molecules a number of interactions between the HC and TraPPE force fields must be defined. As in previous work [119], the bond-stretching interactions for Si-CH_3 and Si-CH_2 are approximated by those for Si-C, the angle-bending interactions of O-Si-CH_3 and O-Si-CH_2, are given by O-Si-C, and the torsional interactions for O-Si-CH_2-CH_2 and Si-O-Si-CH_2 are given by X-Si-C-X and Si-O-Si-C respectively, all from the HC force field. Angle interactions for Si-CH_2-CH_2 and Si-CH_2-CH_3 are approximated by the C-C-C potential in the TraPPE force field, and the torsional interactions for the Si-CH_2-CH_2-CH_2 and Si-CH_2-CH_2-CH_3 bonds are described by the C-C-C-C potential in the TraPPE force field. The parameters for the cross

nonbonded interactions between atoms in the HC and TraPPE force fields are determined following the work of Frischknecht and Curro [126] and are listed in Table 10.

Table 9: Parameters used in the TraPPE force field [124] for the alkyl tethers of the POSS systems studied.

Bond		r_{ij} **(Å)**	k_{ij} **(kcal/mol Å^2)**
C-C		1.540	889.9
Angle		θ_0 **(deg)**	k_θ **(kcal/mol rad^2)**
C-C-C		114.0	124.3122
Dihedral	c_1 **(kcal/mol)**	c_2 **(kcal/mol)**	c_3 **(kcal/mol)**
C-C-C-C	1.4123	-0.27126	3.14786
Non-bonded interactions		σ_{ij} **(Å)**	ε_{ij} **(kcal/mol)**
CH_3-CH_3		3.7500	0.194921
CH_3-CH_2		3.8500	0.133544
CH_2-CH_2		3.9500	0.091493

Table 10: Parameters for the cross nonbonded interactions between atoms in the hybrid-COMPASS and TraPPE force fields.

Non-bonded interactions	σ_{ij} **(Å)**	ε_{ij} **(kcal/mol)**
Si-CH_3	3.830	0.15960
Si-CH_2	3.886	0.10947
O-CH_3	3.380	0.12470
O-CH_2	3.445	0.08550

4.4 Results

The parameters for POSS in the hetero-SAFT-VR approach were fitted to molecular dynamics simulation data for mono-tethered propyl-POSS at 700 K and 1200K. The parameters for the alky tethers were taken from earlier work on parameter estimation for the alkanes. In an extensive study of the phase behavior of *n*-alkanes and their mixtures with the SAFT-VR approach, McCabe and co-workers determined linear relations for the

SAFT-VR parameters for the alkane homologous series [127]. These provide simple expressions for the model parameters as a function of molecular weight M_W, *viz.*

$$m\lambda = 0.039M_W + 0.873 \tag{4.11}$$

$$m\sigma^3 = 1.566M_W + 24.02 \tag{4.12}$$

$$m(\varepsilon/k) = 6.343M_W + 76.38 \tag{4.13}$$

The number of segments m in the alkyl chain is determined from the simple relation $m = 1/3(c-1)+1$, as in earlier work [128]. Therefore in this work only the POSS parameters are optimized. The mono-tethered propyl-POSS system was chosen to determine the POSS parameters rather than hydrogen terminated POSS in order to take into account the effect of the cross-interactions between the POSS and alkyl tether, which are expected to be non-ideal, in an effective way. The parameters obtained from fitting to the PVT data at 700 K and 1200 K for the POSS cube are σ = 6.949 Å, ε / k = 815.5 K, and λ = 1.8 and a comparison between the theoretical predictions and simulation data for mono-tethered propyl POSS is shown in Figure 13. We note that, particularly at low temperatures, some of the pressures reported are negative which clearly reflects a metastable state.

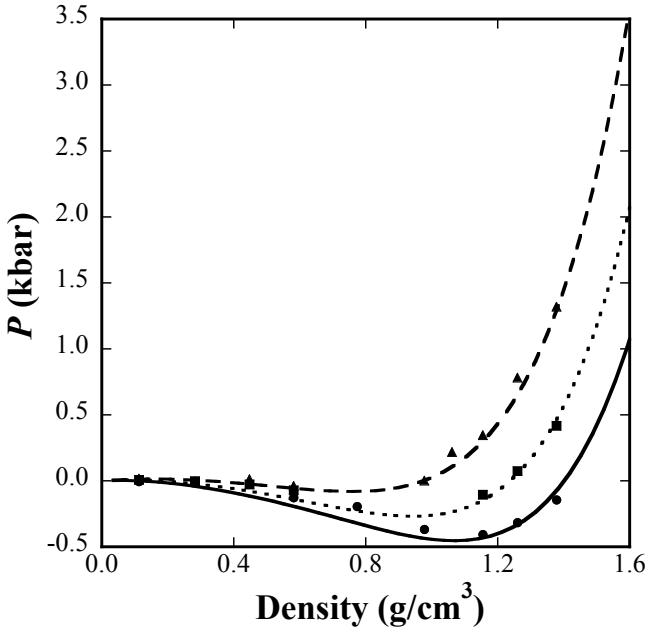

Figure 13: Isotherms for mono-substituted propyl-POSS at 700 K (solid line), 900 K (dotted line), and 1200 K (dashed line). The circles, squares, and triangles represent molecular dynamics simulation results at 700 K, 900 K, and 1200 K respectively.

Once the parameters for the POSS cube were determined, other POSS systems were studied to test parameter transferability. In Figure 14 we present the theoretical predictions for mono-tethered hexyl-POSS from the hetero-SAFT-VR approach using the POSS parameters determined from fitting to PVT data for propyl-POSS and alkyl parameters determined using equations (4.11)-(4.13). From the figure we can see that the theoretical predictions are in good agreement with the pseudo-experimental data, the deviation between the simulation and theoretical results being ~10% in the high density region. A similar result is obtained for mono-tethered nonyl-POSS (Figure 15), in that good agreement is achieved between the theoretical predictions and the pseudo-experimental data without additional optimization of the parameters. This transferability allows us to predict the behavior of other POSS systems with varying alkyl chain lengths as shown in Figure 16 where we consider isotherms at 900 K for tethers from C = 2 to C

= 10 respectively. We find that at a given temperature and pressure the liquid density decreases as the tether length increases. This is consistent with the conclusion drawn for the asymmetric diblock model fluids studied in previous work [8], where increasing the fraction of the smaller segments within a molecule resulted in lower densities at a given pressure and temperature.

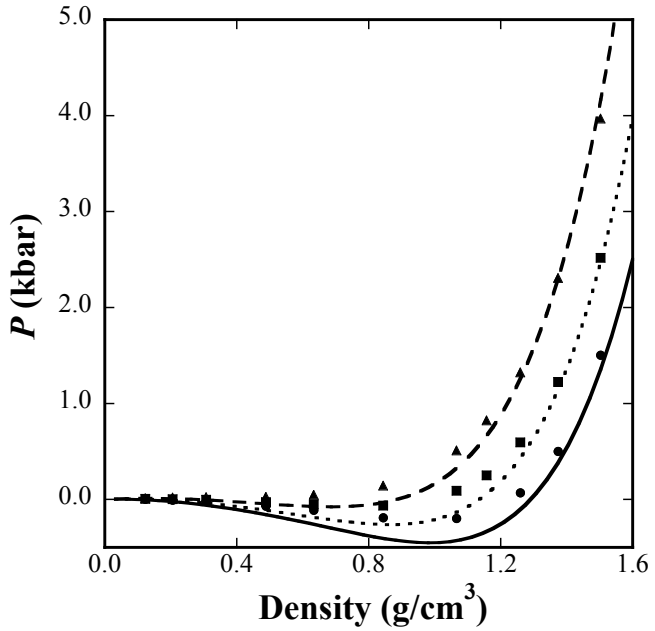

Figure 14: Isotherms for mono-substituted hexyl-POSS at 700 K (solid line), 900 K (dotted line), and 1200 K (dashed line). The circles, squares, and triangles represent molecular dynamics simulation results at 700 K, 900 K, and 1200 K respectively.

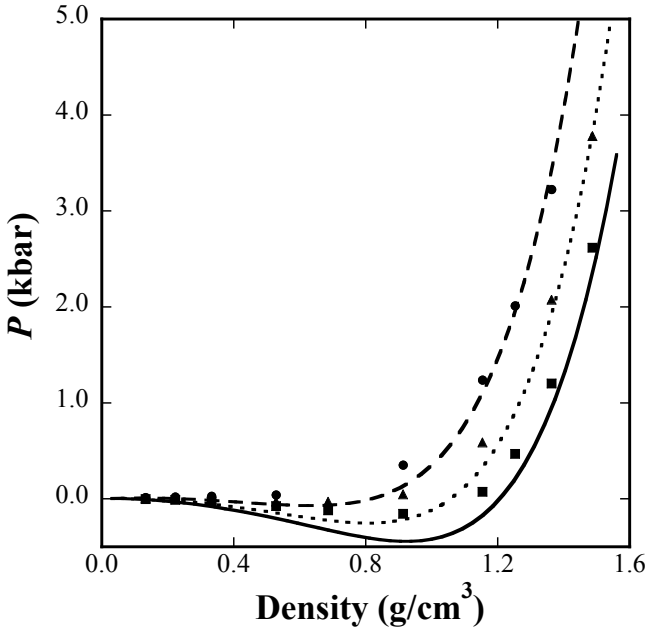

Figure 15: Isotherms for mono-substituted nonyl-POSS at 700 K (solid line), 900 K (dotted line), and 1200 K (dashed line). The circles, squares, and triangles represent molecular dynamics simulation results at 700 K, 900 K, and 1200 K respectively.

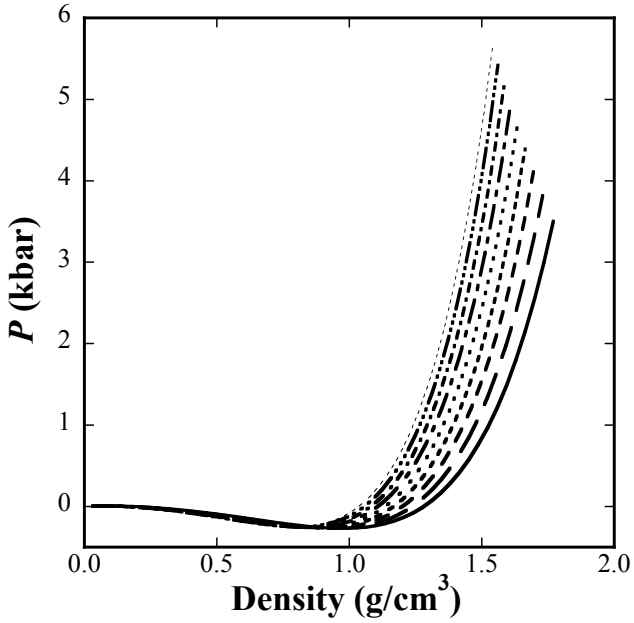

Figure 16: Prediction of isotherms for mono-tethered alkyl-POSS at 900 K. The lines correspond (from right to left) to ethyl (solid line), propyl, butyl, hexyl, heptyl, octyl, nonyl and decyl tethers.

We have also studied the effect of the number of tethers on the thermodynamic properties of multi-tethered POSS systems. Figure 17 presents theoretical predictions for isotherms at 700 K, 900 K, 1200 K for di-tethered propyl-POSS. From the figure we note that while there is good agreement between the theoretical predictions and simulation data at 1200K, deviations are observed at low pressures for the other temperatures studied. We have also calculated isotherms for tetra-tethered propyl-POSS with two different arrangements of the tethers on the POSS cube; tetra-tethered propyl-POSS with the tethers on one face of the cube (Figure 12d) and tetra-tethered propyl-POSS with the tethers on opposite corners of the cube (Figure 12e). We find from the simulation results (as shown in Figure 18) that the differences between the two systems are very small, and therefore a comparison with the hetero-SAFT-VR predictions, which cannot distinguish between the different arrangements of the tethers on the POSS cube, is reasonable. However, we find that while the agreement between the theory and simulation is good at low denstities, the density is underpredicted at a given temperature and pressure for higher densities (> 0.8 g/cm^3). Finally results for octa-tethered propyl-POSS are presented in Figure 19. From Figure 17, Figure 18, and Figure 19 we can see that the deviation between the theoretical prediction and the simulation data increases as the number of tethers increases. This deviation may be caused by the fact that the tethers on the POSS cage in the hetero-SAFT-VR approach are fully flexible and their arrangement cannot be specified as in the MD simulations, and so perhaps steric effects are not accurately captured.

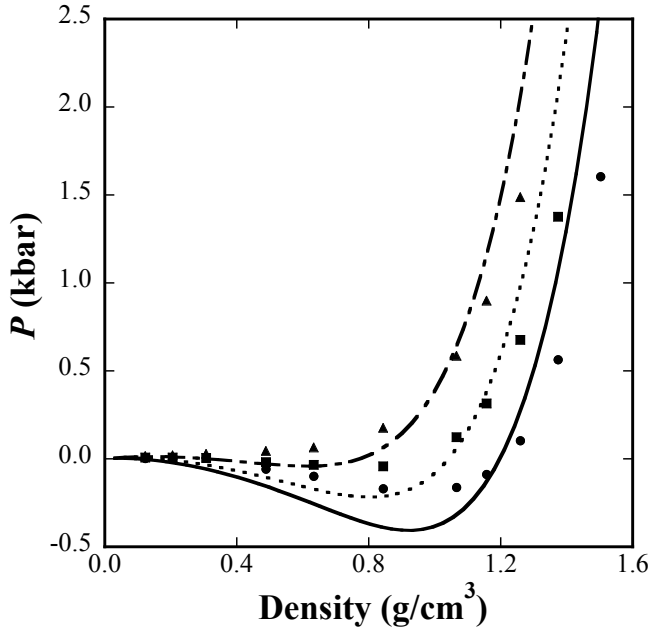

Figure 17: Isotherms for di-tethered propyl-POSS at 700 K (solid line), 900 K (dotted line), and 1200 K (dashed line). The circles, squares, and triangles represent molecular dynamics simulation results at 700 K, 900 K, and 1200 K respectively.

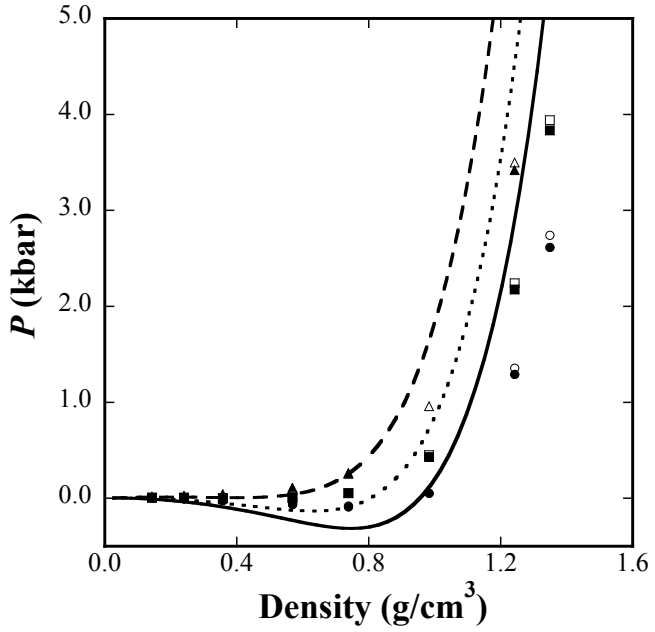

Figure 18: Isotherms for tetra-tethered propyl-POSS at 700 K (solid line), 900 K (dotted line), and 1200 K (dashed line). The circles, squares, and triangles represent molecular dynamics simulation results at 700 K, 900 K, and 1200 K, respectively. Empty symbols are for the configuration in Figure 12d and solid for the configuration Figure 12e.

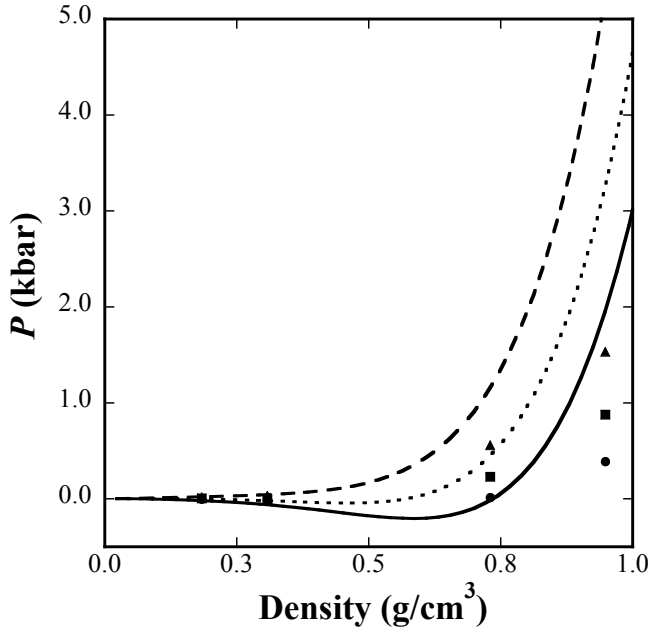

Figure 19: Isotherms for octa-tethered propyl-POSS at 700 K (solid line), 900 K (dotted line), and 1200 K (dashed line). The circles, squares, and triangles represent molecular dynamics simulation results at 700 K, 900 K, and 1200 K respectively.

In order to gain some insight into the effect of the number of tethers on the thermodynamic properties, isotherms at 900 K for a series of multi-propyl-substituted POSS systems with the number of tethers varying from 2 to 8 were calculated and the results are presented in Figure 20. We find that as the number of tethers increases the density decreases at a given temperature and pressure, which is in agreement with the MD simulation results for tetra-substituted POSS compared to octa-substituted POSS.

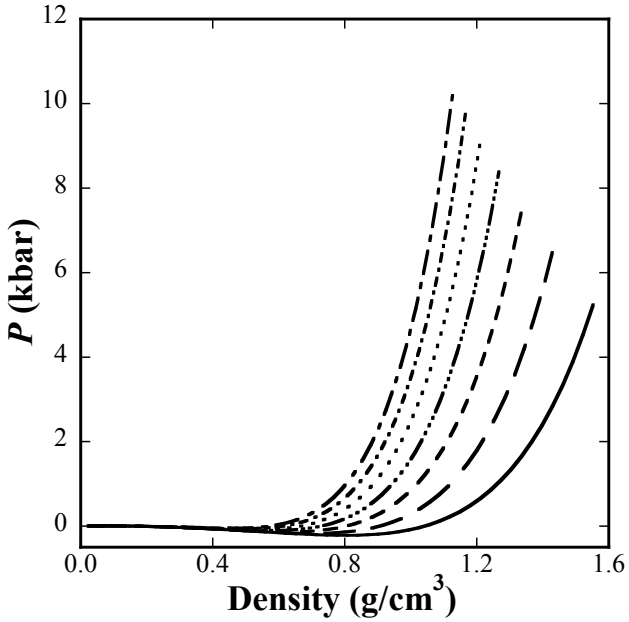

Figure 20: Prediction of isotherms for multi-tethered propyl-POSS at 900 K. The lines correspond to POSS cubes with 2 (solid line), 3, 4, 5, 6, and 8 tethers (from right to left).

We have also studied the vapor-liquid equilibrium (VLE) of a series of mono-substituted alkyl-POSS systems, the results of which are presented in Figure 21. From the calculations we find that the critical temperature decreases as the length of the tether increases, which is consistent with the tethers disrupting the packing and interaction of the POSS cubes.

Since the POSS parameters used in this work were determined by fitting to limited pseudo-experimental data we have also studied a number of model fluids in order to obtain a better understanding of the effect of the parameters on the observed properties and trends. Each model fluid studied mimics a mono-tethered POSS system in that it is composed of two types of segments that have different size and energy parameters, with the number of smaller segments ranging from 1 to 10. The systems studied are listed in Table 11 along with the observed trend in the critical temperature as the tether length is

increased from 1 to 10. We find that generally the critical temperature decreases as the number of tether segments increases. Therefore, we expect the predictions from the hetero-SAFT-VR approach for mono-tethered alkyl-POSS to be at least qualitatively accurate.

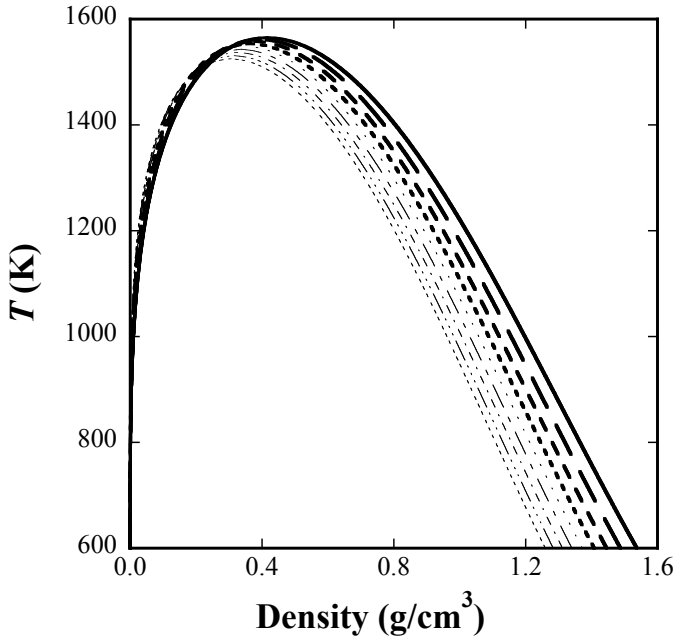

Figure 21: Prediction of vapor-liquid equilibrium curves for mono-tethered alkyl-POSS. The lines correspond to POSS cubes with ethyl (solid line), propyl, butyl, hexyl, heptyl, octyl, nonyl and decyl tethers (from right to left).

Table 11: Model fluid systems studied and predicted trends in T_c as a function of tether length.

System	m_1	m_2	σ_2/σ_1	$\varepsilon_2/\varepsilon_1$	λ_1	λ_2	T_c
1	$1 \rightarrow 10$	1	1.6	3	1.5	1.5	$\downarrow$
2	$1 \rightarrow 10$	1	1.6	3	1.5	1.8	$\downarrow$
3	$1 \rightarrow 10$	1	1.8	3	1.5	1.8	$\downarrow$
4	$1 \rightarrow 10$	1	1.8	3	1.8	1.8	$\uparrow\downarrow$
5	$1 \rightarrow 10$	1	1.8	4	1.5	1.8	$\downarrow$
6	$1 \rightarrow 10$	1	1.8	4	1.8	1.8	$\downarrow$
7	$1 \rightarrow 10$	1	2	3	1.5	1.8	$\downarrow$
8	$1 \rightarrow 10$	1	2	3	1.8	1.8	$\uparrow\downarrow$

Finally, the VLE curves for a series of octa-substituted alkyl-POSS systems of varying tether length have also been studied and are presented in Figure 22. For octa-tethered POSS we find that the VLE curves intersect at a density of ~0.5 g/cc and the predicted critical points increase with increasing tether length. Experimentally, the critical points of the *n*-alkanes also increases with carbon number. Furthermore it is well known that while the melting points of the alkanes increases with carbon number, the relatively short chains show an odd-n/even-n behavior is observed (the alternation becomes attenuated with increasing carbon number and is not detectable for n > 16) [129] and a plot of critical temperature versus melting point indicates a strong correlation or cooperative phenomena between the two properties [102]. The melting points of octa-substituted alkyl-POSS first decreases from C_3 to C_5 and then increases slowly from C_5 to C_{10}, with octa-tethered propyl-POSS having the highest melting point of the systems studied and an odd-even effect being observed for $C_5 - C_{10}$, which was the longest alkyl chain tether studied [101]. The decrease in melting point from C_3 to C_5 is presumably due to the dominant effect of the POSS cube, which diminishes as the chain length of the

alkyl tether increases. The predicted critical points for octa-substituted alkyl-POSS when plotted against their experimental melting points as in Figure 23 appear to follow a similar linear trend and could enable the melting points of octa-substituted alkyl-POSS molecules with longer tether lengths to be determined from the hetero-SAFT-VR predictions for the critical temperature.

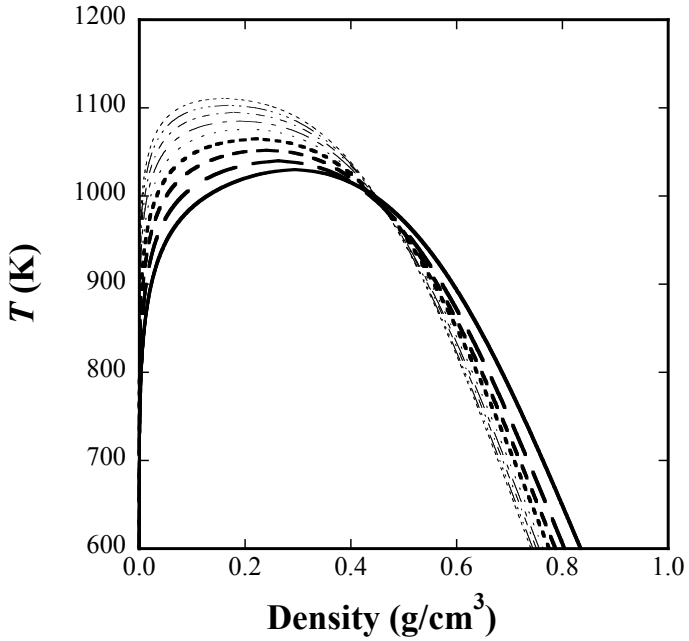

Figure 22: Prediction of isotherms for mono-tethered alkyl-POSS at 900 K. The lines correspond (from right to left) to POSS cubes with ethyl (solid line), propyl, butyl, hexyl, heptyl, octyl, nonyl and decyl tethers.

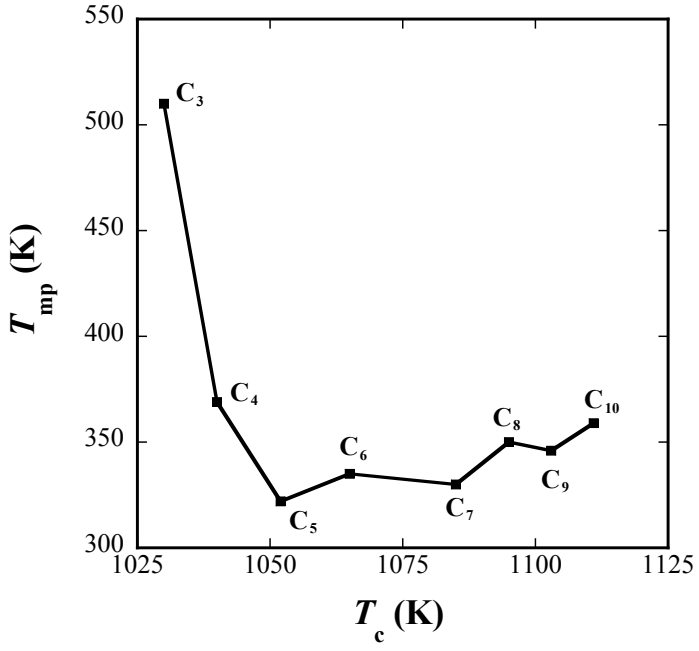

Figure 23: Experimental melting points versus critical temperature for octa-substituted alkyl-POSS of increasing chain length from C_3 – C_{10} predicted from the hetero-SAFT-VR EOS.

4.5 Conclusions

The hetero-SAFT-VR approach has been applied to study alkyl-substituted POSS fluids. Atomistic molecular dynamics simulations were performed for three mono-tethered POSS systems and four multi-tethered POSS systems, and in general good agreement obtained between the theoretical predictions and the simulation data. We find that as the length of the alkyl tether increases, the liquid density of mono-substituted POSS systems decreases at a given temperature and pressure. Additionally, for multi-substituted POSS systems, the density was seen to decrease as the number of tethers increased at a given temperature and pressure. For the tetra- and octa-substituted POSS systems studied, deviations were observed between the simulation data and theoretical predictions, which could be due to steric effects that are not captured by the hetero-SAFT-VR approach due

to the fully flexible nature of the molecules depicted by the model. However, we note that the results for the multi-tethered POSS systems can be considered reasonable since the hetero-SAFT-VR parameters for the POSS cube were obtained by fitting to PVT data for mono-tethered propyl-POSS and no binary interaction parameter between the POSS group and alkyl groups were used to take into account the dissimilarity of the POSS and alkyl segments. The phase behavior of the POSS systems studied was also investigated and the critical points predicted as a function of tether length and the number of tethers on the POSS cube. For mono-substituted alkyl-POSS, the critical temperature is predicted to decrease with increasing tether length from C_3 to C_{10}, while for octa-substituted alkyl-POSS systems the critical temperature increases as tether length increases from C_3 to C_{10}. Furthermore, experimental melting points versus predicted critical temperatures for octa-tethered alkyl-POSS systems were found to exhibit a linear-like trend as the tether length increased from C_5 to C_{10}, as is seen for the *n*-alkanes.

Chapter V

DEVELOPMENT OF THE GC-SAFT-VR EOS

5.1 Introduction

There is an increasing need to understand and accurately model the thermodynamics and phase behavior of complex fluid systems such as heavy hydrocarbons, branched and hyperbranched polymers, and, more generally, molecules with multiple functional groups. In such systems, molecular architecture (e.g., branching) can have an important effect on thermodynamic properties. For example, it is well known that for hydrocarbons with a given number of carbon atoms branching typically leads to a decrease in the boiling point, or conversely in critical temperature; the cloud point pressure of poly(ethylene-1-butene) at a given temperature generally decreases as the degree of polymer branching increases [130]. The nature of the functional groups in a molecule or incorporation of different functional groups into a polymer backbone also strongly influences thermodynamic properties and phase behavior. For example, poly (vinyl acetate) (PVAc) is found to be more CO_2 soluble than poly (methyl acrylate) (PMA) even though the PMA repeat group has the same number of carbon, hydrogen, and oxygen atoms as PVAc [131].

While experimental thermodynamic and phase behavior data is essential to the development of accurate theoretical tools, experiments alone are unable to quantify the effects of molecular structure and composition on the phase behavior of pure fluids and their mixtures, due to the shear number of experiments that would be needed for a systematic study. Equations of state (EOS) can be used to calculate the thermodynamic

properties of pure fluids and their mixtures, however, traditional EOSs like cubic equations which dominate in the study of simple fluids, tend to give poor predictions for complex fluids and their mixtures, such as polymers and associating systems as they do not explicitly take into account the nonsphericity of the molecules and the association interactions. Statistical-mechanics-based EOSs such as the SAFT EOS are an attractive alternative as, being molecular-based, the model parameters are related to the molecular shape, size and interactions of the molecules and so tend to lead to more robust and predictive approaches.

Within the SAFT-VR approach, and typically most SAFT-based equations of state, molecules are treated as homonuclear chains composed of identical tangentially bonded segments. For example, an alkane is generally modeled as a chain of identical segments, the SAFT parameters for which are obtained by fitting to vapor pressure and saturated liquid density data. With this approach it is assumed that each alkane has its own individual set of parameters. In order to develop a more predictive approach several authors [34, 62, 132-137] have shown that simple empirical relationships for the *n*-alkane parameters can be obtained by correlating the parameters for individual alkanes against molecular weight or the number of carbon atoms. This allows for the extrapolation of the model parameters to long-chain *n*-alkanes for which limited experimental data is available and linear polymers such as polyethylene (PE) [6, 138], since PE can be considered to be a very long hydrocarbon chain. However, the extension of such techniques beyond polyolefins to functionalized polymers and copolymers has met with limited success (see for example [139]). Additionally the use of polymer PVT data (in place of the phase coexistence data typically used for small molecules) to determine

polymer parameters is generally not successful [140-142]. Several alternative methods for developing polymer parameters have been proposed, such as using empirical corrections to the parameters for polyethylene [143] and a combination of fitting to polymer densities and polymer-solvent cloud point data [65, 144]. Pseudo-group contribution type approaches have also been proposed to determine the parameters for polymer systems; typically the value of m and σ are obtained from a linear summation of the values for each characteristic group defined in the molecule and the energy parameters determined from either a fit to vapor pressure and liquid density data for the monomer, and then used for the corresponding polymer, or a fit to binary cloud point data [145].

A common feature of these previous studies is the *ad hoc* way in which parameters are put together, which no doubt impacts the need to use pure component and/or cross parameters fitted to experimental mixture data, so removing predictive capability. To move away from this trend and towards a predictive approach uniformity in the parameters and their means of determination needs to be introduced, which should facilitate the use of parameters in a more transferable fashion and reduce the reliance on experimental data. Towards this goal we have developed the hetero-SAFT-VR approach that allows the study of chains composed of segments of different size and/or energy parameters and leads naturally to the development of a group-contribution-like formalism. The GC-SAFT-VR approach allows us to accurately capture the nature of the molecular structure, including branching, and functional groups within a molecule in a precise, rather than *ad hoc* way through effective size parameters. Using the GC-SAFT-

VR approach we can build a database of functional group parameters that can be used to model not only small molecules but also polymers containing those functional groups.

Recently, Tobaly *et al*., have proposed a group-contribution SAFT-based equation of state (GC-SAFT) [146-149], in which the representative groups are defined according to the molecules composition and structure; however, the molecules are modeled as homonuclear chains as the model parameters are obtained by averaging the parameters for the different groups. The GC-SAFT method has been tested using the original SAFT, PC-SAFT, and SAFT-VR equations and applied to study the phase behavior of pure linear hydrocarbons [146], linear alcohols [146] and their binary mixtures [147], esters [148] and binary mixtures of H_2 + n-alkanes and CO_2 + n-alkanes [149]. In general the GC-SAFT equation provides good predictions for the phase behavior of short-chain fluids, though increased deviations from experimental data are observed for the vapor pressures of longer-chain fluids (i.e. C > 16) and in the study of mixture systems binary interaction parameters fitted to experimental mixture data are needed.

In this work, we develop a group-contribution method based on the hetero-SAFT-VR EOS proposed and validated by the authors [8, 64] in order to develop a more physically realistic model for real fluids, i.e., one in which the segments of the model chain can have different size and/or energy parameters in order to mimic the natural heterogeneity of molecules. Such a model allows a quantitative description of the effects of molecular architecture and molecular composition on the thermodynamic properties of fluids, and provides a clear way to determine parameters for polymers based on the functional groups in the repeat unit. The remainder of the chapter is organized as follows. In section 5.2 we provide a description of the molecular model used in the GC-SAFT-VR

equation; details of the parameter regression and results for alkanes, branched alkanes, 1-alkenes, alkylbenzene, ketones, esters, and their binary mixtures are presented in section 5.3; finally conclusions are drawn in section 5.4.

5.2 Models

As described in section 2.1, the hetero-SAFT-VR approach models fluids as chains composed of segments of different size and/or energy. The key functional groups can be defined and parameterized in a group-contribution concept. This allows us to model a wide variety of organic compounds using the GC-SAFT-VR approach. For example, *n*-alkanes are modeled as chains of CH_2 groups capped by a CH_3 group at each end. After determining parameters for the CH_2 and CH_3 groups, parameters for other key functional groups can be regressed from experimental data of compounds for the same family. In particular, branched alkanes, ketones, and alkylbenzenes have been selected for parameterization of a single additional group i.e., the CH group, the carbonyl group (C=O), and the benzyl group respectively. In turn we can use the fitted parameters for these functional groups to determine the GC-SAFT-VR parameters for other functional groups such as the CH_3O and CH_2O groups in esters.

5.3 Results

We have developed the GC-SAFT-VR approach and in this initial study determined the parameters for eight classes of functional groups by fitting to experimental data for selected members of different chemical families, namely *n*-alkanes, branched alkanes, 1-alkenes, alkyl-benzenes, ketones, and esters. We will first present results for the phase

behavior of each class of pure fluids using the GC-SAFT-VR approach and then illustrate the transferability of the groups determined through the study of molecules not included in the fitting process and the study of mixture systems, without additional fitting to experimental data.

5.3.1 Pure Fluids

As discussed above, in the GC-SAFT-VR approach we describe the n-alkanes as chains composed of two types of segments (CH_2 and CH_3) the parameters for which are obtained by fitting to experimental data for selected alkanes, namely propane (C_3H_8) - decane ($C_{10}H_{22}$), hexadecane ($C_{16}H_{34}$), and eicosane ($C_{20}H_{42}$). Methane and ethane were naturally excluded from the fitting process due to their size and anomalous properties, and the two heavier compounds included in order to obtain parameters suitable for both light and heavy alkanes. In order to determine the number of segments *m* in the model chain, we make use of the simple relationship

$$m = 1/3(C-1)+1, \tag{5.1}$$

developed in earlier work that has proven to provide a good description of the critical temperatures and pressures of linear alkanes [150, 151] and has been widely adopted in the study of the *n*-alkanes. In the long chain limit equation (5.1) gives a value for *m* for methylene groups (CH_2) of 0.333, and since the total number of segments in the *n*-alkane molecule is equal to:

$$m = 2m_{CH_3} + (C-2)m_{CH_2} \tag{5.2}$$

where *C* is the number of carbon atoms, the value of *m* for the methyl group (CH_3) can easily be calculated as $m_{CH_3} = 0.667$. The parameters determined for the CH_2 and CH_3

groups are presented in Table 12 - Table 14. We note that the parameters determined for the CH_2 group are very close to those determined from simple empirical relations for the SAFT-VR parameters with molecular weight [7].

The GC-SAFT-VR description of the *n*-alkane phase diagrams in comparison with experimental data are presented in Figure 24 and Figure 25 and the average absolute deviations (AAD) for the vapor pressure and liquid density are reported in Table 15 and Table 16 respectively. We find that the average deviation for vapor pressure is less than 8% for all the *n*-alkanes used in the fitting process except for propane, which was the smallest *n*-alkane molecule considered and so the alkane for which the influence of the CH_3 groups will be greatest. Although the agreement with experimental data is not as accurate as that obtained by fitting parameters separately for each alkane, we do find that our results are generally more accurate than those obtained when using parameters determined from correlations of the SAFT-VR parameters with molecular weight or carbon number [7]; for comparison the AAD values for results obtained from the empirical expressions of Paricaud *et al*. are also reported in Table 15 and Table 16. Similar behavior is observed if the expressions proposed by McCabe *et al*. are used [127].

Table 12: GC-SAFT-VR parameters for segment size and segment number.

Groups	σ (Å)	m_i
CH_3	3.737	0.667
CH_2	4.041	0.333
CH	3.925	0.100
C=O	3.496	0.580
CH_2=CH	3.574	1.052
C_6H_5	3.158	2.693
CH_2O	2.950	1.000
CH_3O	3.078	1.330

Table 13: Segment-segment energy well depth parameters ε_{ij}.

Type	CH_3	CH_2	CH	C=O	CH_2=CH	C_6H_5	CH_2O	CH_3O
CH_3	234.250	235.735	153.064	307.223	226.675	165.521	157.702	191.144
CH_2	235.735	237.230	154.034	309.171	228.112	166.570	158.702	192.356
CH	153.064	154.034	100.015	200.746	148.114	108.155	103.046	124.897
C=O	307.223	309.171	200.746	402.929	297.288	217.084	206.829	250.689
CH_2=CH	226.675	228.112	148.114	297.288	219.344	160.168	152.602	184.962
C_6H_5	165.521	166.570	108.155	217.084	160.168	116.957	111.432	135.062
CH_2O	157.702	158.702	103.046	206.829	152.602	111.432	106.168	128.682
CH_3O	191.144	192.356	124.897	250.689	184.962	135.062	128.682	155.970

Table 14: Segment-segment energy range parameters λ_{ij}.

Type	CH_3	CH_2	CH	C=O	CH_2=CH	C_6H_5	CH_2O	CH_3O
CH_3	1.492	1.583	1.725	1.685	1.529	1.734	1.546	1.566
CH_2	1.583	1.667	1.804	1.586	1.621	1.822	1.645	1.662
CH	1.725	1.804	1.946	1.920	1.766	1.979	1.804	1.818
C=O	1.685	1.586	1.920	1.891	1.728	1.953	1.764	1.558
CH_2=CH	1.529	1.621	1.766	1.728	1.568	1.781	1.589	1.608
C_6H_5	1.734	1.822	1.979	1.953	1.781	2.021	1.824	1.840
CH_2O	1.546	1.645	1.804	1.764	1.589	1.824	1.614	1.635
CH_3O	1.566	1.662	1.818	1.558	1.608	1.840	1.635	1.655

Table 15: The average deviation of vapor pressures between experimental data [152] and correlated results for pure alkanes.

n-alkanes	T (K)	N_{pt}	AAD *P* (%)	AAD *P** (%)
Propane	130-360	24	13.91	10.35
n-Butane	160-420	27	5.72	4.35
n-Pentane	180-460	29	4.77	12.06
n-Hexane	200-500	31	6.85	16.70
n-Heptane	220-560	33	4.52	15.58
n-Octane	240-560	33	3.98	15.21
n-Nonane	250-590	35	4.20	13.57
n-Decane	270-610	35	3.68	12.54
n-Dodecane	300-650	36	3.28	9.01
n-Hexadecane	350-720	38	5.27	5.88
n-Eicosane	390-760	38	7.13	7.01

* Obtained from parameters correlated with molecular weight [7]

Table 16: The average deviation of liquid densities between experimental data [152] and correlated results for pure alkanes.

n-alkanes	T (K)	N_{pt}	AAD D_{Liq} (%)	AAD D_{Liq}* (%)
Propane	100-360	27	4.03	2.93
n-Butane	140-420	29	3.59	2.81
n-Pentane	150-460	32	2.57	2.21
n-Hexane	180-500	33	2.48	2.32
n-Heptane	190-540	36	3.69	3.17
n-Octane	220-560	35	2.70	2.40
n-Nonane	220-590	38	2.87	2.41
n-Decane	250-610	37	2.68	2.18
n-Dodecane	270-650	39	2.64	2.09
n-Hexadecane	300-720	43	2.96	2.20
n-Eicosane	310-760	46	2.26	1.64

* Obtained from parameters correlated with molecular weight [7]

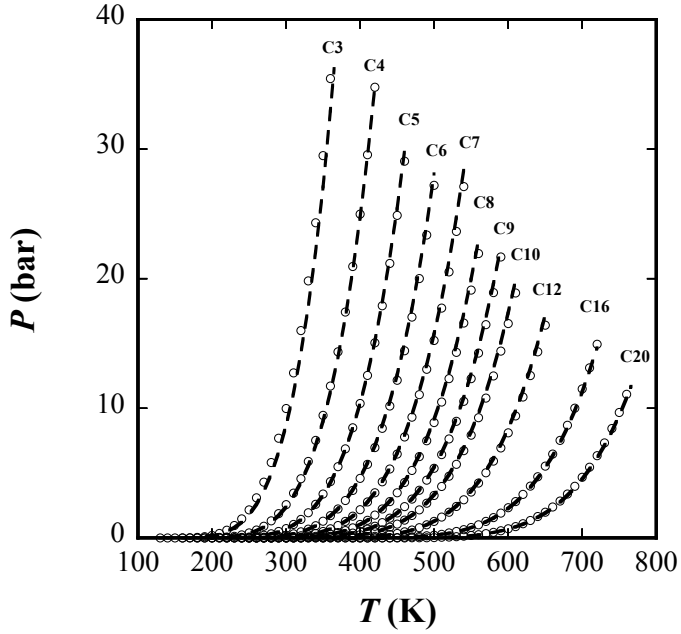

Figure 24: Comparison of GC-SAFT-VR description with experimental vapor pressure data for selected light *n*-alkanes from propane to *n*-eicosane (from left to right); experimental data [152] are represented by circles and calculated results by dashed lines.

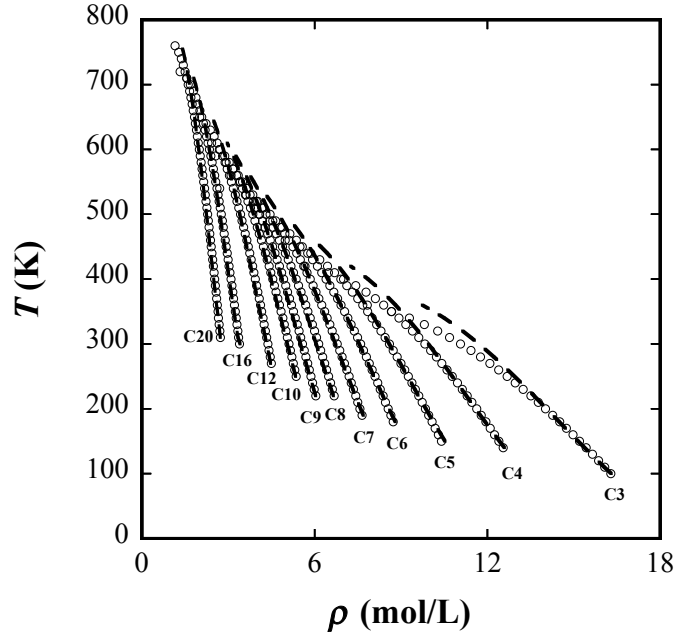

Figure 25: Comparison of GC-SAFT-VR description with experimental saturated liquid density data for selected light *n*-alkanes from propane to *n*-eicosane (from right to left); experimental data [152] are represented by circles and calculated results by dashed lines.

Having presented the agreement with experimental data for *n*-alkanes included in the fitting process we now test the GC-SAFT-VR approach by studying the phase diagrams of heavier alkanes, not included in the fitting process. Predictions for the vapor pressures and saturated liquid densities of undecane ($C_{11}H_{24}$) - hexatriacontante ($C_{36}H_{74}$) are compared with experimental data in Figure 26 and Figure 27. The corresponding AAD values for the vapor pressures and liquid densities are reported in Table 17 and Table 18. For comparison we again provide AAD values for the SAFT-VR description of these *n*-alkanes obtained using parameters from the empirical expressions of Paricaud [7]. Generally, we find that the deviations between the GC-SAFT-VR predictions and experimental data for the saturated liquid density are much smaller than those obtained for predictions for the vapor pressure, indicating that the vapor pressure is a more sensitive quantity.

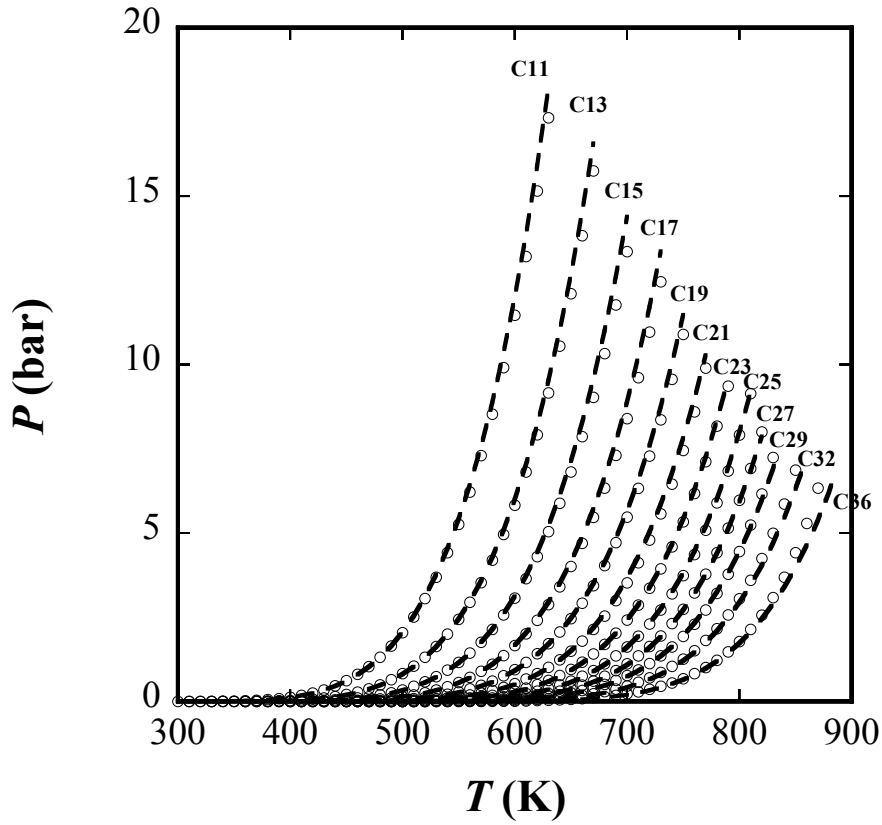

Figure 26: Comparison of GC-SAFT-VR prediction with experimental vapor pressure data for selected heavy *n*-alkanes from *n*-undecane to *n*-dotriacotane (from left to right); experimental data [152] are represented by circles and calculated results by dashed lines.

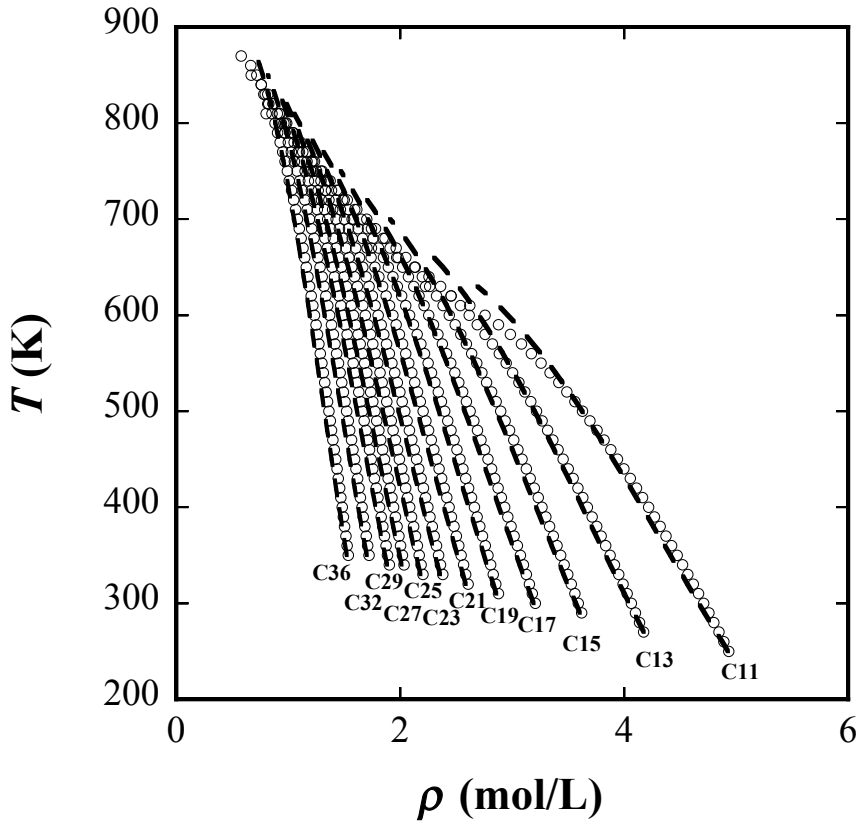

Figure 27: Comparison of GC-SAFT-VR prediction with experimental saturated liquid density data for selected heavy *n*-alkanes from *n*-undecane to *n*-dotriacotane (from right to left); experimental data [152] are represented by circles and calculated results by dashed lines.

Table 17: The average deviation of vapor pressures between experimental data [152] and predicted results for pure alkanes.

n-alkanes	T (K)	N_{pt}	AAD *P* (%)	AAD *P** (%)
n-Undecane	280-630	36	4.26	12.98
n-Tridecane	310-670	37	3.27	9.01
n-Tetradecane	320-690	38	3.88	7.67
n-Pentadecane	330-700	38	4.09	6.21
n-Heptadecane	360-730	38	4.93	5.52
n-Octadecane	370-740	38	6.53	6.32
n-Nonadecane	380-750	38	7.27	6.53
n-Heneicosane	400-770	38	8.64	8.29
n-Docosane	410-780	38	10.93	10.46
n-Tricosane	410-790	39	9.58	8.80
n-Tetracosane	410-800	39	10.55	10.06
n-Pentacosane	430-810	39	11.49	11.73
n-Hexacosane	440-810	38	11.47	10.96
n-Heptacosane	450-820	38	9.97	10.74
n-Octacosane	450-830	39	14.02	14.28
n-Nonacosane	460-830	38	15.80	15.87
n-Triacontane	470-840	38	16.75	19.28
n-Dotriacontane	480-850	38	20.11	22.93
n-Hexatriacontane	500-870	38	24.26	26.78

* Obtained from parameters correlated with molecular weight [7]

Table 18: The average deviation of liquid densities between experimental data [152] and predicted results for pure alkanes.

n-alkanes	T (K)	N_{pt}	AAD D_{Liq} (%)	AAD D_{Liq}* (%)
n-Undecane	250-630	39	2.50	1.99
n-Tridecane	270-670	41	2.76	2.02
n-Tetradecane	280-690	42	2.99	2.24
n-Pentadecane	290-700	42	2.56	1.87
n-Heptadecane	300-730	44	2.59	1.92
n-Octadecane	310-740	44	2.60	1.90
n-Nonadecane	310-750	45	2.56	1.86
n-Heneicosane	320-770	46	2.64	1.90
n-Docosane	320-780	47	2.75	1.98
n-Tricosane	330-790	47	2.82	2.03
n-Tetracosane	330-800	48	2.92	2.12
n-Pentacosane	330-810	49	3.20	2.39
n-Hexacosane	330-810	49	2.65	1.83
n-Heptacosane	340-820	49	2.91	2.07
n-Octacosane	340-830	50	3.11	2.27
n-Nonacosane	340-830	50	2.82	1.96
n-Triacontane	340-840	51	3.25	2.36
n-Dotriacotane	350-850	51	3.10	2.22
n-Hexatriacontane	350-870	53	3.08	2.27

* Obtained from parameters correlated with molecular weight [7]

In order to describe the heterogeneity of branched alkanes, a CH group needs to be defined. The parameters for the CH group were determined by fitting to vapor pressure and saturated liquid density data for two families of branched alkanes, methylalkanes and ethylalkanes, while using the CH_2 and CH_3 group parameters already determined. The GC-SAFT-VR description of the branched alkanes for fitting in comparison with experimental data are presented in Figure 28 and Figure 29 and the parameters obtained for the CH group given in Table 12 - Table 14. The deviations between the GC-SAFT-VR description of the phase diagrams and experimental data are reported in Table 19. From Table 19 we note that the agreement with experimental data is

good with the deviations obtained being similar to those observed for the *n*-alkanes; the liquid densities are ~4% and the deviations for the vapor pressures generally less than 8%. As a test of the theory, 2-methyl heptane, five dimethyl-branched alkanes, and squalane were also investigated and the predictive results are plotted in Figure 30 and Figure 31 and the deviation are included in Table 20. We find that the liquid density of these systems is very well predicted by the GC-SAFT-VR approach, however the vapor pressure is overpredicted as the number of branches increases. The overprediction might be caused by the effect of the interaction between the branches of CH_3 and the group CH directly linked to CH_3.

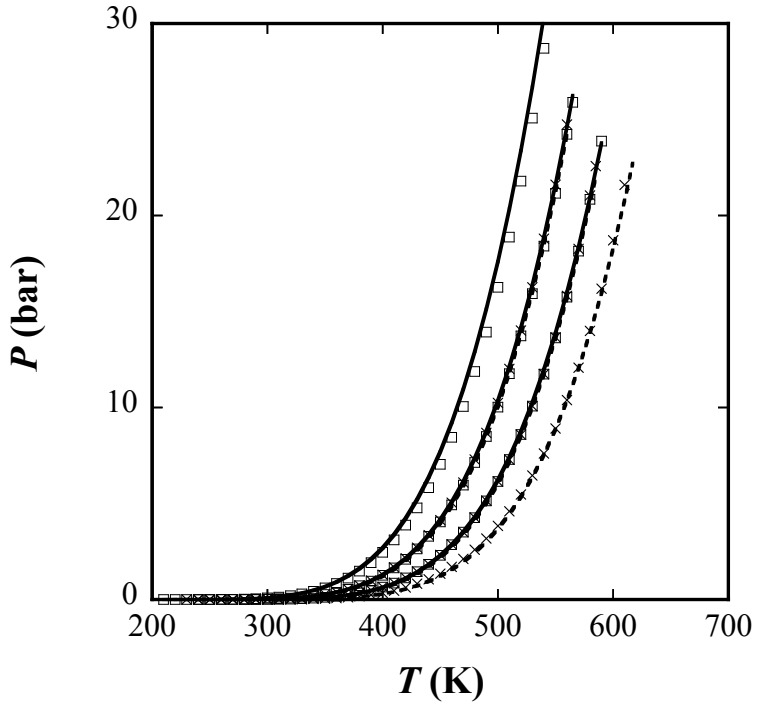

Figure 28: Comparison of GC-SAFT-VR description with experimental vapor pressure data [152] for selected methyl alkanes from 4-methylheptane to 5-methylnonane (from left to right) represented by crosses and for ethyl alkanes from 3-ethylpentane to 3-ethylheptane represented by squares (from left to right); theoretical calculations for methyl alkanes and ethyl alkanes are represented by dashed and solid lines respectively.

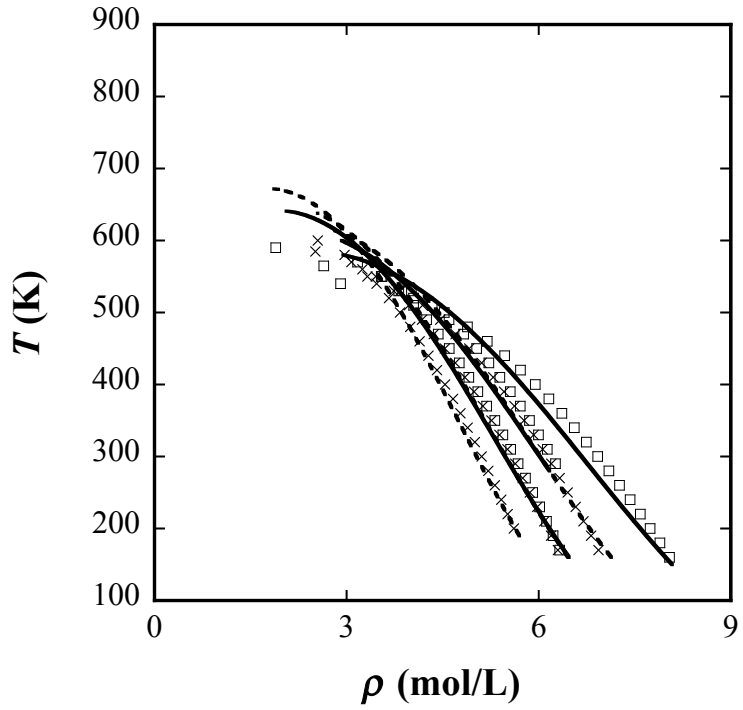

Figure 29: Comparison of GC-SAFT-VR description with experimental saturated liquid density data [152] for selected methyl alkanes from 4-methylheptane to 5-methylnonane (from right to left) represented by crosses and for ethyl alkanes from 3-ethylpentane to 3-ethylheptane represented by squares (from right to left); theoretical calculations for methyl alkanes and ethyl alkanes are represented by dashed and solid lines respectively.

Table 19: The average deviation of vapor pressures and liquid densities between experimental data [152] and correlated results for pure branched alkanes.

Branched alkanes	**T (K)**	**N_{pt}**	**AAD *P* (%)**	**AAD D_{Liq} (%)**
4-methylheptane	160-560	41		3.16
	230-560	34	4.82	
4-methyloctane	160-585	44		3.31
	240-585	36	5.79	
5-methylnonane	190-610	43		4.28
	260-610	36	7.65	
3-ethylpentane	150-540	40		3.91
	210-540	34	15.80	
3-ethylhexane	280-565	30		4.97
	280-565	30	2.69	
3-ethylheptane	160-590	44		4.12
	240-590	36	1.99	

Table 20: The average deviation of vapor pressures and liquid densities between experimental data [152] and predicted results for pure branched alkanes.

Branched alkanes	T (K)	N_{pt}	AAD *P* (%)	AAD D_{Liq} (%)
2-methyl heptane	170-550	39		3.02
	225-550	33	9.83	
2, 4-dimethylhexane	275-550	29		5.98
	275-550	29	14.49	
2, 6-dimethylheptane	175-575	41		4.35
	245-575	34	19.08	
2, 7-dimethyloctane	220-600	39		4.42
	260-600	35	18.09	
Squalane	270-760	63		2.55
	440-760	43	43.25	

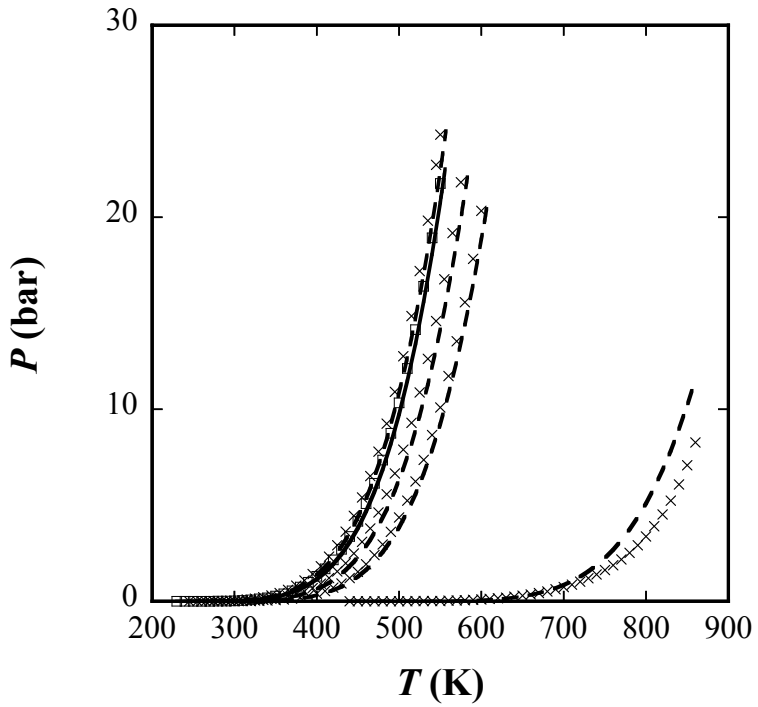

Figure 30: Comparison of GC-SAFT-VR prediction with experimental vapor pressure data [152] for 2, 4-dimethylhexane, 2, 6-dimethylheptane, 2, 7-dimethyloctane, and squalane (from left to right) represented by crosses and 2-methyl heptane represented by squares; theoretical calculations for multi-branched alkanes and 2-methyl heptane are represented by dashed and solid lines respectively.

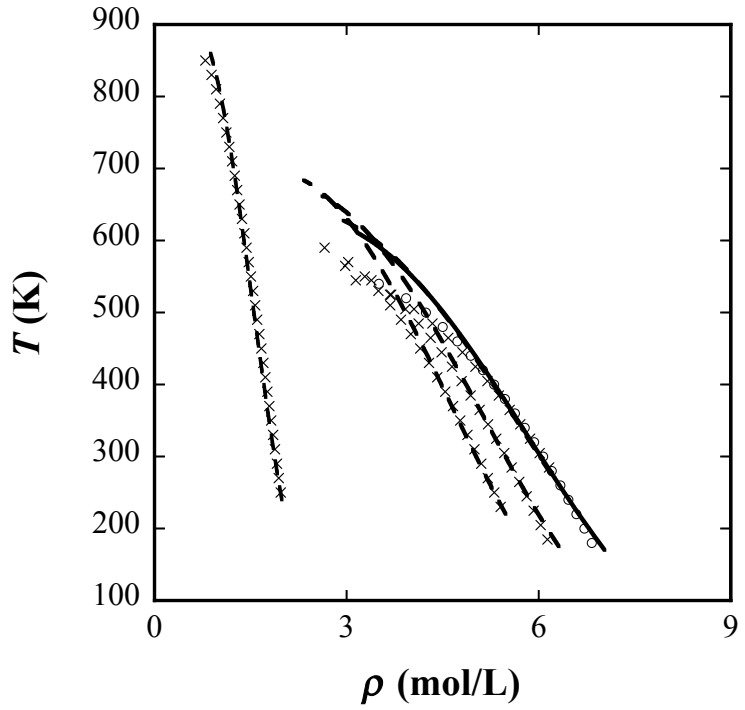

Figure 31: Comparison of GC-SAFT-VR prediction with experimental saturated liquid density data [152] for 2, 4-dimethylhexane, 2, 6-dimethylheptane, 2, 7-dimethyloctane, and squalane (from right to left) represented by crosses and 2-methyl heptane represented by squares; theoretical calculations for multi-branched alkanes and 2-methyl heptane are represented by dashed and solid lines respectively.

In order to study unsaturated alkanes a functional group needs to be defined and parameters determined that incorporates the unsaturated C=C bond. Using the CH_2 and CH_3 groups previously defined parameters for a CH_2=CH group were determined by fitting to the experimental vapor pressures and coexisting densities for eight 1-alkenes from propene to 1-decene. The parameters for the CH_2=CH group are given in Table 12 - Table 14. The GC-SAFT-VR description of the alkene vapor pressures and liquid density for fitting are given in Figure 32 and Figure 33 and the predicted results of vapor pressure and liquid density in Figure 34 and Figure 35. In comparison to the experimental data we can see both the fitting results for short 1-alkenes from pentene to 1-decene and

prediction results for longer 1-alkene systems from 1-undecene to 1-eicosene agree very well with experimental data.

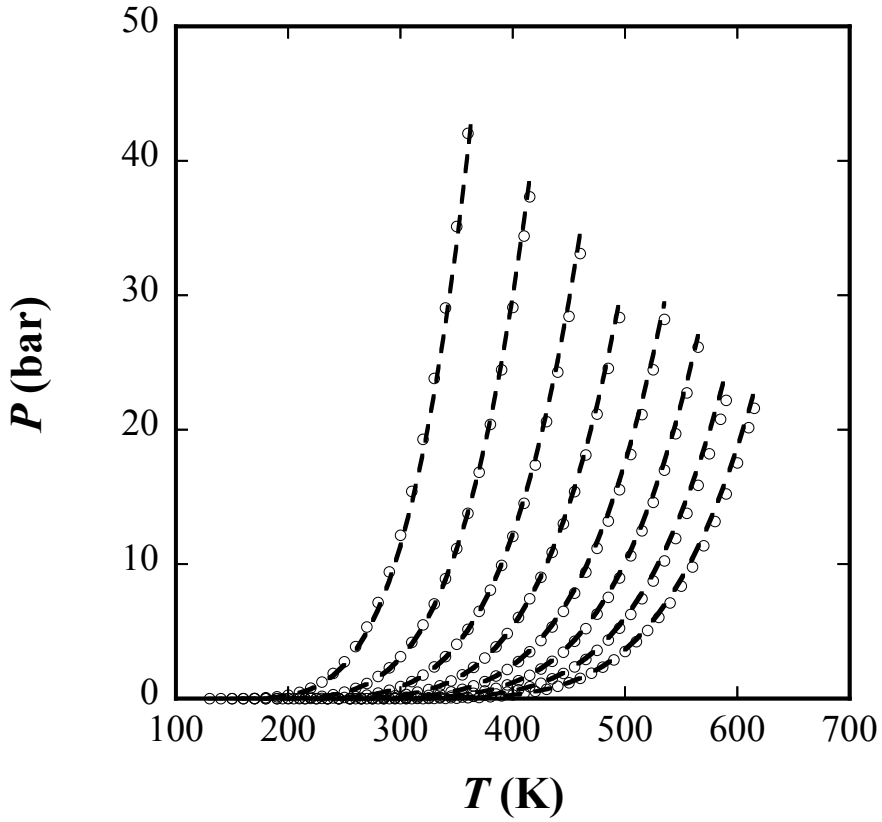

Figure 32: Comparison of GC-SAFT-VR description with experimental vapor pressure data for selected light 1-alkenes from propene to 1-decene (from left to right); experimental data [152] are represented by circles and calculated results by dashed lines.

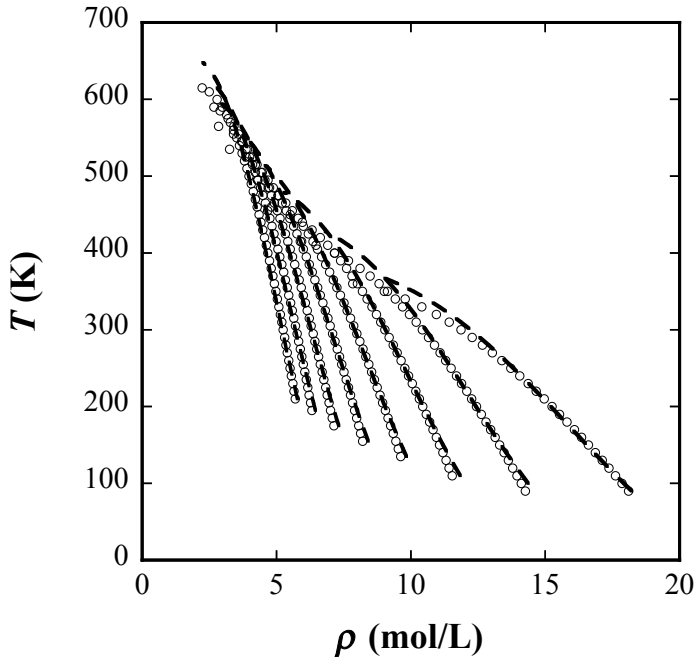

Figure 33: Comparison of GC-SAFT-VR description with experimental saturated liquid density data for selected light 1-alkenes from propene to 1-decene (from right to left); experimental data [152] are represented by circles and calculated results by dashed lines.

Table 21: The average deviation of vapor pressures and liquid densities between experimental data [152] and correlated results for pure alkenes.

Alkenes	**T (K)**	**N_{pt}**	**AAD *P* (%)**	**AAD D_{Liq} (%)**
Propene	90-360	28		2.56
	130-360	24	7.27	
1-Butene	90-415	34		3.44
	150-415	28	4.71	
1-Pentene	110-460	36		2.79
	170-460	30	3.90	
1-Hexene	135-495	37		2.29
	195-495	31	1.71	
1-Heptene	155-535	39		2.50
	215-535	36	3.64	
1-Octene	175-565	40		2.34
	235-565	34	3.05	
1-Nonene	195-590	41		2.26
	245-590	36	4.40	
1-Decene	210-615	42		2.63
	260-615	37	3.51	

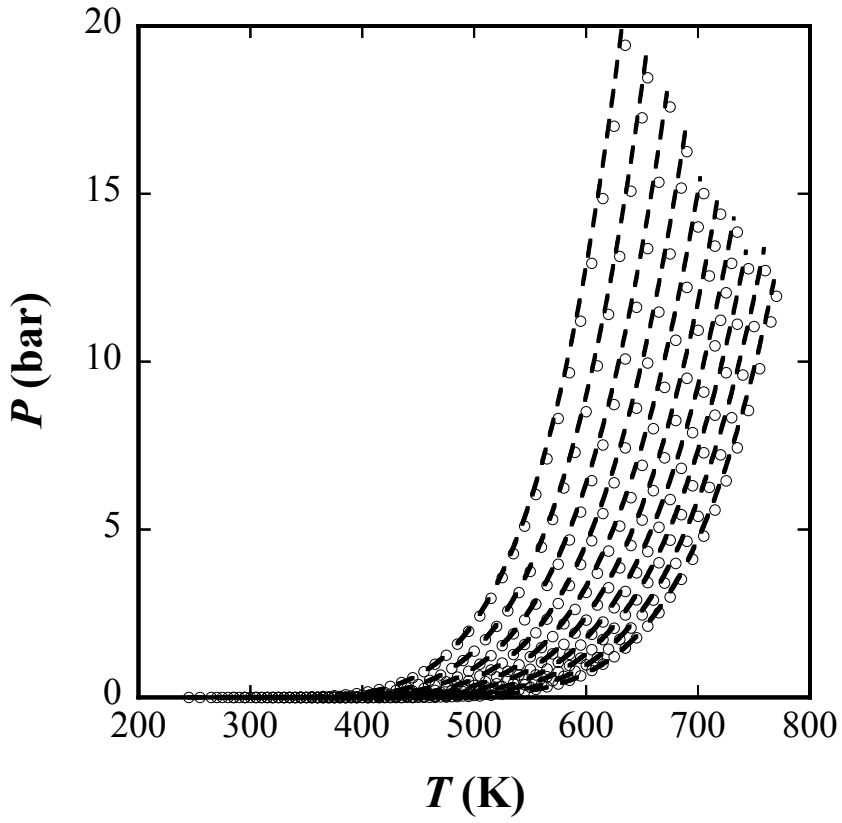

Figure 34: Comparison of GC-SAFT-VR prediction with experimental vapor pressure data for selected heavy 1-alkenes from 1-undecene to 1-eicosene (from left to right); experimental data [152] are represented by circles and calculated results by dashed lines.

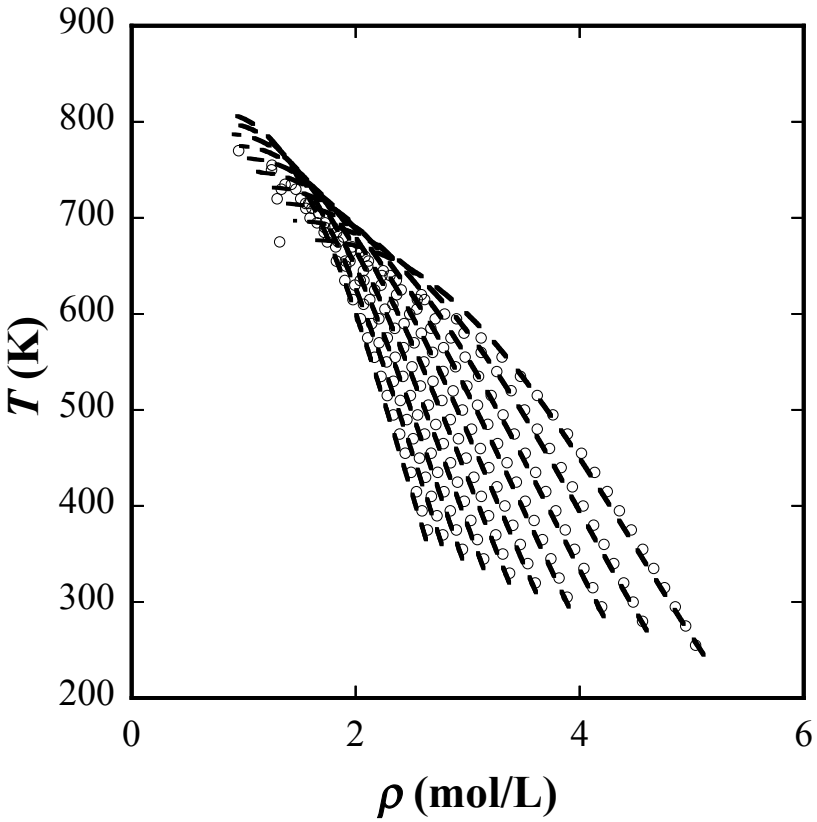

Figure 35: Comparison of GC-SAFT-VR prediction with experimental saturated liquid density data for selected heavy 1-alkenes from 1-undecene to 1-eicosene (from right to left); experimental data [152] are represented by circles and calculated results by dashed lines.

Table 22: The average deviation of vapor pressures and liquid densities between experimental data [152] and predicted results for pure alkenes.

Alkenes	T (K)	N_{pt}	AAD *P* (%)	AAD D_{Liq} (%)
1-Undecene	225-635	42		2.33
	285-635	36	4.23	
1-Dodecene	240-655	43		2.48
	290-655	38	4.52	
1-Tridecene	255-675	43		3.55
	305-675	38	4.14	
1-Tetradecene	265-690	44		2.85
	315-690	39	4.53	
1-Pentadecene	270-705	45		2.88
	330-705	39	5.58	
1-Hexadecene	280-720	46		3.31
	340-720	40	6.19	
1-Heptadecene	285-735	48		3.56
	355-735	41	7.42	
1-Octadecene	295-745	46		2.66
	365-745	39	7.45	
1-Nonadecene	300-760	47		3.75
	380-760	39	7.26	
1-Eicosene	305-770	48		3.28
	385-770	40	7.32	

Having defined parameters for the groups forming the "backbone" of organic molecules we can now define parameters for common functional groups in other classes of organic molecules. In this initial study we have focused on ketones, esters and alkylbenzenes, since the carbonyl (C=O), CH_2O, CH_3O, and benzenyl groups (C_6H_5) are common functional groups in polymers. In order to determine parameters for the carbonyl group we fitted to experimental vapor pressure and saturated liquid density data for 3-pentanone, 3-hexanone, 4-heptanone, 4-octanone, 5-nonanone in which the carbonyl group lies in the center of the ketone chain. Ketones have very strong dipolar interactions due to the carbonyl group, which is not explicitly described in the original SAFT-VR approach but captured through the large value of the range parameter λ. The

regressed parameters for C=O are presented in Table 12 - Table 14. The transferability of the ketone parameters was tested through the prediction of the phase diagrams of 6-undecanone, 8-pentadecanone, and 16-hentriacontanone. The results are in good agreement with experimental data for both the vapor pressure and saturated liquid densities as can be seen in Figure 36 and Figure 37 and from the AAD values of ~5% and 2% (reported in Table 23 and Table 24) for the vapor pressures and saturated liquid densities respectively.

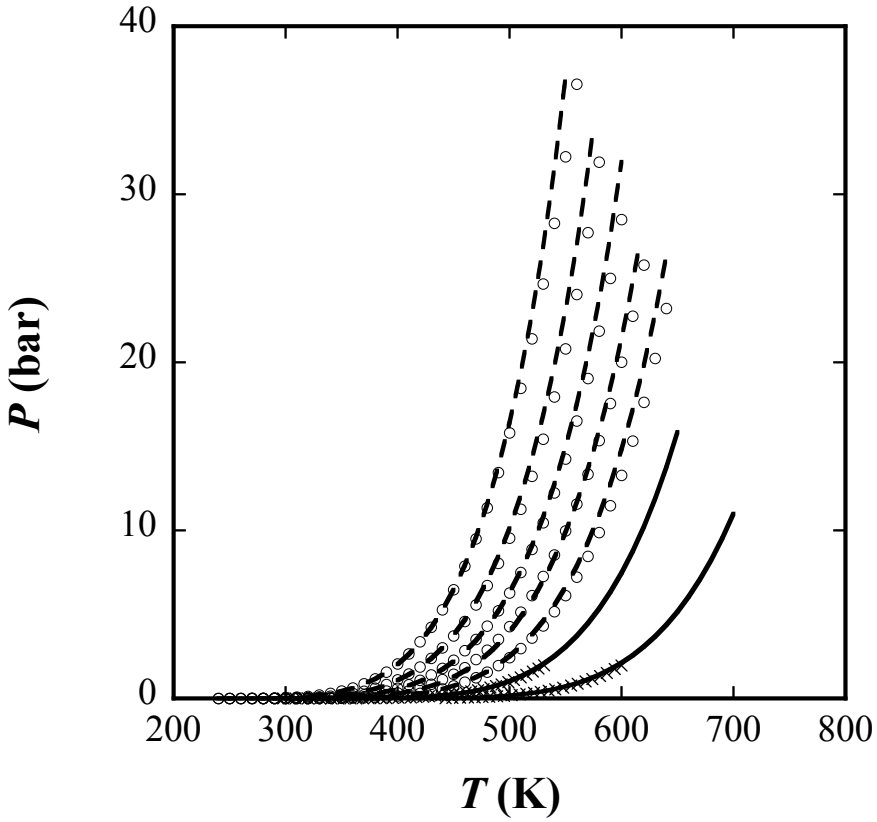

Figure 36: Comparison of GC-SAFT-VR description with experimental vapor pressure data for selected ketones from 3-pentanone to 8-pentadecanone (from left to right); experimental data [152] are represented by the symbols, correlated results and predicted results by dashed and solid lines respectively.

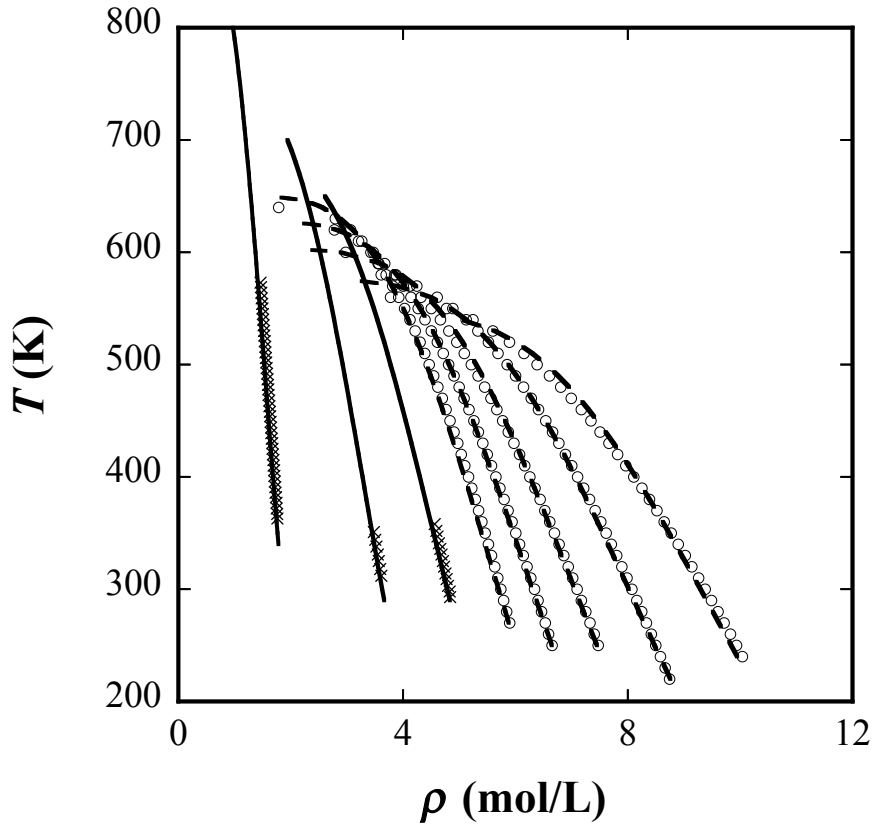

Figure 37: Comparison of GC-SAFT-VR description with experimental saturated liquid density data for selected ketones from 3-pentanone to 16-hentriacontanone (from right to left); experimental data [152] are represented by the symbols, correlated results and predicted results by dashed and solid lines respectively.

Table 23: The average deviation of vapor pressures and liquid densities between experimental data [152] and correlated results for pure ketones.

Ketones	T (K)	N_{pt}	AAD *P* (%)	AAD D_{Liq} (%)
3-pentanone	240-560	33		2.75
	240-560	33	3.04	
3-hexanone	220-580	37		1.38
	240-580	35	5.57	
4-heptanone	250-600	36		1.06
	250-600	36	7.21	
4-octanone	250-615	38		0.56
	290-615	36	7.77	
5-nonanone	270-640	38		2.10
	280-640	37	5.18	

Table 24: The average deviation of vapor pressures and liquid densities between experimental data [153] and predicted results for pure ketones.

Ketones	T (K)	N_{pt}	AAD *P* (%)	AAD D_{Liq} (%)
6-undecanone	293-358	13		0.95
	298-531	45	4.22	
8-pentadecanone	312-351	7		0.84
	443-600	25	4.08	
16-hentriacontanone	363-573	45		2.16

As discussed above, esters require the definition of two types of functional groups (i.e. CH_3O for esters having a CH_3O group next to the C=O group and CH_2O for esters with an alkyl chain rather than a terminal CH3 group). We first study esters with CH_2O and C=O groups and regress the parameters for the CH_2O group to experimental vapor pressure and liquid density for eight esters from ethyl acetate to nonyl acetate. The parameter regression for the CH_2O group is performed while keeping the parameters for the CH_2, CH_3, C=O groups and their cross interactions fixed to their previously determined values. For the molecules studied both the vapor pressure and liquid densities are correlated very well in comparison to the experimental data, as shown in Figure 38. However, we do note some deviation from the experimental data for the vapor pressures of ethyl acetate and propyl acetate which have short alkyl chains. The transferability of the fitted parameters for the CH_2O group was tested by comparing GC-SAFT-VR predictions with experimental data for ester systems not included in the fitting process. Specifically we studied butyl pentanoate, ethyl butanoate, and nonanoicacid butyl ester, which have longer alkyl groups next to the C=O and CH_2O groups and diethyl succinate which has two two C=O and CH_2O groups, as shown in Figure 40 and Figure 41 respectively. The predicted results for butyl pentanoate give a good representation for

both the experimental vapor pressures and liquid densities, while only good agreement with the liquid densities is obtained for the other three systems.

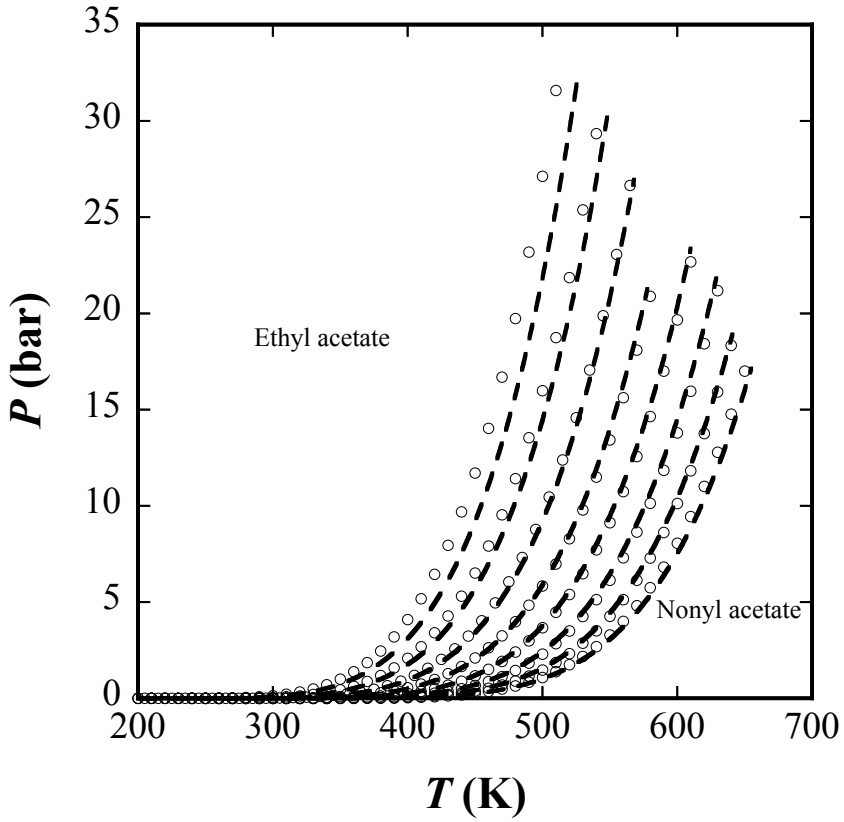

Figure 38: Comparison of GC-SAFT-VR description with experimental vapor pressure data for selected light esters from ethyl acetate to nonyl acetate (from left to right); experimental data [152] are represented by circles and calculated results by dashed lines.

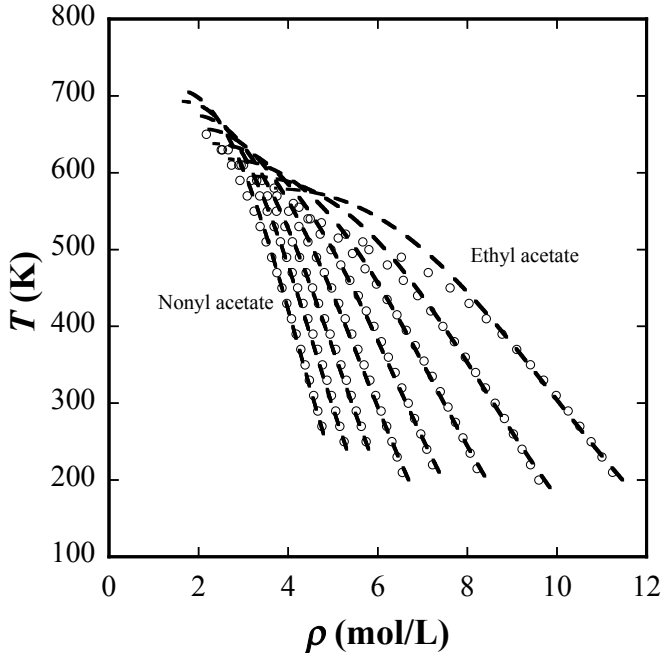

Figure 39: Comparison of GC-SAFT-VR description with experimental saturated liquid density data for selected light esters from ethyl acetate to nonyl acetate (from right to left); experimental data [152] are represented by circles and calculated results by dashed lines.

Table 25: The average deviation of vapor pressures and liquid densities between experimental data [152] and correlated results for pure esters.

Esters (CH_2O)	T (K)	N_{pt}	AAD P (%)	AAD D_{Liq} (%)
Ethyl acetate	200-510	32		2.68
	210-510	31	21.91	
Propyl acetate	200-540	35		2.58
	230-540	32	12.61	
Butyl acetate	205-565	37		2.19
	245-565	33	6.77	
Pentyl acetate	210-580	38		1.52
	260-580	33	5.80	
Hexyl acetate	200-610	42		2.08
	280-610	24	3.52	
Heptyl acetate	250-630	39		2.43
	290-630	35	7.74	
Octyl acetate	250-640	40		2.02
	300-640	35	6.11	
Nonyl acetate	260-650	40		2.89
	330-650	33	5.70	

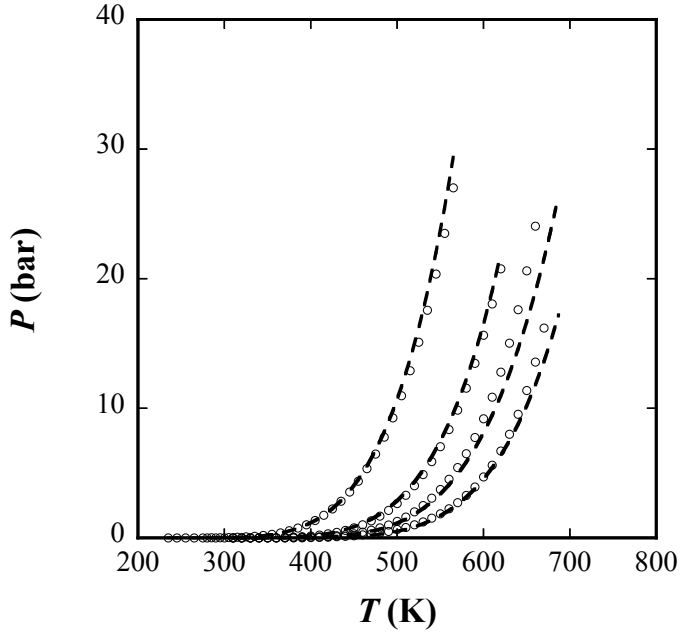

Figure 40: Comparison of GC-SAFT-VR prediction with experimental vapor pressure data for ethyl butanoate, diethyl succinate, butyl pentanoate, and nonanoicacid butyl ester (from left to right); experimental data [152] are represented by circles and calculated results by dashed lines.

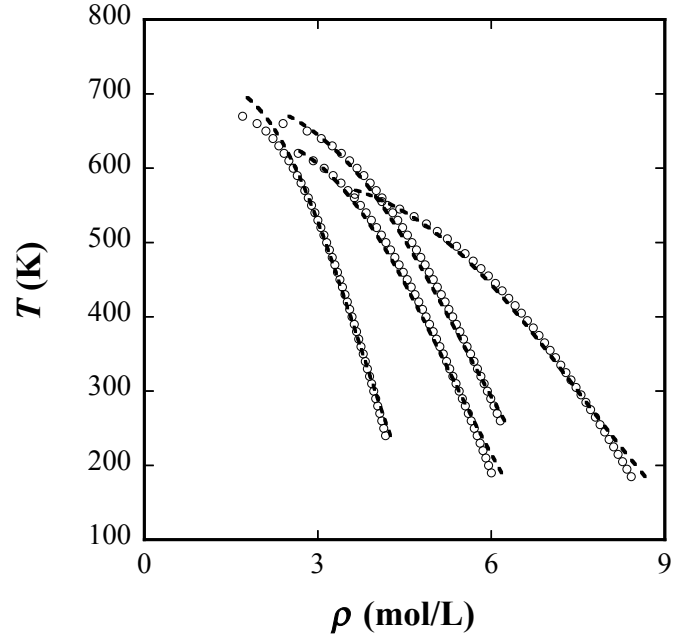

Figure 41: Comparison of GC-SAFT-VR prediction with experimental saturated liquid density data for ethyl butanoate, diethyl succinate, butyl pentanoate, and nonanoicacid butyl ester (from right to left); experimental data [152] are represented by circles and calculated results by dashed lines.

Table 26: The average deviation of vapor pressures and liquid densities between experimental data [152] and predicted results for pure esters.

Esters (CH_2O)	T (K)	N_{pt}	AAD P (%)	AAD D_{Liq} (%)
Butyl pentanoate	190 - 620	44		1.41
	250 - 620	38	10.48	
Ethyl butanoate	185 - 565	39		1.27
	215 - 565	36	8.99	
Diethyl succinate	260 – 660	41		1.78
	290 - 660	38	12.26	
Nonanoicacid butyl ester	240 - 670	44		1.90
	240 - 670	37	32.13	

Similarly, we regress the parameters for CH_3O group to the experimental data of seven esters: methyl acetate, and methyl propanoate to methyl octanoate in which the CH_3O group is the end group and always accompanied with the C=O group. The regressed parameters for the CH_3O group are listed in Table 12 - Table 14. The liquid densities of the selected esters are correlated quite well with the experimental data as presented in Table 27 and in Figure 43.

Table 27: The average deviation of vapor pressures and liquid densities between experimental data [152] and correlated results for pure esters.

Esters (CH_3O)	T (K)	N_{pt}	AAD P (%)	AAD D_{Liq} (%)
Methyl acetate	200-480	29	10.86	2.51
Methyl propanoate	210-500	30	7.46	3.10
Methyl butanoate	220-520	31	4.11	2.17
Methyl pentanoate	298.20- 402.88	22	3.25	0.28
Methyl hexanoate	287.65- 360.05	10	4.67	0.32
Methyl heptanoate	333.07- 402.89	15	1.38	0.45
Methyl octanoate	284.75- 360.55	10		0.37
	370 - 420	11	1.70	
Methyl dodecanoate	285 - 705	43		1.52
	335 - 705	38	4.95	

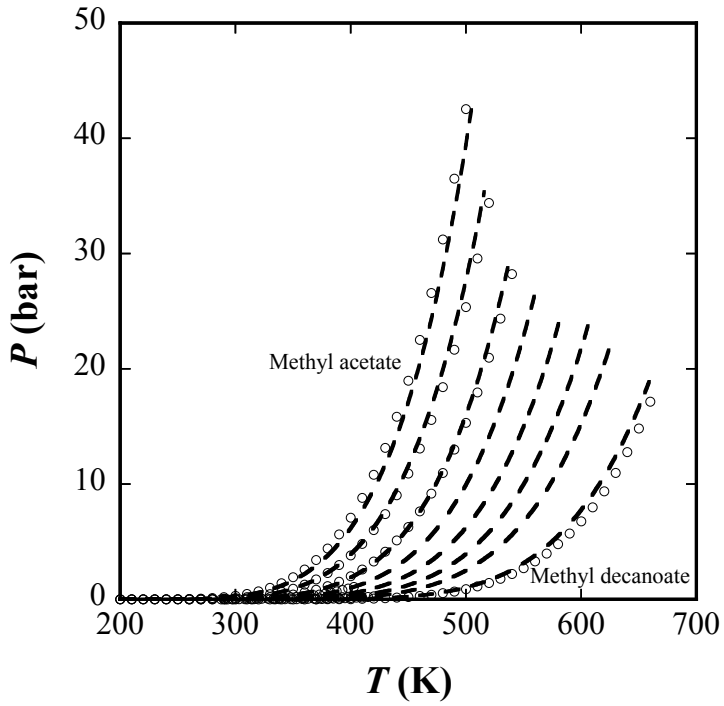

Figure 42: Comparison of GC-SAFT-VR description with experimental vapor pressure data for seven light esters from methyl acetate to methyl octanoate (from left to right); experimental data [152] are represented by circles and calculated results by dashed lines.

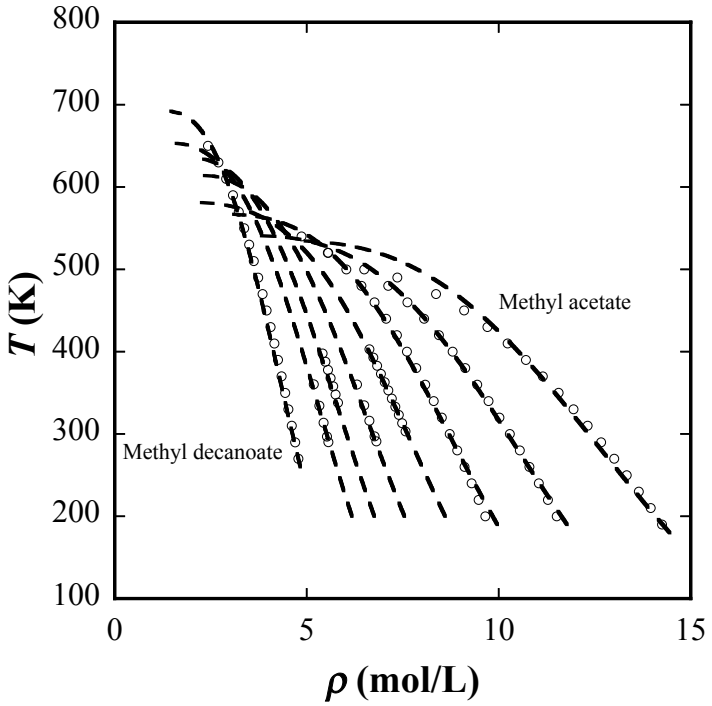

Figure 43: Comparison of GC-SAFT-VR description with experimental saturated liquid density data for seven light esters from methyl acetate to methyl octanoate (from right to left); experimental data [152] are represented by circles and calculated results by dashed lines.

We have also studied alkylbenzene systems with a single alkyl group which are represented by groups CH_2/CH_3. Short alkyl benzenes from methylbenzene to decylbenzene are selected for fitting parameters for the benzenyl group to the experimental data, for which the fitting results of the vapor pressure and liquid density are plotted in Figure 44 and Figure 45 respectively. Then we test the predictivity of the fitted parameters of benzenyl group by applying them to study longer alkylbenzene systems starting from undecylbenzene (as plotted in Figure 46). Although the deviations of liquid density properties between theoretical results and experimental data in both fitting and prediction are good, the shape of the density profile is slightly distorted as seen in Figure 45 and Figure 47. It is also observed that the deviations between the

predictive vapor pressures and experimental data become larger as the alkyl chain increases in Table 29. This is also seen in other systems containing alkyl chain mentioned previously.

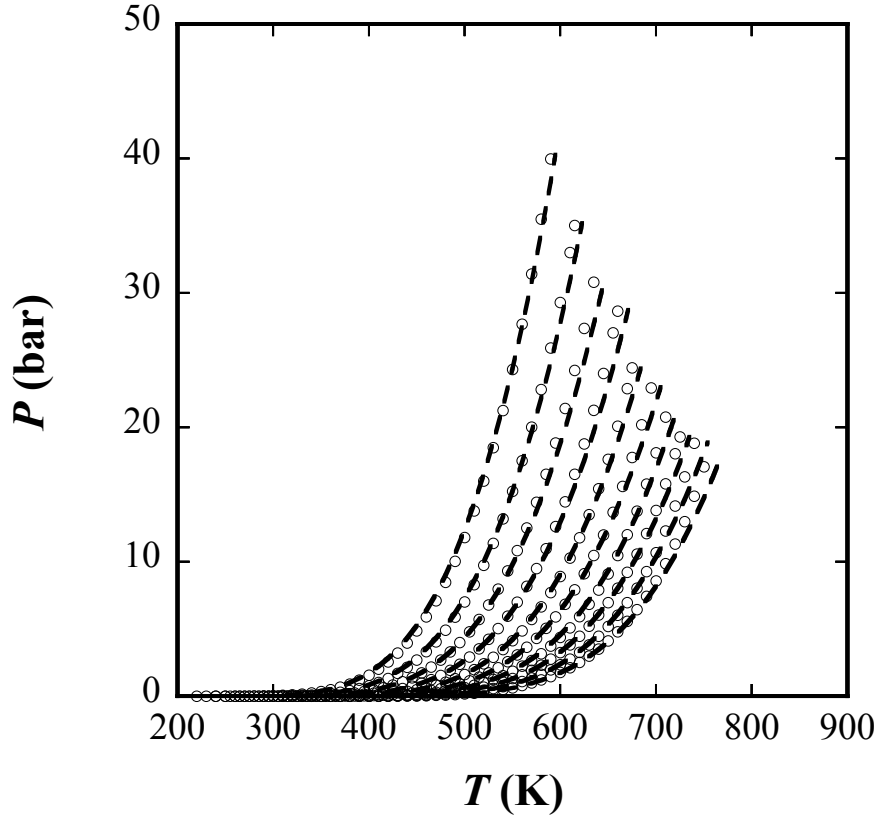

Figure 44: Comparison of GC-SAFT-VR description with experimental vapor pressure data for ten light alkylbenzenes from methylbenzene to decylbenzene (from left to right); experimental data [152] are represented by circles and calculated results by dashed lines.

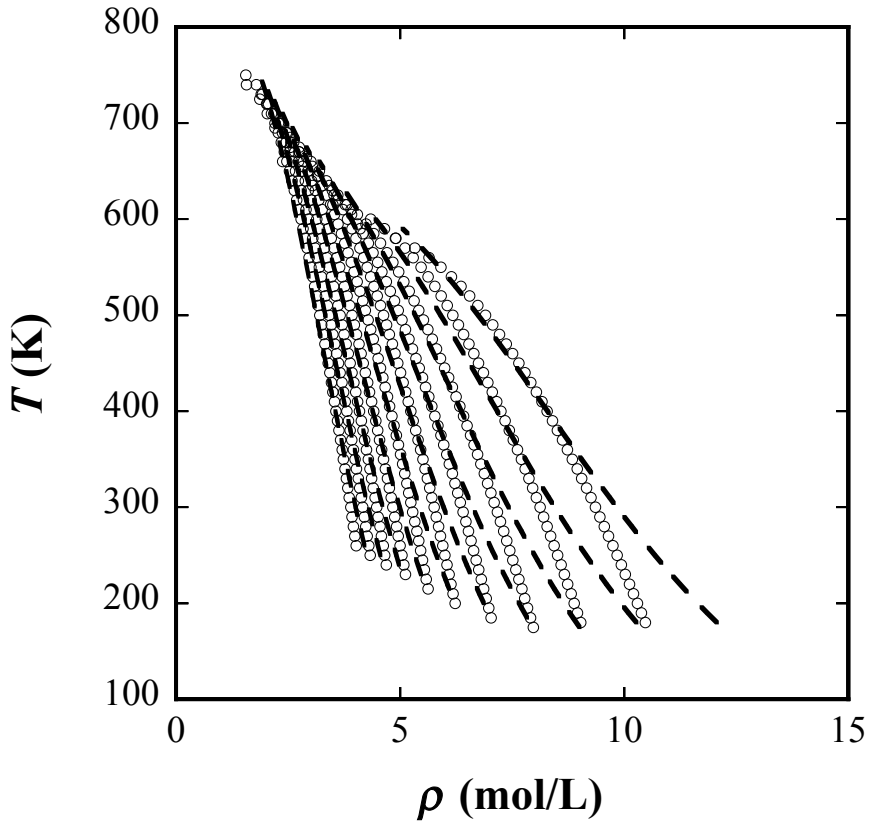

Figure 45: Comparison of GC-SAFT-VR description with experimental saturated liquid density data for ten light alkylbenzenes from methylbenzene to decylbenzene (from right to left); experimental data [152] are represented by circles and calculated results by dashed lines.

Table 28: The average deviation of vapor pressures and liquid densities between experimental data [152] and correlated results for pure alkylbenzenes.

Alkylbenzene	T (K)	N_{pt}	AAD *P* (%)	AAD D_{Liq} (%)
Methylbenzene	180-590	42		4.90
	220-590	38	10.07	
Ethylbenzene	180-615	45		4.91
	240-615	39	8.55	
Propylbenzene	175-635	47		4.14
	255-635	39	2.39	
Butylbenzene	185-660	49		4.37
	265-660	41	1.99	
Pentylbenzene	200-675	49		3.99
	290-675	40	2.01	
Hexylbenzene	215-695	49		3.56
	295-695	41	2.40	
Heptylbenzene	230-710	49		3.03
	310-710	41	4.91	
Octylbenzene	240-725	50		3.04
	320-725	42	4.46	
Nonylbenzene	250-740	50		2.99
	340-740	41	4.33	
Decylbenzene	260-750	50		2.67
	350-750	41	5.89	

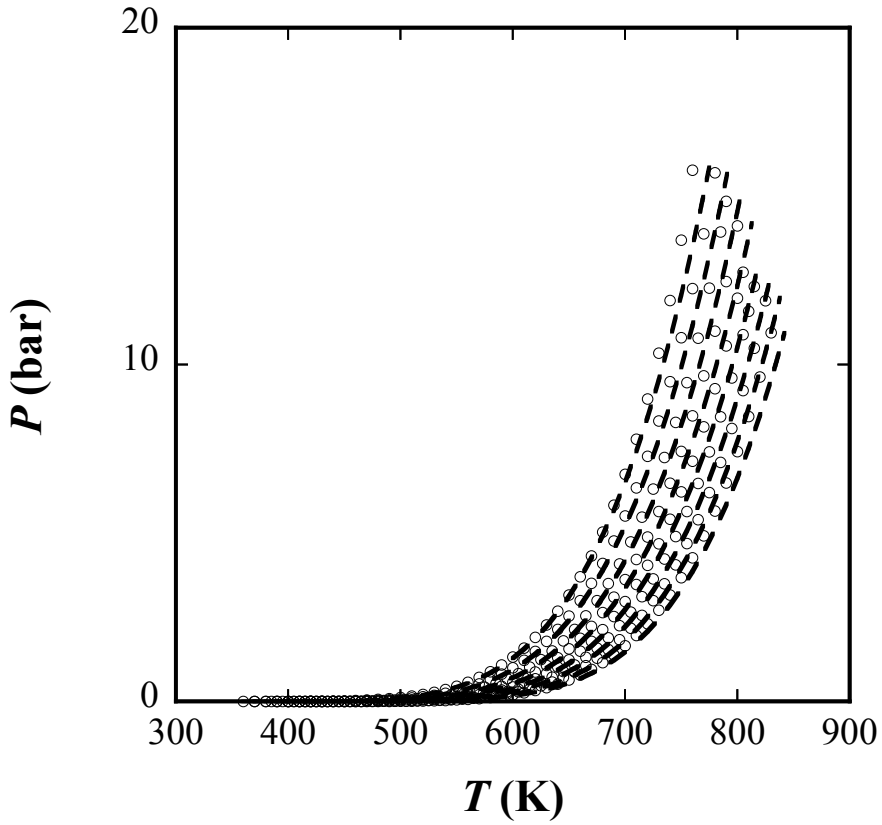

Figure 46: Comparison of GC-SAFT-VR prediction with experimental vapor pressure data for eight heavy alkylbenzenes from undecylbenzene octadecylbenzene (from left to right); experimental data [152] are represented by circles and calculated results by dashed lines.

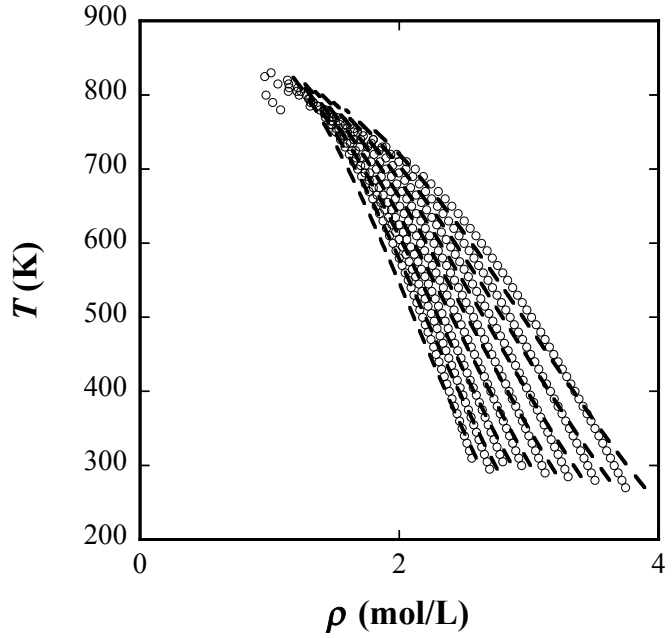

Figure 47: Comparison of GC-SAFT-VR prediction with experimental saturated liquid density data for eight heavy alkylbenzenes from undecylbenzene octadecylbenzene (from right to left); experimental data [152] are represented by circles and calculated results by dashed lines.

Table 29: The average deviation of vapor pressures and liquid densities between experimental data [152] and predicted results for pure alkylbenzenes.

Alkylbenzene	T (K)	N_{pt}	AAD *P* (%)	AAD D_{Liq} (%)
Undecylbenzene	270-760	50		2.46
	360-760	41	7.31	
Dodecylbenzene	280-780	51		2.93
	370-780	42	8.84	
Tridecylbenzene	285-790	52		3.02
	385-790	42	9.44	
Tetradecylbenzene	290-800	52		2.74
	390-800	42	12.48	
Pentadecylbenzene	300-805	52		2.17
	400-805	42	13.64	
Hexadecylbenzene	305-815	53		2.27
	405-815	43	14.36	
Heptadecylbenzene	295-825	54		2.89
	415-825	42	18.07	
Octadecylbenzene	310-830	53		3.06
	420-830	42	20.07	

5.3.2 Binary Mixtures

Having studied the phase behavior of pure fluids using the GC-SAFT-VR equation and tested the predictive capability of the approach and functional groups defined by studying the phase behavior of heavier molecules within the same chemical family, but not included in the fitting process, we now turn to binary mixtures to further test the GC-SAFT-VR approach. As in the study of pure *n*-alkanes, for binary mixtures only two types of groups (CH_3 and CH_2) are used to represent the *n*-alkane components studied, and no binary interaction parameters are used. Here we illustrate for two binary mixture systems of alkanes, one for which the chain lengths of the two alkanes are close and os the phase behavior expected to be simple and the other in which the alkanes have very different chain lengths. In Figure 48 we present results for constant pressure *Tx* slices of a simple mixture of hexane + heptane. From the phase diagram we observe good agreement between our theoretical predictions and the experimental data. We then considered a system with asymmetry in the chain lengths of the two components and studied constant temperature *Px* slices of the hexane + hexadecane phase diagram in Figure 49. We can see from the figure that good agreement is again obtained between the theoretical predictions and experimental data over the wide range of temperatures studied.

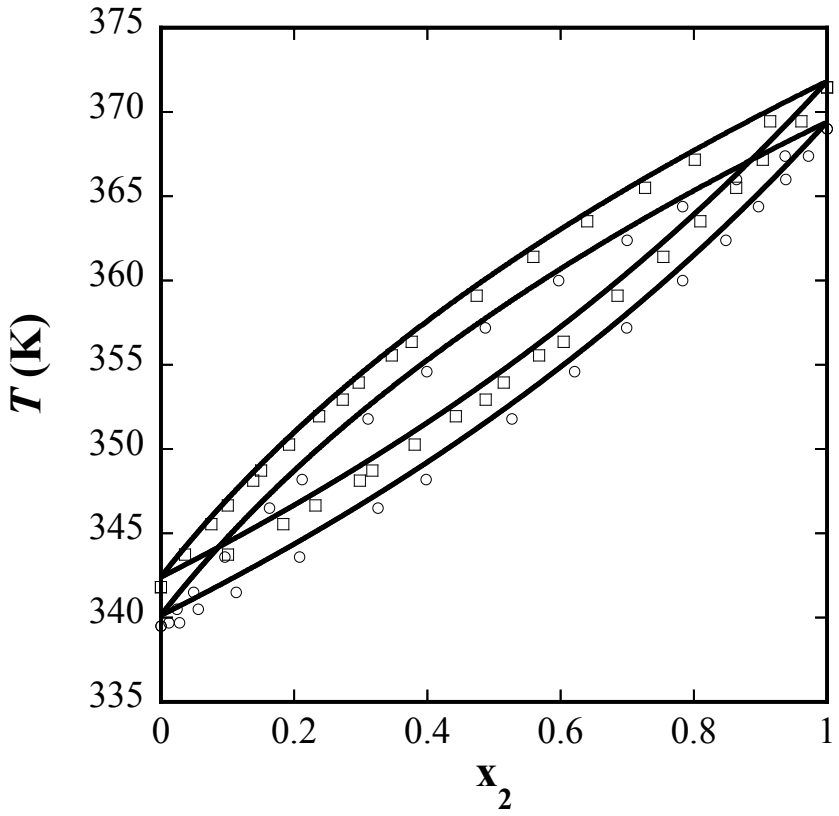

Figure 48: Predicted constant-pressure *Tx* slices of the phase diagram for hexane (1) + heptane (2) by GC-SAFT-VR, compared with experimental data [154, 155] at 0.94 bar (circle), 1.01bar (square).

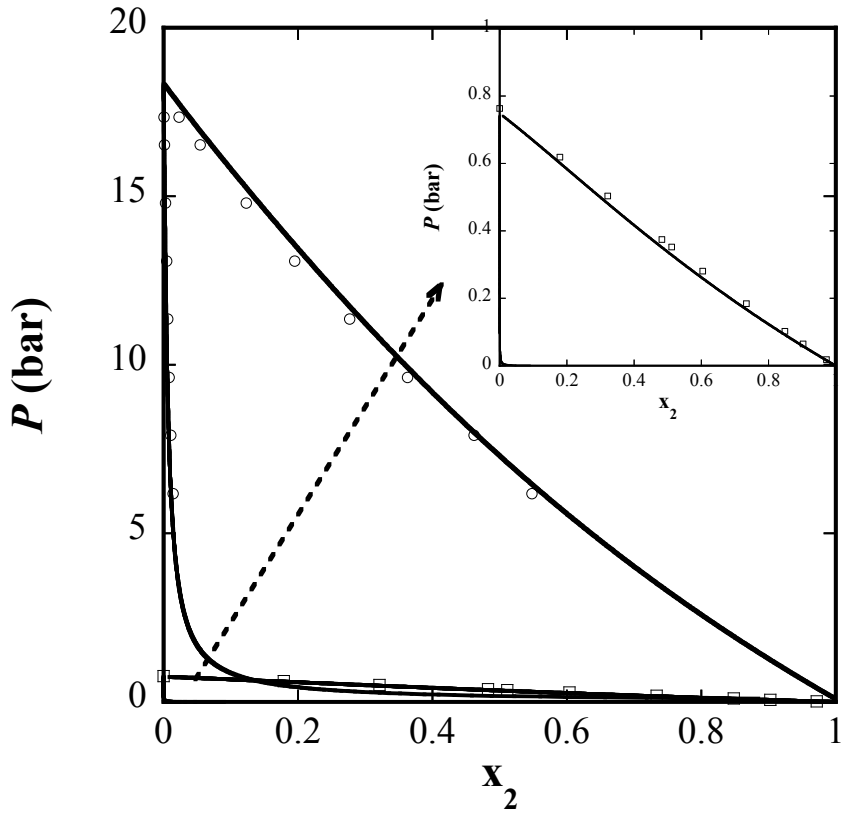

Figure 49: Predicted constant-temperature *Px* slices of the phase diagram for hexane (1) + hexadecane (2) by GC-SAFT-VR, compared with experimental data [156, 157] at 333.15K (square), 472.3K (circle).

We have also studied the vapor-liquid equilibria of four *n*-alkane + ketone binary mixtures. The results are shown in Figure 50 - Figure 53 and obtained using the fitted parameters for the interaction of the CH_3, CH_2, and C=O groups as given in Table 13 and Table 14. From Figure 50, we can see that the bubble-dew point curves at three different temperatures as well as the locations of azeotrope for binary mixture system of 3-pentanone and heptane agree very well with experimental data. In contrast, the 3-pentanone + hexane binary mixture does not display azeortopic behavior which is captured by the theory as shown in Figure 51. We also note from the figure that the GC-SAFT-VR predictions for the bubble-dew point curves are in good agreement with the

experimental data; a slight overprediction is observed close to the vapor pressure of pure hexane. We also obtained one *Px* slice for binary mixture system of 3-heptanone and hexane, its dew point curve agree very well with experimental data while the bubble point curve is slightly underpredicted as observed in Figure 52. Similar prediction of three constant termperature *Px* slices is done for the binary mixture system of longer 3-nonanone with hexane, its bubble point curves are well represented while they are slightly underpredicted when the composition of 3-nonanone increases as seen Figure 53. From Figure 50 - Figure 53, we also observe that the region between the bubble point curve and dew point curve becomes larger for heavier ketone.

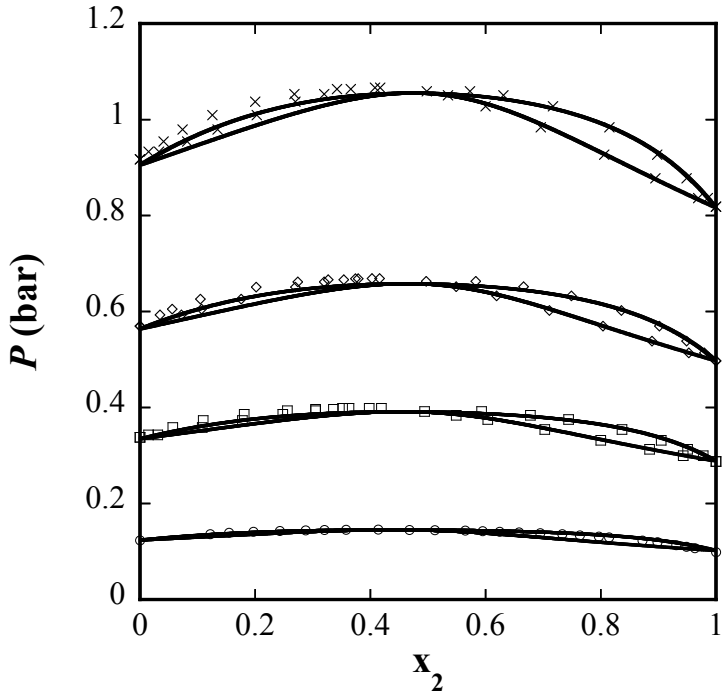

Figure 50: Predicted constant-temperature *Px* slices of the phase diagram for heptane (1) + 3-pentanone (2) by GC-SAFT-VR, compared with experimental data [158, 159] at 313.2K (circle), 338.15K (square), 353.15K (diamond), 368.15K (cross).

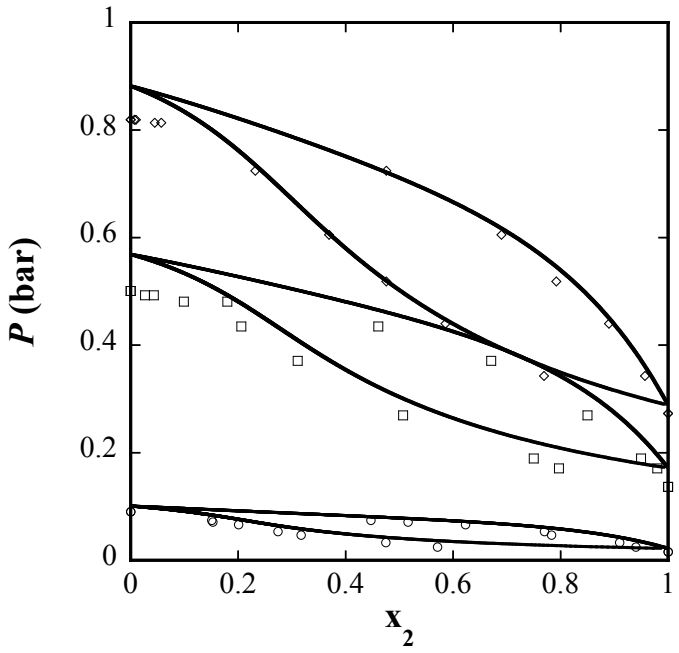

Figure 51: Predicted constant-temperature *Px* slices of the phase diagram for hexane (1) + 3-pentanone (2) by GC-SAFT-VR, compared with experimental data [160] at 283.15K (circle), 325.15K (square), 338.15K (diamond).

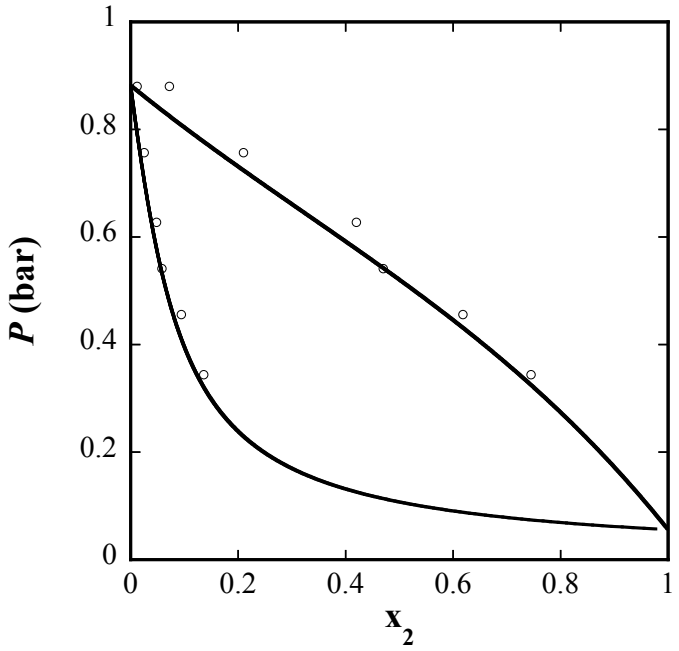

Figure 52: Predicted constant-temperature *Px* slice of the phase diagram for hexane (1) + 3-heptanone (2) by GC-SAFT-VR, compared with experimental data [161] at 338.15K (circle).

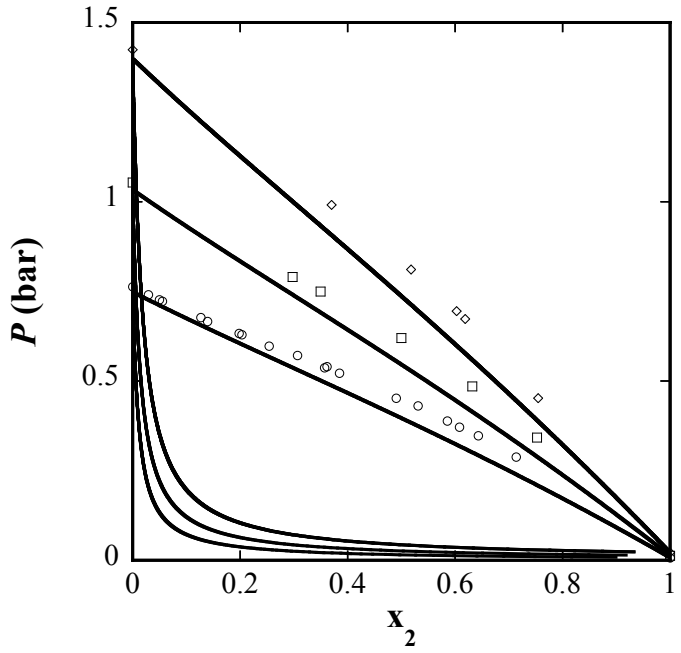

Figure 53: Predicted constant-temperature *Px* slices of the phase diagram for hexane (1) + 3-nonanone (2) by GC-SAFT-VR, compared with experimental data [162] at 333.15K (circle), 343.15K (square), 353.15K (diamond).

We also predicted the T-x phase diagrams for three selected binary mixtures of alkanes and esters and one binary mixture of esters. The predicted results for these systems are obtained by using the fitted parameters for the interaction of the CH_2, CH_3, C=O, CH_2O, and CH_3O groups as given in Table 13 and Table 14. Figure 54 and Figure 55 present the *Tx* slice for propyl butanoate with *n*-heptane (C_7H_{16}) and *n*-nonane (C_9H_{20}) at 1 bar, respectively. Though the two systems have alkanes differing in only two CH_2 groups, their phase diagrams are quite different; the propyl butanoate + nonanes systems displays an azeotrope while the mixture of propyl butanonate + heptane does not. From Figure 54 we can see that the predicted bubble and dew point curves for the propyl butanonate + heptane are in excellent agreement with the experimental data. The predicted *Tx* slice for propyl butanoate + nonane system at 1 bar agrees well with

experimental data while the azeotrope temperature is slightly underpredicted. We also studied a mixture system of methyl pentanoate + heptane (i.e., having a CH_3O group). The predicted constant pressure curves of that system are presented in Figure 56 where the bubble point and dew point curves are slightly overpredicted compared with the experimental data. In addition to mixture systems of alkane and ester, we are also interested in studying the phase properties of ester mixtures. The mixture system of methyl octanoate and methyl hexanoate has also been studied. The *Tx* diagram for this system is presented in Figure 57 and we see that the GC-SAFT-VR equation provides an excellent agreement with the experimental bubble point and dew point curves given that no parameters have been fitted to the binary mixture data and so the theoretical calculation is a pure prediction.

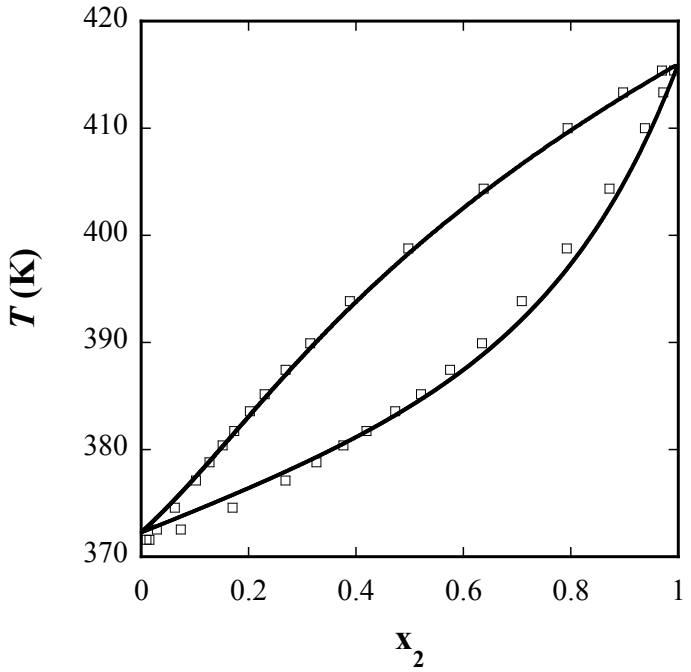

Figure 54: Predicted constant-pressure *Tx* slice of the phase diagram for heptane (1) + propyl butanoate (2) by GC-SAFT-VR, compared with experimental data [163] at 1 bar (square).

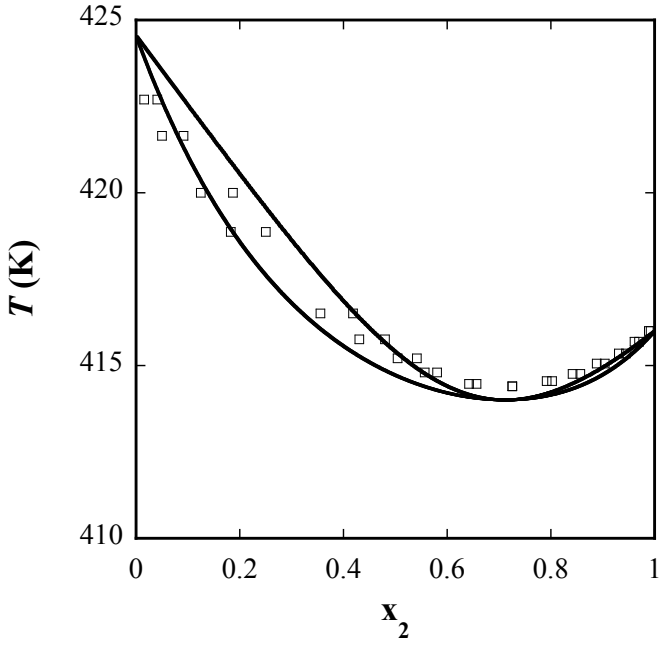

Figure 55: Predicted constant-pressure *Tx* slice of the phase diagram for nonane (1) + propyl butanoate (2) by GC-SAFT-VR, compared with experimental data [163] at 1 bar (square).

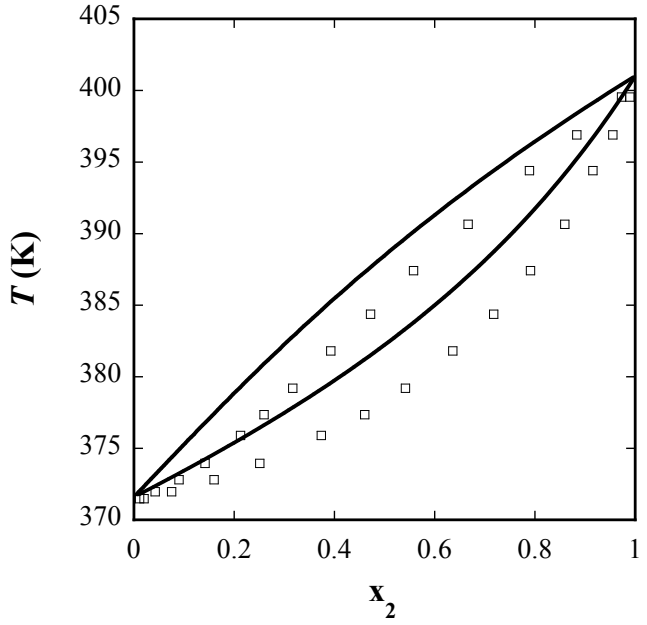

Figure 56: Predicted constant-pressure *Tx* slice of the phase diagram for heptane (1) + methyl pentanoate (2) by GC-SAFT-VR, compared with experimental data [164] at 1 bar (square).

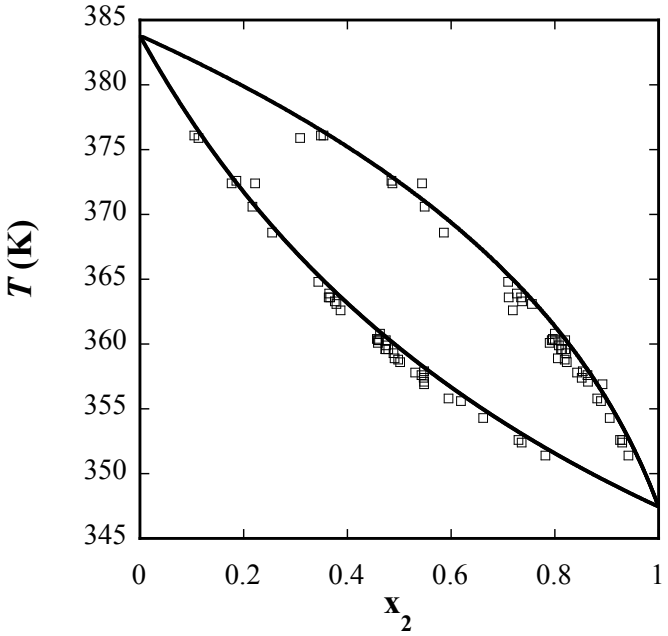

Figure 57: Predicted constant-pressure *Tx* slice of the phase diagram for methyl octanoate (1) + methyl hexanoate (2) by GC-SAFT-VR, compared with experimental data [165] at 0.0667 bar (square).

5.4 Conclusions

In this work, a group-contribution hetero-SAFT-VR approach is developed. The parameters for different key groups have been regressed from the experimental data for different chemical families. In particular, linear alkanes, branched alkanes, 1-alkenes, alkylbenzenes, ketones, and esters have been studied in this work and parameters determined for CH_3, CH_2, CH, CH_2=CH, C_6H_5, C=O, CH_2O, and CH_3O groups in order to well represent the corresponding families and hence to be extrapolated to other systems containing the same groups. The transferability of the fitted parameters for different groups is tested by predicting the phase behavior of heavier molecules. Both regression and prediction results of systems studied here are satisfactory. Hence, the group contribution type hetero-SAFT-VR is proved to be able to capture the phase behavior of fluids composed of different groups. We also applied the theory to study

some mixture systems such as binary mixture systems of alkanes, binary mixture systems of alkane and ketone, binary mixture systems of alkane and ester, and binary mixture system of esters. The theoretical prediction agrees with the experimental data very well. In the next chapter, we will use the parameter database of key functional groups to study the VLE and LLE behavior of polymer systems.

Chapter VI

APPLICATION OF GC-SAFT-VR EOS TO POLYMER SYSTEMS

6.1 Introduction

Knowledge of the phase behavior of polymer systems is very useful in the design and optimization of polymerization reactors and separators where control of the phase behavior (in order to avoid or to induce a phase transition) is essential. For example, the solubility of monomers is significant in the design of monomer devolatilization equipment in which the remaining monomer is removed from the polymer product under low pressure and high temperature conditions in order to protect the environment and eliminate the health and safety hazards related with producing and using polymers [166]. Both vapor-liquid equilibrium (VLE) and liquid-liquid phase equilibrium (LLE) are very important in polymer production, where polymers are produced in one or two phases with solvents, unreacted monomers, and additives, which must be separated [167] from the polymer product. In fact, polymer systems coexist in two liquid phases more often than systems of low molecular weight [168] and hence the LLE of polymer systems has been extensively studied.

While there is a large body of experimental data on the phase behavior (VLE and LLE) of polymer systems, experiments under high pressures and/or involving components at supercritical conditions can be difficult and expensive to perform. Hence, it is of great interest to study the thermodynamic properties of polymer systems using an efficient and robust theoretical modeling tool that can be used to extrapolate to regions of

the phase diagram where experimental measurements are not available. To this end, there are a number of thermodynamic models available in the literature to describe the phase behavior of polymer systems, such as activity coefficient models and equations of state. Traditional equations of state, such as cubic equations, usually work well for simple, nearly spherical molecules, such as small alkanes, nitrogen, and carbon monoxide, but tend to give poor predictions for polymer systems [117], since they have not been derived from a theoretical basis that accommodates for the complexities of molecular shape and interactions. Over the past decade, significant efforts have been focused on developing molecular-based EOSs to model polymers. SAFT has been successfully applied to study the thermodynamics and phase behavior of polymer systems since a polymer can be modeled as a very long flexible chain composed of tangentially bonded spherical segments, e.g., polyethylene can been treated as a very long n-alkane chain [18].

Several versions of the SAFT EOS have been developed to describe the phase behavior of polymer [6, 7, 16, 169] and copolymer systems [30, 59, 170]. In particular, Huang and Radosz proposed an engineering version of the original SAFT EOS (HR-SAFT), that has been used predominately to study polyolefin systems [171-173]. However, limited success has been seen for the HR-SAFT equation with other polymers and copolymers. More recently, Sadowski *et al*. developed a perturbed-chain SAFT (PC-SAFT) [27] to improve the description of polymer systems by using a hard-chain as the reference fluid instead of the hard-sphere reference used in HR-SAFT and shows promising results for the description of VLE and LLE of polymer mixtures [29, 169, 174, 175]. At a similar level of theory, the SAFT-VR approach has been proposed in which

chain molecules are treated as tangent hard spherical segments that interact through attractive potentials of variable range (VR), typically a square-well potential. SAFT-VR has been successfully applied to studying the adsorption of light hydrocarbons on polyethylene (PE) [6, 7] and cloud point curves of polyethylene solutions [7] using parameters for the pure polymer extrapolated from those of lighter hydrocarbons.

A major problem with modeling polymer systems is that they are often poorly characterized with respect to branching (i.e. side chains on the backbone) and heterogeneity (e.g., functional groups of different molecular composition) of polymer structure. In order to better describe the topology of polymers, e.g., copolymers which are composed of different functional groups and polymers that have side chains or pendant groups, heteronu 0clear versions of SAFT that allow the model chain to be composed of segments of different size and/or energy have been proposed by several authors [30, 59, 62, 170, 176]. In several of these heteronuclear approaches, copolymers are modeled as being composed of two distinct types of segments based on the copolymer topology and composition, the sequence of which is described in a statistical fashion through segment and bonding fractions that are estimated on the basis of the known molecular structure, e.g., the NMR-derived branch density and comonomer incorporation (i.e., mass fraction of comonomers in the copolymer composition).

One of the challenges in modeling polymer systems using the SAFT approach is determining the model parameters. In SAFT, like many equations of state, pure-component parameters are generally determined by regressing experimental vapor pressure and liquid density data. However, identifying pure-component parameters for a polymer is more difficult and is afflicted with a higher degree of uncertainty compared to

the case of volatile substances [29] since vapor-pressure data are not available. As an alternative, pure polymer EOS parameters are usually calculated by fitting to melt PVT data; however, it has been shown that SAFT parameters for the dispersion energy and segment size obtained do not work well when applied to the description of mixture phase behavior, even when large binary parameters are used [117]. Alternatively, polymer parameters can be regressed from correlations based on the parameters for smaller molecules in a homologous series. For example, this works well for polyolefins by extrapolation of n-alkane parameters to high molecular weights [6, 138]. However, it has been shown to fail when extrapolating the pure-component parameters for other types of polymers, because molecular effects such as the topology of the polymer repeat unit are not properly accounted for. Therefore, several approaches [30, 59, 62] have been proposed to obtain parameters for different types of polymer segments within a heteronuclear SAFT model in order to try to represent the heterogeneity molecular composition of the of the polymer. For example, in the copolymer-SAFT approach proposed by Banaszak *et al*., the branched copolymer is treated as being composed of two different types of segments, i.e., segments on the branch (or side chain) and segments on the backbone. In their study of poly(ethylene-co-octene-1) [74, 177], the branch (hexyl) segment parameters are taken from those for the corresponding alkane (hexane). The approach requires binary interaction parameters between each segment type on the polymer and the solvent to be fitted to polymer phase equilibrium data. However, the fitted binary parameters are temperature dependent and do not have a consistent trend as a function of temperature, hence limiting the predictive capability. Gross and coworkers proposed the poly($\alpha - co - \beta$) model [30] to study copolymers using the PC-SAFT

equation. In this approach the parameters for the comonomer segments α and β are regressed from experimental data for the corresponding homopolymer and homopolymer-solvent mixture phase equilibrium data and three binary interaction parameters describing the homopolymer-homopolymer interactions are defined and determined from homopolymer and copolymer phase equilibrium data. However, while this approach provides a more direct route to determining model parameters than copolymer-SAFT, the parameter regression becomes difficult when the corresponding homopolymer experimental data are not available, and the approach is somewhat dependent on the type of experimental data (i.e. PVT, LLE or VLE) used and the binary system chosen for parameter regression [178].

More recently, Dominik *et al*. [176] have developed a thermodynamic model to study branched polyolefins within the framework of PC-SAFT [30]. In their approach the polymer segments are also divided into two types, backbone segments and branch segments. For the backbone segments the parameters obtained by Tumakaka *et al*. for polyethylene [65] are used with a dispersion energy parameter adjusted to experimental phase behavior data for polyolefins. The binary interaction parameter between the backbone segments and solvent are also taken from Tumakaka *et al*. [65], while the binary interaction parameter between branch segments and solvent are fitted to experimental data for polyolefins. The advantage of this approach over Gross *et al*.'s work on copolymers [30] is that the number of parameters is reduced by two.

A common limitation of the above fitting methods is that the parameters are pulled together in a somewhat *ad hoc* way, which results in pure component and/or cross parameters being fitted to experimental mixture data, thus reducing the predictive ability.

In order to make the SAFT EOS a more predictive approach, parameters must be used in a transferable way and the dependence on experimental data reduced. In earlier work, we developed the hetero-SAFT-VR model in which molecules are described as chains of segments that can have different size and/or energy parameters, and hence are connected with different types of bonds [8, 64] and so allows the study of heterogeneity in molecular architecture to be captured within a SAFT model. Based on the hetero-SAFT-VR equation we have developed a group-contribution-based SAFT approach (GC-SAFT-VR) in which parameters have been determined for several key functional groups by fitting to experimental vapor pressure and saturated liquid density data for a number of of small molecules containing the functional groups of interest. The transferability of the parameters obtained for each group was tested by predicting the phase behavior of pure fluids not used in the fitting process and binary mixtures of alkanes, ketones, and esters. In all cases good agreement was obtained between the GC-SAFT-VR predictions and experimental data. In this work the parameters developed for the functional groups are used in a transferable way to study the phase behavior of polymer systems in order to investigate the suitability of the GC-SAFT-VR EOS to obtain parameters for polymers. In the following sections of this chapter, the models for polymer systems studied are described in section 6.2; the results of theoretical predictions for selected binary polymer solutions including polymers such as LDPE (Low density polyethylene), PE (polyethylene), PBD (polybutadiene), and PS (polystyrene) with a variety of polar and nonpolar solvents are presented in section 6.3; finally, the conclusions are drawn in section 6.4.

6.2 Model

In the GC-SAFT-VR approach polymers are treated as consisting of repeat units, each of which contains several types of functional groups that are connected together via different bonds according to their molecular composition and structure. For example, the simplest polymer in this study is LDPE in which CH_2 is the only functional group in the polymer repeat unit. If there are either functional groups or branches attached to the backbone as side chains, the connecting group attached is modeled as a CH group, for example since polystyrene (PS) is a homopolymer with a benzyl group attached to the hydrocarbon backbone and the repeat unit is given by,

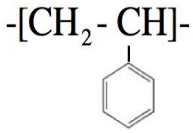

Hence the polymer repeat unit for PS in our model is composed of three types of segments; CH, CH_2, and C_6H_5.

As mentioned in the previous chapter, we have obtained parameters for the CH_3, CH_2, CH, C_6H_5, C=O, OCH_3, and OCH_2 functional groups. These regressed parameters (the segment diameter σ, well depth ε, and potential range λ) are used to describe the corresponding groups in the polymer repeat unit without any additional fitting. A detailed description of the GC-SAFT-VR EOS is provided in the Chapter V. The number of repeat units in the polymer chain is calculated based on the molecular weight of the polymer, i.e., by dividing the total molecular weight of the polymer by the molecular weight of a single repeat unit. Since the number of groups of each type within one repeat unit is also known, the total number of segments m_i for group of type i in the polymer is

obtained by multiplication of the number of repeat units, the number of groups of that type within one repeat unit, and the number of segments for a single group which has been obtained from the parameter regression for small molecules.

6.3 Results

We have applied the GC-SAFT-VR to study the phase behavior of pure fluids of small molecules and their mixtures and obtained the parameters for eight classes of functional groups in Chapter V. In this work, we extend the GC-SAFT-VR approach to study the VLE and LLE phase behavior of various binary solvent-polymer systems, using the already fitted parameters for functional groups. Although semicrystalline polymers exist as amorphous and crystalline form below its melting point, it is usually assumed that gas molecules are adsorbed in the amorphous region and do not penetrate into the crystalline region of polymer. Therefore, we have focused on studying the VLE of amorphous polymers. We first study the VLE of LDPE, which is a fairly simple polymer, in different solvents, and then study the VLE behavior of branched polyolefin, PBD and PS solutions. We have also studied the LLE behavior of LDPE solutions and PS solutions.

In Figure 58 we present the predictions for the solubility of n-pentane and 1-pentene in LDPE with a weight average molecular weight, (Mw) of 760000 g/mol at 423.65 K and 474.15 K using the GC-SAFT-VR approach. From the figure we see that experimentally more 1-pentene is absorbed than n-pentane under the same pressure and temperature, which is also predicted by the GC-SAFT-VR approach. Good agreement between the experimental data and theoretical predictions are obtained for both systems at low temperature, though we note a slight overprediction of the pressure is seen at the

higher temperature, which is above the critical temperature of both n-pentane and 1-pentene. Overall the agreement between the theoretical predictions and experimental data is very good given that no polymer data is used to obtain the model parameters and no binary interaction parameters are used. In addition to the prediction of VLE curves for mixture of LDPE and a nonpolar solvent, we also studied the VLE of mixture of LDPE and 3-pentanone ($CH_3CH_2C{=}OCH_2CH_3$). However, as with the pure fluids, when polar solvents are considered deviations are observed from the experimental data when the GC-SAFT-VR parameters are used. Therefore, in order take into account the weaker cross interactions in these systems a γ_{ij} of 0.95, defined by

$$\lambda_{ij} = \gamma_{ij} \frac{\lambda_{ii}\sigma_{ii} + \lambda_{jj}\sigma_{jj}}{\sigma_{ii} + \sigma_{jj}}$$

is used between the C=O in 3-pentanone and a CH_2 group in LDPE, which is fitted to the VLE curve for the LDPE + 3-pentanone system at 425.15 K. The predictions of VLE for the LDPE + 3-pentanone system at 425.15 K and 477.15 K are shown in Figure 59. Both vapor-pressure curves at two temperatures agree with experimental data very well.

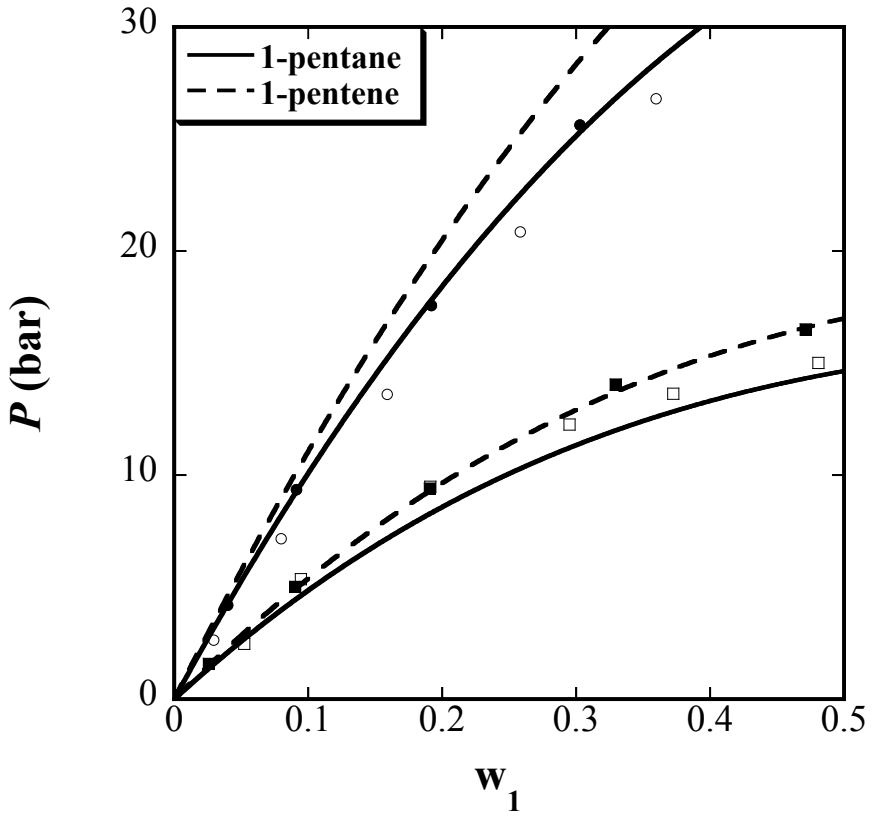

Figure 58: Constant-temperature *Pw* slices of the phase diagram for n-pentane (1) and LDPE (Mw = 760000 g/mol) and for 1-pentene (1) + LDPE (Mw = 760000 g/mol) at 423.65 K and 474.15 K. The dashed and solid lines correspond to the GC-SAFT-VR predictions for 1-pentene and pentane systems, respectively and the experimental data for n-pentane and LDPE at 423.65 and 474.15 K [179] and for 1-pentene and LDPE at 423.65 and 474.15 K [179] are represented by empty squares, empty circles, filled squares and filled circles respectively.

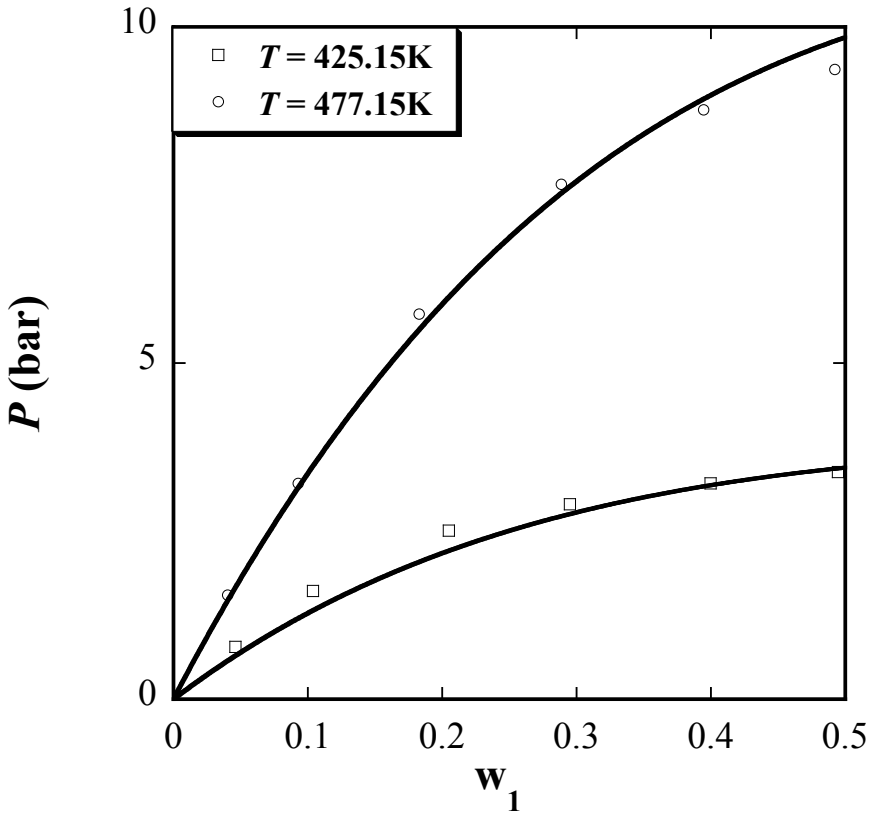

Figure 59: Constant-temperature *Pw* slices of the phase diagram for 3-pentanone (1) + LDPE (Mw = 760000 g/mol) at T = 425.15 K and 477.15 K. The solid lines correspond to the GC-SAFT-VR predictions. Experimental data at 425.15 K and 477.15 K [179] are represented by squares and circles respectively.

We also studied the effect of molecular weight on the VLE phase behavior of PE in toluene, which is a commonly used solvent. The curves predicted for PE system with a higher molecular weight (the number average molecular weight, Mn = 6220 g/mol) gives higher weight fraction of toluene than for PE system with a lower weight (Mn = 1710 g/mol) at the same temperature and pressure. This is also consistent with the experimental data as shown in Figure 60. Theoretical prediction gives very good results below the pressure of 0.8 bar compared with the experimental data. No binary interaction parameter is applied to the GC-SAFT-VR parameters in this system.

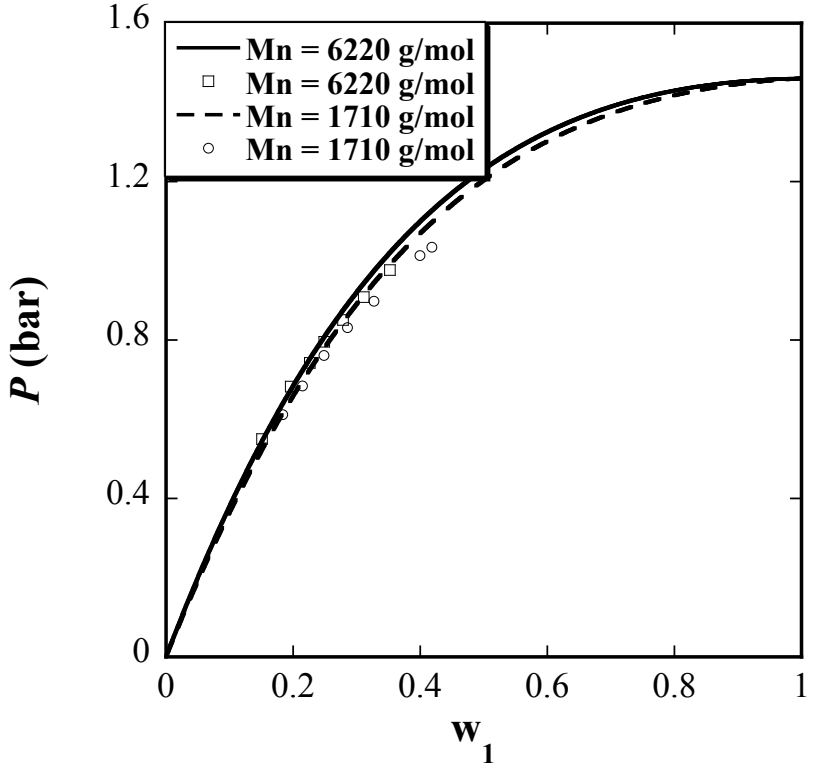

Figure 60: Constant-temperature *Pw* slices of the phase diagram for toluene (1) + PE (Mn = 6220 g/mol) and for toluene (1) + PE (Mn = 1710 g/mol) at T = 393.15 K. The lines correspond to the GC-SAFT-VR predictions. Experimental data at 393.15 K [180] are represented by squares and circles.

In addition to studying effect of polymer molecular weight on the phase behavior we also studied the effect of branching (or side chains) in polyolefins. Figure 61 presents the experimental weight fractions of toluene in polydecene-1 and polyheptene-1 at 303.15 K, compared with the model predictions obtained by the GC-SAFT EOS. Although polydecene-1 (Mn = 213900 g/mol) and polyheptene-1 1 (Mn = 224100 g/mol) have similar molecular weights they differ in structure, as illustrated in Figure 62. The predicted curve for the polydecene-1 with long branches is above that for polyheptene-1 with short branches, which is in agreement with the experimental data. However, we can

see that the branching effect on the VLE of branched polyolefin of high molecular weight in toluene is insignificant from both the model predictions and experimental data. As seen from the figure, theoretical prediction of the pressure curves obtained without applying any binary parameter are in good agreement with the experimental data at low pressures. However, the adsorption of toluene in polydecene-1 or polyheptene-1 at the same pressure is underpredicted when the weight fraction of toluene is above 0.4.

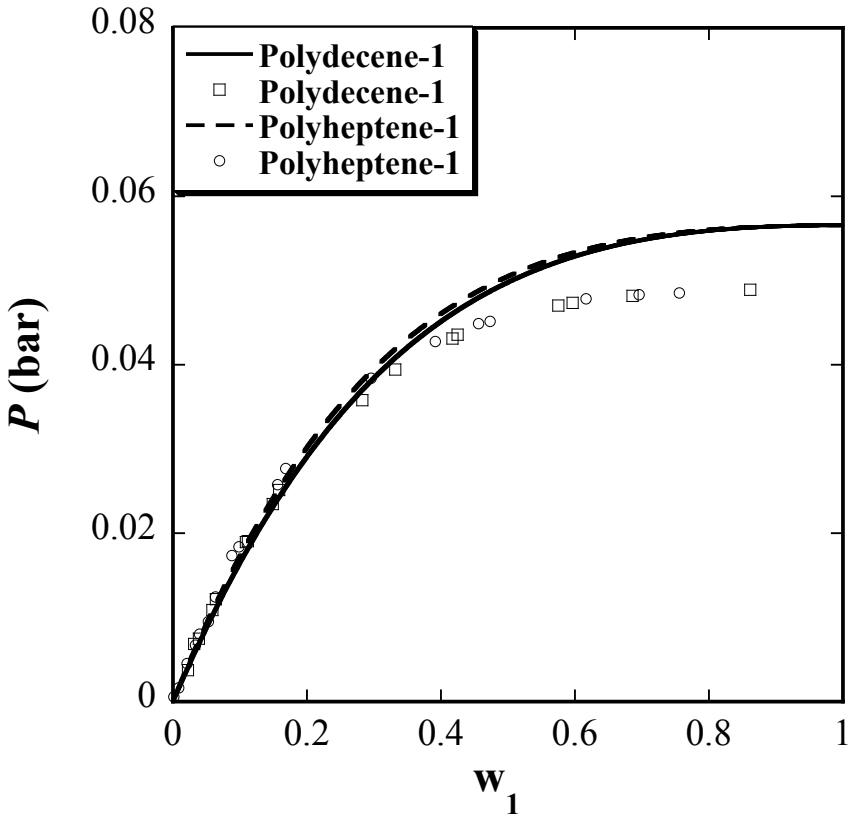

Figure 61: Constant-temperature *Pw* slices of the phase diagram for toluene (1) + polydecene-1 (Mn = 213900 g/mol) and for toluene (1) + polyheptene-1 (Mn = 224100 g/mol) at T = 303.15 K. The lines correspond to the GC-SAFT-VR predictions. Experimental data at 303.15 K [180] are represented by symbols.

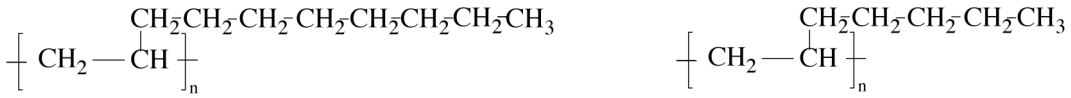

(a) (b)

Figure 62: Repeat unit structure of a) poly(decene-1) and b) poly(heptene-1) (from left to right).

In contrast to the linear polyolefins studied, PBD has a linear backbone structure $(CH=CH\text{-}CH_2\text{-}CH_2)_n$ that is composed of two different segments CH=CH and CH_2. The VLE behavior of solution of PBD (Mw = 250000 g/mol) and ethyl benzene at 353.15 K, 373.15 K, and 403.15 K is illustrated in Figure 63. As the temperature increases, less ethyl benzene is dissolved in the PBD solution under the same pressure, which is accurately captured by the theory. Although the theory underpredicts the vapor pressure for the low-temperature curve of PBD in ethyl benzene, we note that the agreement is good given that no polymer experimental data is used to determine the model parameters or binary interaction parameter is used.

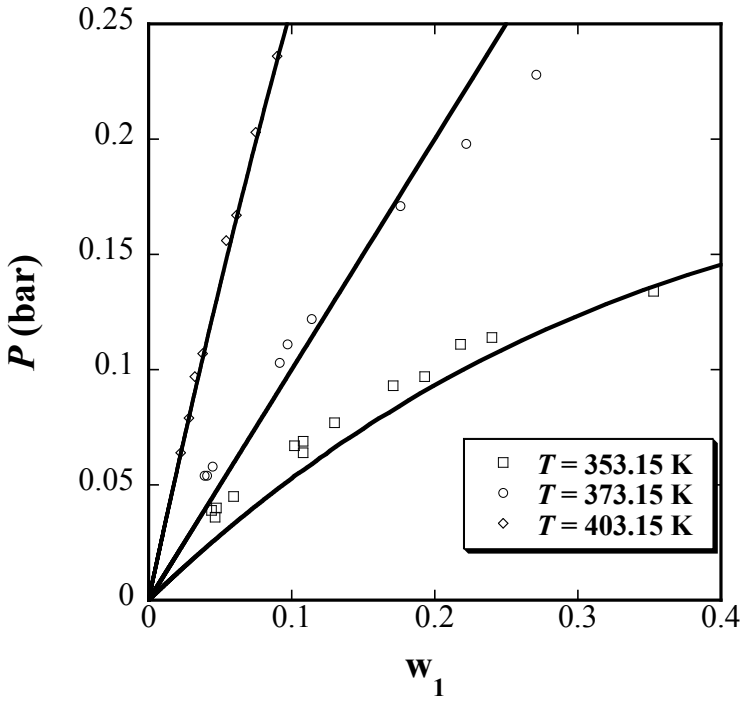

Figure 63: Constant-temperature *Pw* slices of the phase diagram for ethylbenzene (1) + PBD (Mw = 250000 g/mol) at T = 353.15, 373.15, and 403.15 K. The lines correspond to the GC-SAFT-VR predictions. Experimental data at T = 353.15, 373.15, and 403.15 K [181] are represented by squares, circles, and diamonds respectively.

Having studied the VLE behavior of some linear and branched polyolefin solutions, we are interested in studying the heteronuclear polymer with other pedant group. We examine the VLE phase behavior of mixtures of polystyrene (PS) having benzyl functional group as pendant to the backbone as illustrated in Figure 64 - Figure 67. The results obtained with the GC-SAFT-VR EOS for the nonane – PS binary mixture for a polymer sample with Mn = 53700 g/mol at 403.15 K, 423.15 K, and 448.15 K are presented in Figure 64. From the figure we can see that the model predicts the VLE behavior of this system accurately as a function of temperature, again without the use of any polymer experimental data or binary parameters fitted to the nonane-PS system. In Figure 65, we present the theoretical prediction for the VLE of the toluene - PS system

(Mn = 290000 g/mol) at 298.15 K and 333.15 K. Again, excellent agreement between the theoretical results and experimental data is achieved without using binary interaction parameters.

Having studied the VLE of PS in nonpolar solvents, we now apply the GC-SAFT-VR EOS to investigate the VLE behavior of PS in polar solvents such as ketones and esters. The results from VLE calculations for the 3-pentanone - PS (Mn = 200000 g/mol) system at 293.15 K are presented in Figure 66. Again, in order take into account the weaker cross polar interactions a γ_{ij} of 0.95 is used for the interaction between the C=O in pentanone and the CH_2 in the polymer. Additionally a γ_{ij} of 0.976 to used between the C=O in pentanone and C_6H_5 in PS. Using these parameters good agreement between the predicted results and experimental data is obtained. Furthermore, we studied a mixture of PS (Mn =290000 g/mol) and propyl acetate ($CH_3C{=}OOCH_2CH_2CH_3$). The VLE results are calculated at 298.15 K and 343.15 K as shown in Figure 67 again using a γ_{ij} of 0.95 between the C=O group in the acetate and the CH_2 group in the polymer and a γ_{ij} of 0.976 between C=O in the acetate and C_6H_5 in PS. From the figure, we can see that while the theory provides a good description of the experimental data in the low weight fraction region, deviations are observed at high weight fractions. However, we note that this deviation of the pressure curve of PS in propyl acetate might result from the deviation between the correlated vapor pressure and the experimental data of pure propyl acetate.

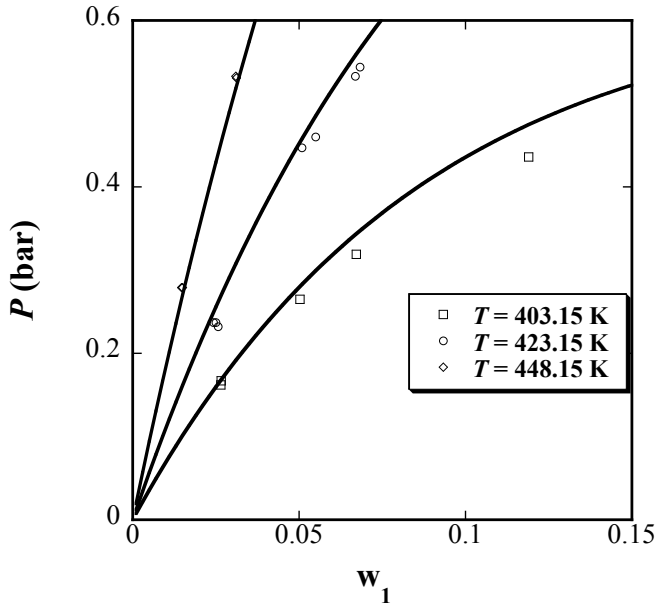

Figure 64: Constant-temperature *Pw* slices of the phase diagram for nonane (1) + PS (Mn = 53700 g/mol) at T = 403.15, 423.15, 448.15 K. The lines correspond to the GC-SAFT-VR predictions. Experimental data at T = 403.15, 423.15, 448.15 K [181] are represented by squares, circles, and diamonds respectively.

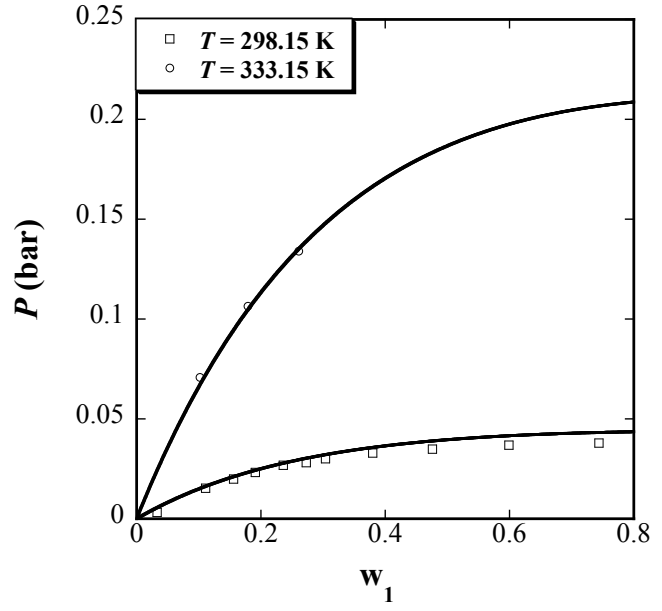

Figure 65: Constant-temperature *Pw* slices of the phase diagram for toluene (1) + polystyrene (Mn = 290000 g/mol) at T = 298.15 and 333.15 K. The lines correspond to the GC-SAFT-VR predictions. Experimental data at T = 298.15 and 333.15 K [181] are represented by squares and circles respectively.

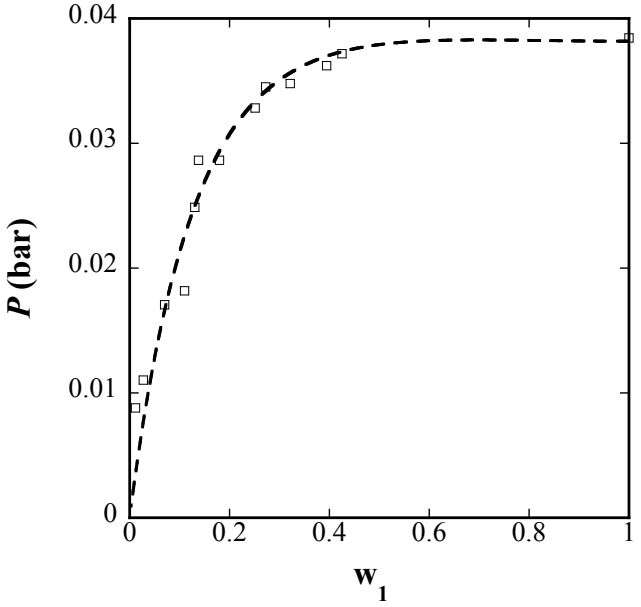

Figure 66: Constant-temperature *Pw* slice of the phase diagram for 3-pentanone (1) + polystyrene (Mn = 200000 g/mol) at T = 293.15 K. The dashed line corresponds to the GC-SAFT-VR prediction. Experimental data at T = 293.15 K [181] are represented by squares.

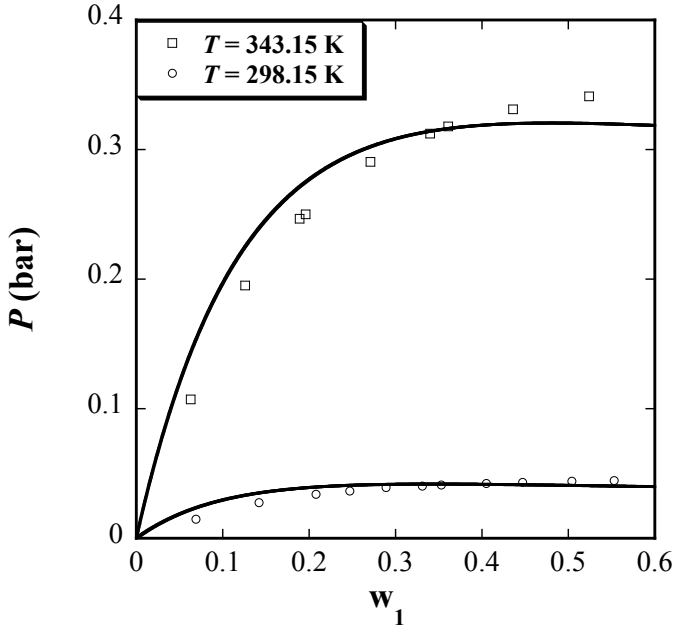

Figure 67: Constant-temperature *Pw* slices of the phase diagram for propyl acetate (1) + polystyrene (Mn = 290000 g/mol) at T = 298.15 and 343.15 K. The lines correspond to the GC-SAFT-VR predictions. Experimental data at T = 298.15 and 343.15 K [181] are represented by circles and squares respectively.

Being able to model the VLE phase behavior of polymers in nonpolar solvents successfully and polymer in polar solvents satisfactorily as illustrated before, the performance of the GC-SAFT-VR EOS also is further tested by studying binary polymer-solvent mixtures exhibiting liquid-liquid phase behavior. Here we used the approach of Paricaud *et al.* [182] to find the coexistence (binodal) composition of the two liquid phases in which the spinodal compositions are obtained as a starting point for finding the binodals. The GC-SAFT-VR EOS was tested on the liquid-liquid equilibria (LLE) behavior of several polymer-solvent systems including PE and PS. Figure 68 shows a comparison of the demixing pressures at 460 K for PE (Mw = 108000 g/mol) solutions with n-butane and n-pentane. The region above each curve corresponds to the one-phase region for each system. Both systems exhibit upper critical solution pressure (UCSP) behavior. We find that while the GC-SAFT-VR approach gives the correct trend it underpredicts the experimental results if no binary parameters fitted to the LLE data are used. If a cross interaction parameter of $\gamma_{ij} = 0.994$ is used between CH_2 and CH_3 in different molecules good agreement with the experimental data is observed as shown in Figure 68.

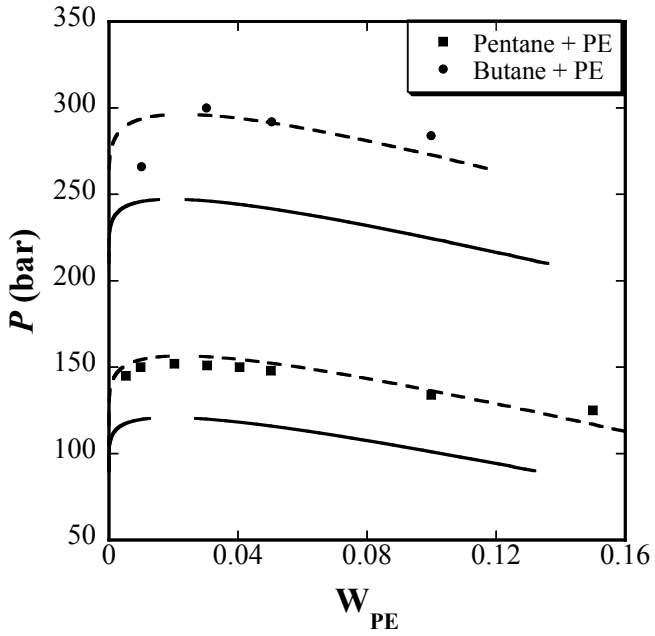

Figure 68: Constant-temperature *Pw* slices of the phase diagram for pentane + PE (108000 g/mol) and for butane + PE (108000 g/mol) at T = 460 K. The dashed lines are calculated by the GC-SAFT-VR predictions using $\gamma_{ij} = 0.994$ between CH_2 and CH_3 and solid lines calculated without using γ_{ij}. Experimental data for pentane systems and butane systems at T = 460 K [183] are represented by squares and dots respectively.

We have also compared the demixing curves for solvent-PE with different molecular weights. Figure 69 presents the temperature-composition curve for PE (Mw = 108000 g/mol) in butane at 300 bar and the temperature-composition curve for PE (Mw = 16400 g/mol) in pentane at 100 bar. The region below each curve corresponds to the one-phase region for each system. The model predicts the lower critical solution temperature (LCST) behavior satisfactorily keeping an interaction parameter of $\gamma_{ij} = 0.994$ between CH_2 and CH_3 in different molecules as used in Figure 68.

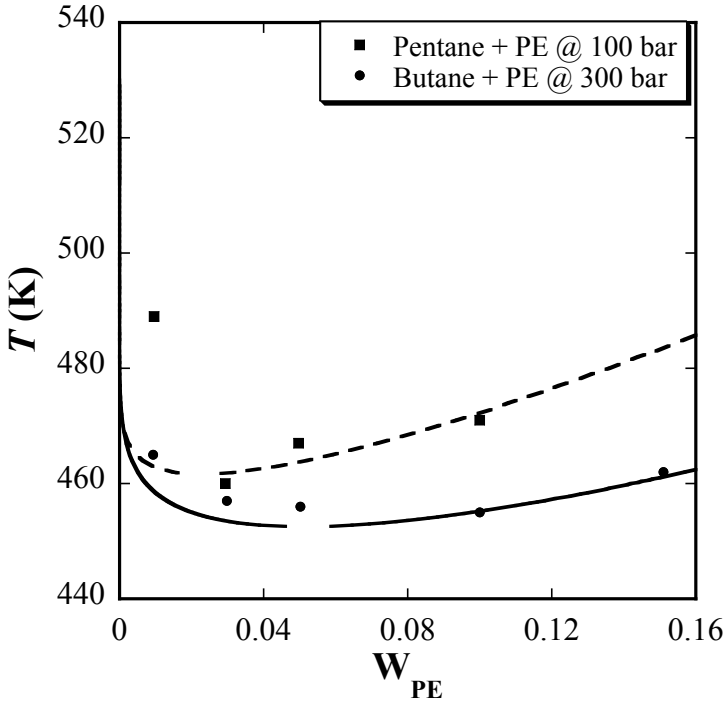

Figure 69: Constant-pressure *Tw* slices of the phase diagram for pentane + PE (Mw = 16400 g/mol) at P = 100 bar and for butane + PE (Mw = 108000 g/mol) at P = 300 bar. The lines correspond to prediction from the GC-SAFT-VR EOS. Experimental data for pentane systems at P = 100 bar [184] and for butane systems at P = 300 bar [183] are represented by squares and dots respectively.

After studying LLE behavior of PE solutions, we examined the LLE behavior of PS in propyl acetate solution. The interactions among the aromatic and hydrocarbon groups in PS and carbonyl group in propyl acetate are very complicated, which was seen when we studied the VLE behavior of PS in propyl acetate. Here we use the same binary cross interaction parameters between C=O and CH_2 and between C=O and C_6H_5 as for the VLE properties of PS in propyl acetate along with the γ_{ij} of 0.994 between cross CH_2 and CH_3 groups. Using this approach, the predicted LCST curve displays a much narrower phase envelope compared with the experimental data as shown in Figure 70.

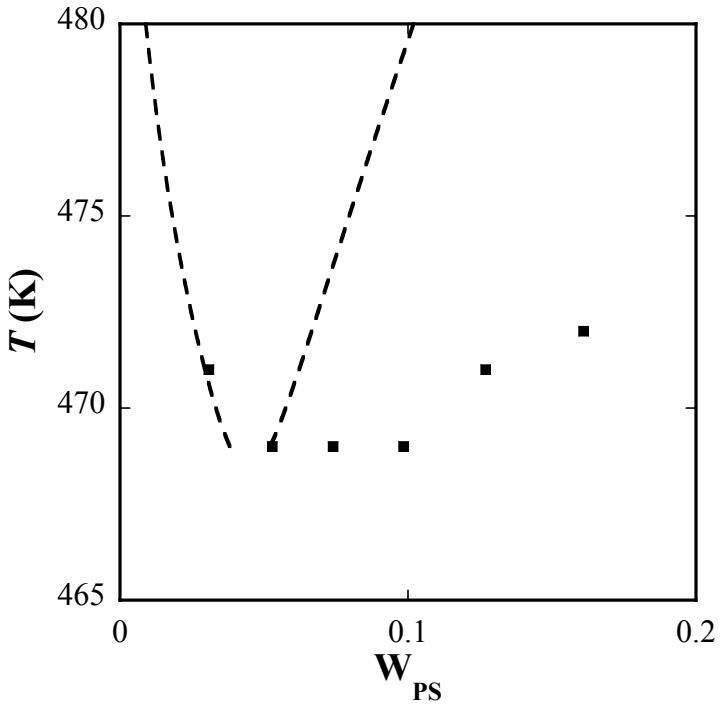

Figure 70: Constant-pressure *Tw* slice of the phase diagram for propyl acetate + PS (110000 g/mol) at P = 1 bar. The dashed line corresponds to prediction from the GC-SAFT-VR EOS. Experimental data at P = 1 bar [185] are represented by squares.

6.4 Conclusions

In this work, GC-SAFT-VR equation is applied to study both the VLE and LLE phase behavior of polymer systems. The parameters for the functional groups in the polymer repeat units were obtained from the regression of experimental vapor pressure and saturated liquid density data for pure fluids. The heterogeneity in the polymer structure (e.g., branching and functional groups) is explicitly described in the GC-SAFT-VR EOS. In general, the GC-SAFT-VR EOS gives good predictions of the VLE behavior of polymer solutions with parameters regressed from the experimental data of pure components only. The effects of polymer molecular weight and branching on the VLE behavior of polymer solutions are captured by the GC-SAFT-VR EOS. However, the LLE behavior of polymer solutions is more difficult to predict, thus resulting in the use of

binary interaction parameters to overcome the overprediction or underprediction of the experimental data. Furthermore, a transferrable γ_{ij} is often applied to effectively take into account the dipolar interactions when studying the phase behavior of systems with polymer and/or solvent containing C=O group with other groups including the hydrocarbon groups and aromatic group. Recently, Zhao *et al.* [57] has developed a SAFT-VR+D equation to study dipolar chain fluids using the dipolar square well fluid as the reference state. This approach can explicitly take into account the magnitude and orientation of the dipole moment which have been found to affect the thermodynamics and phase behavior of dipolar square well monomer and chain fluids. Therefore, the use of binary parameter might be eliminated, if the polarity of dipolar functional group C=O in our GC-SAFT-VR model is explicitly treated by combining the SAFT-VR+D scheme.

CHAPTER VII

CONCLUSIONS

Understanding the fluid phase behavior of chemical systems is of great practical importance in the design of industrial chemical process and equipment. A reliable and accurate modeling tool for the calculation and prediction of the phase behavior of chemical systems over the wide range of operating conditions encountered would be of great value in industrial practice. Among the many versions of EOSs, a lot of attention has been focused on developing molecular-based approaches. In this work, we focus on developing a molecular-based hetero-SAFT-VR approach and investigating its applications in the fluid systems of low molecular weight as well as polymer systems and addressing the effects of molecular heterogeneity on the phase behavior of these systems. Our work extends the original SAFT-VR EOS which is a homonuclear-based model to a heteronuclear approach in which the chain fluids are treated as being composed of segments of different size and/or energy of interaction, so that the effects of heterogeneity in terms of molecular structure and composition on the thermodynamic properties can be captured explicitly and quantatively. Furthermore, by capitalizing on the flexibility of the hetero-SAFT-VR approach, we have implemented the concept of group contribution into the hetero-SAFT-VR approach and developed the GC-SAFT-VR EOS. Parameters for key functional groups have been determined and demonstrated to be transferable from the pure component to mixture of small molecules, and polymer solutions.

In Chapter III, the hetero-SAFT-VR approach has been validated by comparing with both *NPT* MC and GEMC simulations which are performed for symmetric and asymmetric diblock chain fluid systems. The phase behavior of diblock fluids is also found to be influenced by the interaction energies, segment sizes, and the segment arrangement in terms of symmetry. Excellent agreement is obtained between the theoretical predictions and simulation data, hence validating the use of the SAFT-VR approach for heteronuclear chains in more realistic models of polymers and small molecules composed of different functional groups.

In Chapter IV, we have studied the effect of tether groups on the thermodynamic properties and phase behavior of POSS fluids through both molecular simulation and the hetero-SAFT-VR EOS. The POSS cage is represented by a single sphere and the tether groups by one or more smaller spheres, depending on chain length in the hetero-SAFT-VR approach, Since very limited experimental data is available for the thermodynamic properties of POSS systems, the molecular dynamics simulations are carried out to obtain pseudo-experimental *PVT* data at constant temperature with which to regress the SAFT parameters for POSS molecules and also to validate the theoretical approach. The effects of tether length and the number of tethers on the phase behavior (PVT and VLE) of POSS systems have been investigated by using the hetero-SAFT-VR approach. Good agreement is obtained between the simulation data and the theoretical results and predictions are made for systems yet to be studied by simulation or experiment.

In Chapter V, we have developed the GC-SAFT-VR EOS based on the hetero-SAFT-VR approach and regressed the parameters for key functional groups to experimental vapor pressure and saturated liquid density data of selected classes of

compounds including alkanes, 1-alkenes, alkyl benzenes, ketones, and esters. The transferability of the fitted parameters has been tested by comparing the theoretical prediction of phase behavior with experimental data of pure fluids not included in the fitting process, and also binary mixtures of alkanes, of alkane and ketone, and of alkane and ester. Good agreement is obtained between the experimental data and theoretical predictions. Using the GC-SAFT-VR we are able to capture the effects of heterogeneity in molecular architecture by defining different representative groups in terms of different size/energy parameters. This allows a quantitative description of the effects of molecular structure and molecular composition (i.e. number and type of different functional groups) on the thermodynamic properties.

In Chapter VI, the GC-SAFT-VR EOS has been applied to model polymer systems by explicitly addressing the effects of molecular topology (e.g., the composition of repeat unit or branching) on polymer solution phase behavior. The parameters for each functional group in the polymer repeat unit have been obtained by regressing to experimental vapor pressure and saturated liquid density data for small molecules in Chapter V. Having tested the transferability of the fitted parameters for small molecule systems, the parameters were then used to study the VLE behavior of different polymers (e.g., PE, PS, PDB) in nonploar (e.g., alkanes, toluene) and polar solvents (e.g., ketones, esters). Generally, good agreement between the theoretical predictions and experimental data is achieved. The GC-SAFT-VR model has also been used to study the liquid-liquid equilibrium of polymer solutions. However, it is found that the LLE properties of polymer solutions are more sensitive to the functional group energy parameters, than the VLE properties of polymer solutions. We also found that in study of both VLE and LLE

behavior of polymer solutions, systems containing C=O group with strong polar interaction require a binary parameter between C=O and other groups (CH_2 or C_6H_5) to be fitted.

In future work to enhance the GC-SAFT-VR approach for studying polar systems, polar interactions could be explicitly taken into account by implementing the SAFT-VR+D approach to the GC-SAFT-VR equation. This may eliminate the need for a binary interaction parameter between CH_2 (or C_6H_5) group and C=O group. Once the dipole interaction is explicitly accounted for in the GC-SAFT-VR approach, we can explore the phase behavior of more complex polymer systems with strong dipole moments. For example, there has been increasing interest in the development of copolymers soluble in supercritical CO_2 that are composed of only carbon, hydrogen, and oxygen such as the carbonyl group [131, 186, 187]. It was found experimentally that PVAc is more soluble in supercritical CO_2 (sCO_2) than PMA [131], even though a repeat group in PMA has the same number of carbon, hydrogen, and oxygen atoms as PVAc. In order to investigate the cause of their different phase behaviors, the dipolar interactions caused by C=O group in these polymers should explicitly be accounted for through extending GC-SAFT-VR approach for polar fluids.

Additionally, in the current work, we only focus on the binary mixture systems for which the algorithm for the liquid-liquid calculation is simple. However, many polymer solutions contain more than two components and so it would be very useful to develop an efficient numerical algorithm to calculate the LLE for multi-component polymer solutions.

Since the corners of POSS cube can functionalized with different functional groups, the hetero-SAFT-VR approach could be broadly applied to a wide range of systems. An additional interesting application area would be to combine the work presented on POSS with the GC-SAFT-VR approach. It would be very interesting to study the effects of these functional groups on the thermodynamic properties of POSS systems using the GC-SAFT-VR approach. Furthermore, POSS has been used as additives to polymeric materials to improve the polymer properties and hence the GC-SAFT-VR approach could be applied to study the adsorption of POSS molecules in polymers. One major drawback to this approach currently is the lack of experimental data for validation of the cross interactions (i.e., POSS-solvent or POSS-polymer). Additional experimental work in this area would be needed to pursue this area of research.

REFERENCES

1 Agrawal, R., "Separations: Perspective of a process developer/designer," AIChE Journal, 47, 967-971 (2001).

2 Chapman, W.G., K.E. Gubbins, G. Jackson and M. Radosz, "Saft - Equation-of-State Solution Model For Associating Fluids," Fluid Phase Equilibria, 52, 31-38 (1989).

3 Song, Y.H., S.M. Lambert and J.M. Prausnitz, "Equation Of State For Mixtures Of Hard-Sphere Chains Including Copolymers," Macromolecules, 27, 441-448 (1994).

4 Gil Villegas, A., A. Galindo, P.J. Whitehead, S.J. Mills, G. Jackson and A.N. Burgess, "Statistical associating fluid theory for chain molecules with attractive potentials of variable range," Journal of Chemical Physics, 106, 4168-4186 (1997).

5 Galindo, A., L.A. Davies, A. Gil-Villegas and G. Jackson, "The thermodynamics of mixtures and the corresponding mixing rules in the SAFT-VR approach for potentials of variable range," Molecular Physics, 93, 241-252 (1998).

6 McCabe, C., A. Galindo, M.N. Garcia-Lisbona and G. Jackson, "Examining the adsorption (vapor-liquid equilibria) of short- chain hydrocarbons in low-density polyethylene with the SAFT-VR approach," Industrial & Engineering Chemistry Research, 40, 3835-3842 (2001).

7 Paricaud, P., A. Galindo and G. Jackson, "Modeling the cloud curves and the solubility of gases in amorphous and semicrystalline polyethylene with the SAFT-VR approach and flory theory of crystallization," Industrial & Engineering Chemistry Research, 43, 6871-6889 (2004).

8 Peng, Y., H.G. Zhao and C. McCabe, "On the thermodynamics of diblock chain fluids from simulation and heteronuclear statistical associating fluid theory for potentials of variable range," Molecular Physics, 104, 571-586 (2006).

9 Peng, Y. and C. McCabe, "Molecular simulation and theoretical modeling of polyhedral oligomeric silsesquioxanes," Molecular Physics, 105, 261-272 (2007).

10 Peng, Y. and C. McCabe, "Developing a Group Contribution based hetero-SAFT-VR Equation of State," in preparation (2007).

11 Peng, Y. and C. McCabe, "Modeling Phase Equilibrium of Polymer Systems with the GC-SAFT-VR Approach," in preparation (2007).

12 Wertheim, M.S., "Fluids with Highly Directional Attractive Forces.1. Statistical Thermodynamics," Journal of Statistical Physics, 35, 19-34 (1984).

13 Wertheim, M.S., "Fluids with Highly Directional Attractive Forces.2. Thermodynamic Perturbation-Theory and Integral-Equations," Journal of Statistical Physics, 35, 35-47 (1984).

14 Wertheim, M.S., "Fluids with Highly Directional Attractive Forces.3. Multiple Attraction Sites," Journal of Statistical Physics, 42, 459-476 (1986).

15 Wertheim, M.S., "Fluids with Highly Directional Attractive Forces.4. Equilibrium Polymerization," Journal of Statistical Physics, 42, 477-492 (1986).

16 Huang, S.H. and M. Radosz, "Equation Of State For Small, Large, Polydisperse, And Associating Molecules," Industrial & Engineering Chemistry Research, 29, 2284-2294 (1990).

17 Huang, S.H. and M. Radosz, "Equation of State For Small, Large, Polydisperse, and Associating Molecules - Extension to Fluid Mixtures," Industrial & Engineering Chemistry Research, 30, 1994-2005 (1991).

18 Muller, E.A. and K.E. Gubbins, "Molecular-based equations of state for associating fluids: A review of SAFT and related approaches," Industrial & Engineering Chemistry Research, 40, 2193-2211 (2001).

19 Jackson, G., W.G. Chapman and K.E. Gubbins, "Phase-Equilibria of Associating Fluids - Spherical Molecules With Multiple Bonding Sites," Molecular Physics, 65, 1-31 (1988).

20 Galindo, A., P.J. Whitehead, G. Jackson and A.N. Burgess, "Predicting the high-pressure phase equilibria of water plus n- alkanes using a simplified SAFT theory with transferable intermolecular interaction parameters," Journal of Physical Chemistry, 100, 6781-6792 (1996).

21 Galindo, A., P.J. Whitehead, G. Jackson and A.N. Burgess, "Predicting the phase equilibria of mixtures of hydrogen fluoride with water, difluoromethane (HFC-32), and 1,1,1,2- tetrafluoroethane (HFC-134a) using a simplified SAFT approach," Journal of Physical Chemistry B, 101, 2082-2091 (1997).

22 Garcia Lisbona, M.N., A. Galindo, G. Jackson and A.N. Burgess, "Predicting the high-pressure phase equilibria of binary aqueous solutions of 1-butanol, n-butoxyethanol and n- decylpentaoxyethylene ether (C10E5) using the SAFT-HS approach," Molecular Physics, 93, 57-71 (1998).

23 Garcia Lisbona, M.N., A. Galindo, G. Jackson and A.N. Burgess, "An examination of the cloud curves of liquid-liquid immiscibility in aqueous

solutions of alkyl polyoxyethylene surfactants using the SAFT-HS approach with transferable parameters," Journal of the American Chemical Society, 120, 4191-4199 (1998).

24 Blas, F.J. and L.F. Vega, "Prediction of binary and ternary diagrams using the statistical associating fluid theory (SAFT) equation of state," Industrial & Engineering Chemistry Research, 37, 660-674 (1998).

25 Blas, F.J. and L.F. Vega, "Critical behavior and partial miscibility phenomena in binary mixtures of hydrocarbons by the statistical associating fluid theory," Journal of Chemical Physics, 109, 7405-7413 (1998).

26 Dias, A.M.A., H. Carrier, J.L. Daridon, J.C. Pamies, L.F. Vega, J.A.P. Coutinho and I.M. Marrucho, "Vapor-liquid equilibrium of carbon dioxide-perfluoroalkane mixtures: Experimental data and SAFT modeling," Industrial & Engineering Chemistry Research, 45, 2341-2350 (2006).

27 Gross, J. and G. Sadowski, "Perturbed-chain SAFT: An equation of state based on a perturbation theory for chain molecules," Industrial & Engineering Chemistry Research, 40, 1244-1260 (2001).

28 Tumakaka, F. and G. Sadowski, "Application of the Perturbed-Chain SAFT equation of state to polar systems," Fluid Phase Equilibria, 217, 233-239 (2004).

29 Gross, J. and G. Sadowski, "Modeling polymer systems using the perturbed-chain statistical associating fluid theory equation of state," Industrial & Engineering Chemistry Research, 41, 1084-1093 (2002).

30 Gross, J., O. Spuhl, F. Tumakaka and G. Sadowski, "Modeling copolymer systems using the perturbed-chain SAFT equation of state," Industrial & Engineering Chemistry Research, 42, 1266-1274 (2003).

31 Kleiner, M., F. Tumakaka, G. Sadowski, H. Latz and M. Buback, "Phase equilibria in polydisperse and associating copolymer solutions: Poly (ethene-co-(meth)acrylic acid)-monomer mixtures," Fluid Phase Equilibria, 241, 113-123 (2006).

32 McCabe, C., A. Galindo, A. Gil-Villegas and G. Jackson, "Predicting the high-pressure phase equilibria of binary mixtures of n-alkanes using the SAFT-VR approach," International Journal of Thermophysics, 19, 1511-1522 (1998).

33 McCabe, C., A. Gil-Villegas and G. Jackson, "Predicting the high-pressure phase equilibria of methane plus n-hexane using the SAFT-VR approach," Journal Of Physical Chemistry B, 102, 4183-4188 (1998).

34 McCabe, C. and G. Jackson, "SAFT-VR modelling of the phase equilibrium of long-chain n- alkanes," Physical Chemistry Chemical Physics, 1, 2057-2064 (1999).

35 McCabe, C. and S. Kiselev, "Application of Crossover Theory to the SAFT-VR Equation of State: SAFT-VRX for Pure Fluids," Industrial & Engineering Chemistry Research, in press (2004).

36 McCabe, C. and S.B. Kiselev, "A crossover SAFT-VR equation of state for pure fluids: preliminary results for light hydrocarbons," Fluid Phase Equilibria, 219, 3-9 (2004).

37 Galindo, A., L.J. Florusse and C.J. Peters, "Prediction of phase equilibria for binary systems of hydrogen chloride with ethane, propane and n-dodecane," Fluid Phase Equilibria, 160, 123-131 (1999).

38 Filipe, E.J.M., E. de Azevedo, L.F.G. Martins, V.A.M. Soares, J.C.G. Calado, C. McCabe and G. Jackson, "Thermodynamics of liquid mixtures of xenon with alkanes: (xenon plus ethane) and (xenon plus propane)," Journal Of Physical Chemistry B, 104, 1315-1321 (2000).

39 Filipe, E.J.M., L.F.G. Martins, J.C.G. Calado, C. McCabe and G. Jackson, "Thermodynamics of liquid mixtures of xenon with Alkanes: (xenon plus n-butane) and (xenon plus isobutane)," Journal Of Physical Chemistry B, 104, 1322-1325 (2000).

40 McCabe, C., L.M.B. Dias, G. Jackson and E.J.M. Filipe, "On the liquid mixtures of xenon, alkanes and perfluorinated compounds," Physical Chemistry Chemical Physics, 3, 2852-2855 (2001).

41 Sun, L.X., H.G. Zhao, S.B. Kiselev and C. McCabe, "Application of SAFT-VRX to binary phase behaviour: alkanes," Fluid Phase Equilibria, 228, 275-282 (2005).

42 Sun, L.X., H.G. Zhao, S.B. Kiselev and C. McCabe, "Predicting mixture phase equilibria and critical behavior using the SAFT-VRX approach," Journal of Physical Chemistry B, 109, 9047-9058 (2005).

43 McCabe, C., A. Galindo, A. Gil-Villegas and G. Jackson, "Predicting the high-pressure phase equilibria of binary mixtures of perfluoro-n-alkanes plus n-alkanes using the SAFT- VR approach," Journal of Physical Chemistry B, 102, 8060-8069 (1998).

44 Bonifacio, R.P., E.J.M. Filipe, C. McCabe, M.F.C. Gomes and A.A.H. Padua, "Predicting the solubility of xenon in n-hexane and n- perfluorohexane: a simulation and theoretical study," Molecular Physics, 100, 2547-2553 (2002).

45 Galindo, A., S.J. Burton, G. Jackson, D.P. Visco and D.A. Kofke, "Improved models for the phase behaviour of hydrogen fluoride: chain and ring aggregates in the SAFT approach and the AEOS model," Molecular Physics, 100, 2241-2259 (2002).

46 Dias, L.M.B., R.P. Bonifacio, E.J.M. Filipe, J.C.G. Calado, C. McCabe and G. Jackson, "Liquid-vapour equilibrium of {xBF3 + (1 - x)n-butane} at 195.49 K," Fluid Phase Equilibria, 205, 163-170 (2003).

47 Dias, L.M.B., E.J.M. Filipe, C. McCabe, T. Cordeiro and J.C.G. Calado, "Liquid Mixtures of Xenon with Fluorinated Species: Xenon + Sulfur Hexafluoride," Journal of Physical Chemistry B, in press (2007).

48 Galindo, A., A. Gil-Villegas, P.J. Whitehead, G. Jackson and A.N. Burgess, "Prediction of phase equilibria for refrigerant mixtures of difluoromethane (HFC-32), 1,1,1,2-tetrafluoroethane (HFC-134a), and pentafluoroethane (HFC-125a) using SAFT-VR," Journal of Physical Chemistry B, 102, 7632-7639 (1998).

49 McCabe, C., A. Galindo and P.T. Cummings, "Anomalies in the solubility of alkanes in near-critical water," Journal of Physical Chemistry B, 107, 12307-12314 (2003).

50 Galindo, A., A. Gil-Villegas, G. Jackson and A.N. Burgess, "SAFT-VRE: Phase behavior of electrolyte solutions with the statistical associating fluid theory for potentials of variable range," Journal of Physical Chemistry B, 103, 10272-10281 (1999).

51 Gil-Villegas, A., A. Galindo and G. Jackson, "A statistical associating fluid theory for electrolyte solutions (SAFT-VRE)," Molecular Physics, 99, 531-546 (2001).

52 Patel, B.H., P. Paricaud, A. Galindo and G.C. Maitland, "Prediction of the salting-out effect of strong electrolytes on water plus alkane solutions," Industrial & Engineering Chemistry Research, 42, 3809-3823 (2003).

53 Blas, F.J. and A. Galindo, "Study of the high pressure phase behaviour of CO2+n-alkane mixtures using the SAFT-VR approach with transferable parameters," Fluid Phase Equilibria, 194-197, 501-509 (2002).

54 Galindo, A. and F.J. Blas, "Theoretical examination of the global fluid phase behavior and critical phenomena in carbon dioxide plus n-alkane binary mixtures," Journal of Physical Chemistry B, 106, 4503-4515 (2002).

55 Colina, C.M., A. Galindo, F.J. Blas and K.E. Gubbins, "Phase behavior of carbon dioxide mixtures with n-alkanes and n-perfluoroalkanes," Fluid Phase Equilibria, 222, 77-85 (2004).

56 Colina, C.M. and K.E. Gubbins, "Vapor-liquid and vapor-liquid-liquid equilibria of carbon dioxide/n-perfluoroalkane/n-alkane ternary mixtures," Journal of Physical Chemistry B, 109, 2899-2910 (2005).

57 Zhao, H.G. and C. McCabe, "Phase behavior of dipolar fluids from a modified statistical associating fluid theory for potentials of variable range," Journal of Chemical Physics, 125 (2006).

58 Amos, M.D. and G. Jackson, "BHS Theory and Computer-Simulations of Linear Heteronuclear Triatomic Hard-Sphere Molecules," Molecular Physics, 74, 191-210 (1991).

59 Banaszak, M., C.K. Chen and M. Radosz, "Copolymer SAFT equation of state. Thermodynamic perturbation theory extended to heterobonded chains," Macromolecules, 29, 6481-6486 (1996).

60 Blas, F.J. and L.F. Vega, "Thermodynamic behaviour of homonuclear and heteronuclear Lennard-Jones chains with association sites from simulation and theory," Molecular Physics, 92, 135-150 (1997).

61 Shukla, K.P. and W.G. Chapman, "SAFT equation of state for fluid mixtures of hard chain copolymers," Molecular Physics, 91, 1075-1081 (1997).

62 Adidharma, H. and M. Radosz, "Prototype of an engineering equation of state for heterosegmented polymers," Industrial & Engineering Chemistry Research, 37, 4453-4462 (1998).

63 Adidharma, H. and M. Radosz, "Square-well SAFT equation of state for homopolymeric and heteropolymeric fluids," Fluid Phase Equilibria, 160, 165-174 (1999).

64 McCabe, C., A. Gil-Villegas, G. Jackson and F. Del Rio, "The thermodynamics of heteronuclear molecules formed from bonded square-well (BSW) segments using the SAFT-VR approach," Molecular Physics, 97, 551-558 (1999).

65 Tumakaka, F., J. Gross and G. Sadowski, "Modeling of polymer phase equilibria using Perturbed-Chain SAFT," Fluid Phase Equilibria, 194-197, 541-551 (2002).

66 Singh, D.K. and K.N. Khanna, "Equations of state for fluids containing alternating heteronuclear chain molecules," Journal of Molecular Liquids, 115, 5-15 (2004).

67 Amos, M.D. and G. Jackson, "Bonded Hard-Sphere (BHS) Theory for the Equation of State of Fused Hard-Sphere Polyatomic-Molecules and Their Mixtures," Journal of Chemical Physics, 96, 4604-4618 (1992).

68 Sear, R.P., M.D. Amos and G. Jackson, "Bonded Hard-Sphere Theory and Computer-Simulations of Polyatomic Hard-Sphere Models of Alkanes and Their Derivatives," Molecular Physics, 80, 777-788 (1993).

69 Dickman, R. and C.K. Hall, "Equation Of State For Chain Molecules - Continuous-Space Analog Of Flory Theory," Journal Of Chemical Physics, 85, 4108-4115 (1986).

70 Dickman, R. and C.K. Hall, "High-Density Monte-Carlo Simulations Of Chain Molecules - Bulk Equation Of State And Density Profile Near Walls," Journal Of Chemical Physics, 89, 3168-3174 (1988).

71 Chiew, Y.C., "Percus-Yevick Integral-Equation Theory For Athermal Hard-Sphere Chains.1. Equations Of State," Molecular Physics, 70, 129-143 (1990).

72 Pan, C. and M. Radosz, "Copolymer SAFT modeling of phase behavior in hydrocarbon-chain solutions: Alkane oligomers, polyethylene, poly(ethylene-co-olefin-1), polystyrene, and poly(ethylene-co-styrene)," Industrial & Engineering Chemistry Research, 37, 3169-3179 (1998).

73 Banaszak, M. and M. Radosz, "Molecular dynamics study on homonuclear and heteronuclear chains of Lennard-Jones segments," Fluid Phase Equilibria, 193, 179-189 (2002).

74 Chan, A.K.C., H. Adidharma and M. Radosz, "Fluid-liquid transitions of poly(ethylene-co-octene-1) in supercritical ethylene solutions," Industrial & Engineering Chemistry Research, 39, 4370-4375 (2000).

75 Tang, Y.P., "A SAFT model for associating Lennard-Jones chain mixtures," Molecular Physics, 100, 1033-1047 (2002).

76 Equations of State for Fluids and Fluid Mixtures. Part II. (Elsevier, Amsterdam, 2000).

77 Allen, M.P. and D.J. Tildesley, Computer Simulation of Liquids. (Oxford University Press, Oxford, 1987).

78 Panagiotopoulos, A.Z., "Direct Determination Of Phase Coexistence Properties Of Fluids By Monte-Carlo Simulation In A New Ensemble," Molecular Physics, 61, 813-826 (1987).

79 Frenkel, D. and B. Smit, Understanding molecular simulation: from algorithms to applications, Second ed. (Academic Press, San Diego, 2002).

80 Widom, B., "Some topics in the theory of fluids," Journal of Chemical Physics, 39, 2802-2812 (1963).

81 Mooij, G. and D. Frenkel, "A systematic optimization scheme for configurational bias Monte Carlo," Molecular Simulation, 17, 41-55 (1996).

82 Frenkel, D., G.C.A.M. Mooij and B. Smit, "Novel Scheme to Study Structual and Thermal Properties of Continuously Deformable Molecules," Journal of Physics-Condensed Matter, 3, 3053-3076 (1991).

83 Siepmann, J.I. and D. Frenkel, "Configurational Bias Monte-Carlo - a New Sampling Scheme for Flexible Chains," Molecular Physics, 75, 59-70 (1992).

84 Frenkel, D. and B. Smit, Understanding molecular simulation: from algorithms to applications. (Academic Press, San Diego, 1996).

85 Frenkel, D., G. Mooij and B. Smit, "Novel Scheme To Study Structural And Thermal-Properties Of Continuously Deformable Molecules," Journal of Physics-Condensed Matter, 4, 3053-3076 (1992).

86 Berendsen, H.J.C., J.P.M. Postma, W.F. Vangunsteren, A. Dinola and J.R. Haak, "Molecular-Dynamics with Coupling to an External Bath," Journal of Chemical Physics, 81, 3684-3690 (1984).

87 Nose, S., "A Molecular-Dynamics Method For Simulations In The Canonical Ensemble," Molecular Physics, 52, 255-268 (1984).

88 Nosé, S., "A unified formulation of the constant temperature molecular dynamics methods," Journal of Chemical Physics, 81, 511-519 (1984).

89 Rowlinson, J.S. and F.L. Swinton, Liquids and Liquid Mixtures, 3rd ed. (Butterworth Scientific, London, 1982).

90 Leonard, P.J., Henderso.D and J.A. Barker, "Perturbation Theory and Liquid Mixtures," Transactions of the Faraday Society, 66, 2439-& (1970).

91 Boublik, T., "Hard-Sphere Equation of State," Journal of Chemical Physics, 53, 471-472 (1970).

92 Mansoori, G.A., N.F. Carnahan, K.E. Starling and T.W. Leland, "Equilibrium Thermodynamic Properties of Mixture of Hard Spheres," Journal of Chemical Physics, 54, 1523-1525 (1971).

93 Carnahan, N.F. and K.E. Starling, "Equation of State for Nonattracting Rigid Spheres," Journal of Chemical Physics, 51, 635-636 (1969).

94 Patel, B.H., H. Docherty, S. Varga, A. Galindo and G.C. Maitland, "Generalized equation of state for square-well potentials of variable range," Molecular Physics, 103, 129-139 (2005).

95 Gulati, H.S. and C.K. Hall, "Generalized Flory equations of state for copolymers modeled as square-well chain fluids," Journal of Chemical Physics, 108, 7478-7492 (1998).

96 Frenkel, D. and B. Smit, Understanding molecular simulation: from algorithms to applications, 2nd ed. (Academic Press, San Diego, 2001).

97 McCabe, C. and S.B. Kiselev, "Application of crossover theory to the SAFT-VR equation of state: SAFT-VRX for pure fluids," Industrial & Engineering Chemistry Research, 43, 2839-2851 (2004).

98 Laine, R.M., "Nanobuilding blocks based on the $[OSiO_{1.5}](x)$ (x=6, 8, 10) octasilsesquioxanes," Journal of Materials Chemistry, 15, 3725-3744 (2005).

99 Fu, B.X., L. Yang, R.H. Somani, S.X. Zong, B.S. Hsiao, S. Phillips, R. Blanski and P. Ruth, "Crystallization studies of isotactic polypropylene containing nanostructured polyhedral oligomeric silsesquioxane molecules under quiescent and shear conditions," Journal of Polymer Science Part B-Polymer Physics, 39, 2727-2739 (2001).

100 Kopesky, E.T., T.S. Haddad, R.E. Cohen and G.H. McKinley, "Thermomechanical properties of poly(methyl methacrylate)s containing tethered and untethered polyhedral oligomeric silsesquioxanes," Macromolecules, 37, 8992-9004 (2004).

101 Bolln, C., A. Tsuchida, H. Frey and R. Mulhaupt, "Thermal properties of the homologous series of 8-fold alkyl-substituted octasilsesquioxanes," Chemistry of Materials, 9, 1475-1479 (1997).

102 Balaban, A.T., D.J. Klein, N.H. March, M.P. Tosi and M. Ausloos, "Phase-transition regularities in critical constants, fusion temperatures and enthalpies of chemically similar chainlike structures," Chemphyschem, 6, 1741-1745 (2005).

103 Knischka, R., F. Dietsche, R. Hanselmann, H. Frey, R. Mulhaupt and P.J. Lutz, "Silsesquioxane-based amphiphiles," Langmuir, 15, 4752-4756 (1999).

104 Bharadwaj, R.K., R.J. Berry and B.L. Farmer, "Molecular dynamics simulation study of norbornene-POSS polymers," Polymer, 41, 7209-7221 (2000).

105 Lamm, M.H., T. Chen and S.C. Glotzer, "Simulated assembly of nanostructured organic/inorganic networks," Nano Letters, 3, 989-994 (2003).

106 Sheng, Y.J., W.J. Lin and W.C. Chen, "Network structures of polyhedral oligomeric silsesquioxane based nanocomposites: A Monte Carlo study," Journal of Chemical Physics, 121, 9693-9701 (2004).

107 Capaldi, F.M., G.C. Rutledge and M.C. Boyce, "Structure and dynamics of blends of polyhedral oligomeric silsesquioxanes and polyethylene by atomistic simulation," Macromolecules, 38, 6700-6709 (2005).

108 Striolo, A., C. McCabe and P.T. Cummings, "Thermodynamic and transport properties of polyhedral oligomeric sislesquioxanes in poly(dimethylsiloxane)," Journal of Physical Chemistry B, 109, 14300-14307 (2005).

109 Striolo, A., C. McCabe and P.T. Cummings, "Effective interactions between polyhedral oligomeric sislesquioxanes dissolved in normal hexadecane from molecular simulation," Macromolecules, 38, 8950-8959 (2005).

110 Patel, R.R., R. Mohanraj and C.U. Pittman, "Properties of polystyrene and polymethyl methacrylate copolymers of polyhedral oligomeric silsesquioxanes: A molecular dynamics study," Journal of Polymer Science Part B-Polymer Physics, 44, 234-248 (2006).

111 Striolo, A., C. McCabe and P.T. Cummings, "Organic-inorganic telechelic molecules: Solution properties from simulations," Journal of Chemical Physics, 125, Art. No. 104904 (2006).

112 Zhang, X., E.R. Chan and S.C. Glotzer, "Self-assembled morphologies of monotethered polyhedral oligomeric silsesquioxane nanocubes from computer simulation," Journal of Chemical Physics, 123, Art. No. 184718 (2005).

113 Striolo, A., E.R. Chan, C. McCabe, S.C. Glotzer and P.T. Cummings, "Aggregation of POSS monomers in Liquid Hexane: A Molecular-simulation Study," Journal of Physical Chemistry B, submitted (2006).

114 Chapman, W.G., G. Jackson and K.E. Gubbins, "Phase-Equilibria of Associating Fluids Chain Molecules With Multiple Bonding Sites," Molecular Physics, 65, 1057-1079 (1988).

115 Chapman, W.G., K.E. Gubbins, G. Jackson and M. Radosz, "New Reference Equation of State For Associating Liquids," Industrial & Engineering Chemistry Research, 29, 1709-1721 (1990).

116 Muller, E.A. and K.E. Gubbins, in *Equations of State for Fluids and Fluid Mixtures*, edited by J. V. Sengers, R. F. Kayser, C. J. Peters and H. J. J. White (Elsevier, Amsterdam, 2000), Vol. I, pp. 435.

117 Economou, I.G., "Statistical associating fluid theory: A successful model for the calculation of thermodynamic and phase equilibrium properties of complex fluid mixtures," Industrial & Engineering Chemistry Research, 41, 953-962 (2002).

118 Smith, W. and T.R. Forester, "DL_POLY_2.0: A general-purpose parallel molecular dynamics simulation package," Journal Of Molecular Graphics, 14, 136-141 (1996).

119 Ionescu, T.C., F. Qi, C. McCabe, A. Striolo, J. Kieffer and P.T. Cummings, "Evaluation of force fields for molecular simulation of polyhedral oligomeric silsesquioxanes," Journal of Physical Chemistry B, 110, 2502-2510 (2006).

120 Voronkov, M.G. and V.I. Lavrentyev, "Polyhedral Oligosilsesquioxanes and Their Homo Derivatives," Topics in Current Chemistry, 102, 199-236 (1982).

121 Siepmann, J.I., S. Karaborni and B. Smit, "Simulating the Critical-Behavior of Complex Fluids," Nature, 365, 330-332 (1993).

122 Sun, H., "Ab-Initio Calculations and Force-Field Development for Computer-Simulation of Polysilanes," Macromolecules, 28, 701-712 (1995).

123 Sun, H. and D. Rigby, "Polysiloxanes: Ab initio force field and structural, conformational and thermophysical properties," Spectrochimica Acta Part a-Molecular and Biomolecular Spectroscopy, 53, 1301-1323 (1997).

124 Martin, M.G. and J.I. Siepmann, "Transferable potentials for phase equilibria. 1. United-atom description of n-alkanes," Journal of Physical Chemistry B, 102, 2569-2577 (1998).

125 Li, H.C., C.Y. Lee, C. McCabe, A. Striolo and M. Neurock, "Ab initio analysis of the structural properties of alkyl-substituted polyhedral oligomeric silsesquioxanes," Journal of Physical Chemistry A, 111, 3577-3584 (2007).

126 Frischknecht, A.L. and J.G. Curro, "Improved united atom force field for poly(dimethylsiloxane)," Macromolecules, 36, 2122-2129 (2003).

127 McCabe, C. and G. Jackson, "SAFT-VR modelling of the phase equilibrium of long-chain n-alkanes," Physical Chemistry Chemical Physics, 1, 2057-2064 (1999).

128 GilVillegas, A., A. Galindo, P.J. Whitehead, S.J. Mills, G. Jackson and A.N. Burgess, "Statistical associating fluid theory for chain molecules with attractive potentials of variable range," Journal of Chemical Physics, 106, 4168-4186 (1997).

129 Boese, R., H.C. Weiss and D. Blaser, "The melting point alternation in the short-chain n-alkanes: Single-crystal X-ray analyses of propane at 30 K and of n-butane to n-nonane at 90 K," Angewandte Chemie-International Edition, 38, 988-992 (1999).

130 Chen, S.J., M. Banaszak and M. Radosz, "Phase-Behavior Of Poly(Ethylene-1-Butene) In Subcritical And Supercritical Propane - Ethyl Branches Reduce Segment Energy And Enhance Miscibility," Macromolecules, 28, 1812-1817 (1995).

131 Shen, Z., M.A. McHugh, J. Xu, J. Belardi, S. Kilic, A. Mesiano, S. Bane, C. Karnikas, E. Beckman and R. Enick, "CO2-solubility of oligomers and polymers that contain the carbonyl group," Polymer, 44, 1491-1498 (2003).

132 Chen, C.K., M. Banaszak and M. Radosz, "Statistical associating fluid theory equation of state with Lennard-Jones reference applied to pure and binary n-alkane systems," Journal of Physical Chemistry B, 102, 2427-2431 (1998).

133 Blas, F.J. and L.F. Vega, "Prediction of Binary and Ternary Diagrams Using the Statistical Associating Fluid Theory (SAFT) Equation of State," Industrial & Engineering Chemistry Research, 37, 660-674 (1998).

134 Sadowski, G., "A square-well based equation of state taking into account the connectivity in chain molecules," Fluid Phase Equilibria, 149, 75-89 (1998).

135 Jiang, J. and J.M. Prausnitz, "Equation of state for thermodynamic properties of chain fluids ner-to and far-from the vapor-liquid critical region," Journal of Chemical Physics, 111, 5964 (1999).

136 Paredes, M.L.L., R. Nobrega and F.W. Tavares, "An equation of state for polymers and normal fluids using the square-well potential of variable well width," Industrial & Engineering Chemistry Research, 40, 1748-1754 (2001).

137 Pamies, J.C. and L.F. Vega, "Critical properties of homopolymer fluids studied by a Lennard- Jones statistical associating fluid theory," Molecular Physics, 100, 2519-2529 (2002).

138 Chen, S.J., I.G. Economou and M. Radosz, "Density-Tuned Polyolefin Phase-Equilibria.2. Multicomponent Solutions of Alternating Poly(Ethylene Propylene) in Subcritical and Supercritical Olefins - Experiment and Saft Model," Macromolecules, 25, 4987-4995 (1992).

139 Hasch, B.M. and M.A. McHugh, "Calculating Poly(Ethylene-Co-Acrylic Acid)-Solvent Phase- Behavior with the Saft Equation of State," Journal of Polymer Science Part B-Polymer Physics, 33, 715-723 (1995).

140 Lee, S.H., B.M. Hasch and M.A. McHugh, "Calculating copolymer solution behavior with Statistical Associating Fluid Theory," Fluid Phase Equilibria, 117, 61-68 (1996).

141 Koak, N., R.M. Visser and T.W. de Loos, "High-pressure phase behavior of the systems polyethylene plus ethylene and polybutene+1-butene," Fluid Phase Equilibria, 160, 835-846 (1999).

142 Takishima, S., M.L. O'Neill and K.P. Johnston, "Solubility of Block Copolymer Surfactants in Compressed CO2 Using a Lattice Fluid Hydrogen-Bonding Model," Industrial & Engineering Chemistry Research, 36, 2821-2833 (1997).

143 Gregg, C.J., F.P. Stein and M. Radosz, "Phase-Behavior of Telechelic Polyisobutylene (Pib) in Subcritical and Supercritical Fluids.1. Inter-Association and Intra-Association Effects for Blank, Monohydroxy, and Dihydroxy Pib(1k) in Ethane, Propane, Dimethyl Ether, Carbon-Dioxide, and Chlorodifluoromethane," Macromolecules, 27, 4972-4980 (1994).

144 Sadowski, G., L.V. Mokrushina and W. Arlt, "Finite and infinite dilution activity coefficients in polycarbonate systems," Fluid Phase Equilibria, 139, 391-403 (1997).

145 Lora, M., F. Rindfleisch and M.A. McHugh, "Influence of the alkyl tail on the solubility of poly(alkyl acrylates) in ethylene and CO2 at high pressures: Experiments and modeling," Journal of Applied Polymer Science, 73, 1979-1991 (1999).

146 Tamouza, S., J.P. Passarello, P. Tobaly and J.C. de Hemptinne, "Group contribution method with SAFT EOS applied to vapor liquid equilibria of various hydrocarbon series," Fluid Phase Equilibria, 222, 67-76 (2004).

147 Tamouza, S., J.P. Passarello, P. Tobaly and J.C. de Hemptinne, "Application to binary mixtures of a group contribution SAFT EOS (GC-SAFT)," Fluid Phase Equilibria, 228, 409-419 (2005).

148 Thi, T.X.N., S. Tamouza, P. Tobaly, J.P. Passarello and J.C. de Hemptinne, "Application of group contribution SAFT equation of state (GC-SAFT) to model phase behaviour of light and heavy esters," Fluid Phase Equilibria, 238, 254-261 (2005).

149 Le Thi, C., S. Tamouza, J.P. Passarello, P. Tobaly and J.C. de Hemptinne, "Modeling phase equilibrium of H-2+n-alkane and CO2+n-alkane binary mixtures using a group contribution statistical association fluid theory equation of state (GC-SAFT-EOS) with a k(ij) group contribution method," Industrial & Engineering Chemistry Research, 45, 6803-6810 (2006).

150 Jackson, G. and K.E. Gubbins, "Mixtures Of Associating Spherical And Chain Molecules," Pure and Applied Chemistry, 61, 1021-1026 (1989).

151 Archer, A.L., M.D. Amos, G. Jackson and I.A. McLure, "The theoretical prediction of the critical points of alkanes, perfluoroalkanes, and their mixtures using bonded hard-sphere (BHS) theory," International Journal of Thermophysics, 17, 201-211 (1996).

152 DIPPR 801 Tables, Thermophysical Properties Database, (2005).

153 Smith, B.D. and R. Srivastava, Thermodynamic Data for Pure Compounds. Part A. hydrocarbons and ketones. (Elsevier, London, 1986).

154 Wisniak, J., E. Magen, M. Shachar, I. Zeroni, R. Reich and H. Segura, "Phase equilibria in the systems hexane plus heptane and methyl 1,1-dimethylethyl ether plus hexane plus heptane," Journal of Chemical and Engineering Data, 42, 458-462 (1997).

155 Jan, D.S., H.Y. Shiau and F.N. Tsai, "Vapor-Liquid-Equilibria Of N-Hexane Plus Cyclohexane Plus N-Heptane And The 3 Constituent Binary-Systems At 101.0-Kpa," Journal of Chemical and Engineering Data, 39, 438-440 (1994).

156 McGlashan, M.L. and A.G. Williamson, "Thermodynamics of Mixtures of n-Hexane + n-Hexadecane. Part 2. Vapor Pressures and Activity," Trans. Faraday Soc., 588-600 (1961).

157 Joyce, P.C. and M.C. Thies, "Vapor-liquid equilibria for the hexane plus hexadecane and hexane plus 1-hexadecanol systems at elevated temperatures and pressures," Journal of Chemical and Engineering Data, 43, 819-822 (1998).

158 Fuchs, R., L. Krenzer and J. Gaube, "Excess Properties of Binary Mixtures Composed of a Polar Component and an Alkane," Ber. Bunsen-Ges. Phy. Chem., 642-649 (1984).

159 Geiseler, G. and H. Kohler, "Thermodynamic Behavior Of Methyl Ethyl Ketoxime/N-Heptane Diethyl Ketone/N-Heptane And Methyl Ketoxime/Diethyl Ketone Mixed Systems," Berichte Der Bunsen-Gesellschaft Fur Physikalische Chemie, 72, 697-706 (1968).

160 Barraza, R., S. Diaz, J. Edwards and P. Tapia, "Thermodynamics Of The Systems Normal-Hexane-3-Pentanone, Normal-Hexane-Acetone And Normal-Heptane-3-Pentanone Mixtures," Zeitschrift Fur Physikalische Chemie-Wiesbaden, 117, 43-54 (1979).

161 Maripuri, V.C. and G.A. Ratcliff, "Isothermal Vapor-Liquid Equilibria In Binary-Mixtures Of Ketones And Alkanes," Journal Of Applied Chemistry And Biotechnology, 22, 899-& (1972).

162 Renon, H. and Prausnit.Jm, "Liquid-Liquid And Vapor-Liquid Equilibria For Binary And Ternary Systems With Dibutyl Ketone Dimethyl Sulfoxide N-Hexane And 1-Hexene," Industrial & Engineering Chemistry Process Design and Development, 7, 220-225 (1968).

163 Ortega, J., C. Gonzalez and S. Galvan, "Vapor-liquid equilibria for binary systems composed of a propyl ester (ethanoate, propanoate, butanoate) plus an n-alkane (C-7, C-9)," Journal of Chemical and Engineering Data, 46, 904-912 (2001).

164 Ortega, J., F. Espiau, J. Tojo, J. Canosa and A. Rodriguez, "Isobaric vapor-liquid equilibria and excess properties for the binary systems of methyl esters plus heptane," Journal of Chemical and Engineering Data, 48, 1183-1190 (2003).

165 Rose, A. and W.R. Supina, "Vapor pressure and vapor-liquid equilibrium data for methyl esters of the common saturated normal fatty acids," J. Chem. Eng. Data, 6, 173-179 (1961).

166 Zervopoulou, E., V.G. Mavrantzas and D.N. Theodorou, "A new Monte Carlo simulation approach for the prediction of sorption equilibria of oligomers in polymer melts: Solubility of long alkanes in linear polyethylene," Journal of Chemical Physics, 115, 2860-2875 (2001).

167 Bokis, C.P., H. Orbey and C.C. Chen, "Properly model polymer processes," Chemical Engineering Progress, 95, 39-52 (1999).

168 von Solms, N., I.A. Kouskoumvekaki, T. Lindvig, M.L. Michelsen and G.M. Kontogeorgis, "A novel approach to liquid-liquid equilibrium in polymer systems with application to simplified PC-SAFT," Fluid Phase Equilibria, 222, 87-93 (2004).

169 Tumakaka, F., J. Gross and G. Sadowski, "Modeling of polymer phase equilibria using Perturbed-Chain SAFT," Fluid Phase Equilibria, 194, 541-551 (2002).

170 Shukla, K.P. and W.G. Chapman, "TPT2 and SAFTD equations of state for mixtures of hard chain copolymers," Molecular Physics, 98, 2045-2052 (2000).

171 Chen, C.K., M.A. Duran and M. Radosz, "Phase-Equilibria in Polymer-Solutions - Block-Algebra, Simultaneous Flash Algorithm Coupled with Saft Equation of State, Applied to Single-Stage Supercritical Antisolvent Fractionation of Polyethylene," Industrial & Engineering Chemistry Research, 32, 3123-3127 (1993).

172 Xiong, Y. and E. Kiran, "Comparison of Sanchez-Lacombe and Saft Model in Predicting Solubility of Polyethylene in High-Pressure Fluids," Journal of Applied Polymer Science, 55, 1805-1818 (1995).

173 Orbey, H., C.P. Bokis and C.C. Chen, "Equation of state modeling of phase equilibrium in the low-density polyethylene process: The Sanchez-Lacombe, statistical associating fluid theory, and polymer-Soave-Redlich-Kwong equations of state," Industrial & Engineering Chemistry Research, 37, 4481-4491 (1998).

174 Spyriouni, T. and I.G. Economou, "Evaluation of SAFT and PC-SAFT models for the description of homo- and co-polymer solution phase equilibria," Polymer, 46, 10772-10781 (2005).

175 Haslam, A.J., N. von Solms, C.S. Adjiman, A. Galindo, G. Jackson, P. Paricaud, M.L. Michelsen and G.M. Kontogeorgis, "Predicting enhanced absorption of light gases in polyethylene using simplified PC-SAFT and SAFT-VR," Fluid Phase Equilibria, 243, 74-91 (2006).

176 Dominik, A. and W.G. Chapman, "Thermodynamic model for branched polyolefins using the PC-SAFT equation of state," Macromolecules, 38, 10836-10843 (2005).

177 Chan, K.C., H. Adidharma and M. Radosz, "Fluid-liquid and fluid-solid transitions of poly(ethylene-co- octene-1) in sub- and supercritical propane solutions," Industrial & Engineering Chemistry Research, 39, 3069-3075 (2000).

178 Kouskoumvekaki, I.A., N. Von Solms, T. Lindvig, M.L. Michelsen and G.M. Kontogeorgis, "Novel method for estimating pure-component parameters for polymers: Application to the PC-SAFT equation of state," Industrial & Engineering Chemistry Research, 43, 2830-2838 (2004).

179 Surana, R.K., R.P. Danner, A.B. de Haan and N. Beckers, "New technique to measure high-pressure and high-temperature polymer-solvent vapor-liquid equilibrium," Fluid Phase Equilibria, 139, 361-370 (1997).

180 Wohlfarth, C., Vapour-liquid equilibrium data of binary polymer solutions. (Elsevier, Amsterdam, 1994).

181 Hao, W., H.S. Elbro and P. Alessi, in *Chemistry Data Series* (DECHEMA, Frankfurt, 1992), Vol. XIV, pp. Part 1.

182 Paricaud, P., presented at the Conference Name, Conference Location, 2003 of Conference (unpublished).

183 Xiong, Y. and E. Kiran, "High-Pressure Phase-Behavior In Polyethylene N-Butane Binary And Polyethylene N-Butane Co2 Ternary-Systems," Journal of Applied Polymer Science, 53, 1179-1190 (1994).

184 Kiran, E., Y. Xiong and W.H. Zhuang, "Modeling Polyethylene Solutions In Near And Supercritical Fluids Using The Sanchez-Lacombe Model," Journal of Supercritical Fluids, 6, 193-203 (1993).

185 Saeki, S., S. Konno, N. Kuwahara, M. Nakata and M. Kaneko, "Upper And Lower Critical Solution Temperatures In Polystyrene Solutions.3. Temperature-Dependence Of Chi-1 Parameter," Macromolecules, 7, 521-526 (1974).

186 Sarbu, T., T. Styranec and E.J. Beckman, "Non-fluorous polymers with very high solubility in supercritical CO2 down to low pressures," Nature, 405, 165-168 (2000).

187 Raveendran, P. and S.L. Wallen, "Sugar acetates as novel, renewable CO2-philes," Journal of the American Chemical Society, 124, 7274-7275 (2002).